

DYNAMIC ACOUSTIC PARAMETERS OF POROUS MEDIA

a theoretical, numerical, and experimental investigation

DYNAMIC ACOUSTIC PARAMETERS OF POROUS MEDIA

a theoretical, numerical, and experimental investigation

PROEFSCHRIFT

ter verkrijging van de graad van doctor
aan de Technische Universiteit Delft,
op gezag van de Rector Magnificus
Prof.dr. ir J.T. Fokkema,
voorzitter van het College voor Promoties,
in het openbaar te verdedigen
op dinsdag 7 Mei 2002 te 16.00 uur

door

ANDREA CORTIS

Dottore in Ingegneria Civile Idraulica, Università degli Studi di Cagliari
geboren te Iglesias (Italië)

Dit proefschrift is goedgekeurd door de promotor:
Prof.dr.ir. J.T. Fokkema

Samenstelling promotiecommissie:

Rector Magnificus,	voorzitter
Prof.dr.ir. J.T. Fokkema,	Technische Universiteit Delft, promotor
Dr.ir. D.M.J. Smeulders,	Technische Universiteit Delft, toegevoegd promotor
Prof.ir. C.P.J.W. van Kruijsdijk,	Technische Universiteit Delft
Prof.dr.ir. C.P.A. Wapenaar,	Technische Universiteit Delft
Prof.dr.ir. M.E.H. van Dongen,	Technische Universiteit Eindhoven
Prof.dr. S. Pride,	Université de Rennes
Dr. D. Lafarge,	Université du Maine

Printed by:
Drukkerij Technische Universiteit Delft
ISBN xx-xxxxxxx-x

¹³And I applied my mind to seek and to search out by wisdom all that is done under heaven; it is an unhappy business that God has given to the sons of men to be busy with.

¹⁴I have seen everything that is done under the sun; and behold, all is vanity and a striving after wind.

¹⁵What is crooked cannot be made straight, and what is lacking cannot be numbered.

Ecclesiastes 1, 13-15

CONTENTS

	Abstract	1
I	Upscaling techniques for porous media	5
§ 1	Introduction	5
§ 2	The Representative Elementary Volume	8
§ 3	Geometric characterization	10
§ 4	Microscopic vs Macroscopic theories	12
§ 5	The volume averaging with closure method	14
§ 6	Double scale asymptotic expansion	17
§ 7	Biot’s approach to porous media	20
§ 8	Conclusions	22
II	From micro to macro	25
§ 9	Microscopic equations	25
§ 10	Homogenization of the system	28
§ 11	Macroscopic laws	32
§ 12	Analytic solution for a cylindrical tube	35
§ 13	Dynamic thermal behavior	39
§ 14	Conclusions	41
III	On the viscous length scale of wedge-shaped porous media	43
§ 15	Introduction	43
§ 16	Wedge-shaped geometries	46
§ 17	Schwartz–Christoffel Transformations	48

§ 18	Numerical results	52
§ 19	Pore variation technique	56
§ 20	Conclusions	58
IV	Influence of pore roughness on high-frequency permeability	59
§ 21	Introduction	59
§ 22	Oscillating Stokes flow	62
§ 23	High-frequency velocity pattern in smooth geometries . . .	66
§ 24	High-frequency permeability and tortuosity	70
§ 25	Corrugated pore channels	73
§ 26	Non-corrugated channels	77
§ 27	Numerical computations	79
§ 28	Conclusions	84
	APPENDICES TO CHAPTER IV	
§ 29	Energetic representation of the dynamic tortuosity	86
§ 30	Proof of the identity (40)	87
V	Numerical validation of scaling functions for viscous and thermal relaxation in gas-filled porous media	89
§ 31	Scaling functions	89
§ 32	Viscous and thermal coefficients	91
§ 33	Direct dynamic numerical computations	101
§ 34	Causality	105
§ 35	Conclusions	108
	APPENDIX TO CHAPTER V	
§ 36	Causal models for viscous and thermal dynamic dissipation	108
VI	Viscous dynamic permeability: theory and experiments	113
§ 37	In-series tube geometry	113
§ 38	The porous medium under study	117
§ 39	Static permeability measurements	120
§ 40	Experiments on the tortuosity	120
§ 41	Dynamic measurements	122

§ 42 Conclusions	126
Bibliography	133
Samenvatting	135
Acknowledgements	137
Curriculum Vitæ	139

ABSTRACT

We investigate the different existing approaches for the upscaling problem of porous media, i.e., the problem of the translation of the microscopic equations to the macroscopic equations. The Homogenization Theory is shown to be equivalent to the Volume Averaging Method with Closure for the case of Darcy's law. For the case of wave propagation in porous media, the Biot theory is briefly discussed, and it is shown that it addresses the dynamic interaction between the solid and the pore fluid on a macroscopic level. It is similar to the so-called Theory of Porous Media (TPM), yet the latter does not consider this dynamic coupling. Though this may lead to correct results in the low-frequency domain, it will fail for high-frequency wave phenomena.

The high-frequency behavior of fluid velocity patterns for smooth and corrugated pore channels is studied in detail. The classical approach of Johnson et al. for smooth morphologies is obtained in different manners, thus clarifying differences with the Sheng & Zhou and Avellaneda & Torquato treatments. For extreme geometries having singularities like wedge-shaped intrusions, the classical approach has to be modified by a non-analytic extension proposed by Achdou & Avellaneda. The dependency of this extension on the apex angle of the wedge is derived and shown to be different from the original Achdou & Avellaneda theory. Precise numerical computations for various apex angles in two-dimension channels confirmed this relation. Moreover, it was found that the contribution of the singularities only adds an extra non-analytical term, but does not change the parameters of the classical theory by Johnson et al.

One of these parameters, the weighted pore volume-to-surface ratio Λ ,

is carefully evaluated for different apex angles and channel pore throat diameters. It appears that our computational method employing Schwartz-Christoffel transformations produces results that are fully identical to Finite Element computations performed by Firdaouss et al. The Schwartz-Christoffel transformations, however, are computationally much more efficient.

For low frequencies, it was pointed out by Pride et al. that the classical dynamic behavior for viscous damping as described by Johnson's scaling function, is not entirely adequate. This scaling describes the functional relationship of the dynamic permeability/tortuosity on frequency. In the viscous regime, however, non-leading order terms are not correctly predicted. Pride et al. therefore modified the viscous scaling function, and showed this modification to be correct for sinusoidally varying tubes. Essentially, a new pore space parameter, the Stokes tortuosity, was introduced to allow for this modification. This Stokes tortuosity is the low-frequency counterpart of the conventional tortuosity, which is evaluated in the limit of high frequencies. In this thesis, it is shown that also thermal damping can be addressed in this way, i.e., the thermal scaling function introduced by Allard et al. also has to be modified to obtain the correct behavior for low frequencies. Using a precise numerical Finite Element Scheme, the full dynamic viscous and heat problem is solved in two dimensions for regular arrangements of cylindrical and square fibres. The porosity is varied over a wide range by changing the radii of the cylinders or the side lengths of the squares. We find that indeed the modified scaling functions for both the thermal and viscous damping are now in full agreement with the numerical predictions.

In order to explore experimentally the dynamic behavior of extreme geometries, a model porous medium was constructed out of a stack of orifice plates separated by cylindrical spacers. In this way, a bimodal tube configuration was put together with extreme orifice-to-spacer diameter ratio. The dynamic permeability of this sample was experimentally determined in the Dynamic Darcy Cell, where an oscillating fluid flow in the sample is induced by means of an electro-mechanical device. To vary the viscosity of the fluid, different mixtures of water and glycerol were used. In this way, a broad

range of dimensionless frequencies could be covered. The temperature dependence of the mixture was measured separately. We find good agreement between the experimental results and the scaling function predictions. The properties of the model porous medium were determined separately, both experimentally and numerically. They serve as input parameters for the scaling function. These experimental and numerical results were found to be in excellent agreement.

CHAPTER I

UPSCALING TECHNIQUES FOR POROUS MEDIA

In this Chapter we give the basic definitions common to all porous materials, and compare several upscaling techniques widely used in current literature. In sections § 2 and § 3 we introduce the basic concepts of porous medium, separation of scales, Representative Elementary Volume (REV), and average quantities. In § 4 we show that the introduction of a so-called *closure hypothesis* is needed to describe the unknown coupling between the solid matrix and the fluid phase, and we point out that it can be of a macroscopic nature like in Biot's and Mixture theory approach, or of a microscopic nature like in the Volume Averaging, and the Formal Asymptotic Expansion. In § 5 we will study the microscopic upscaling technique known as Volume Averaging Method with Closure, and we compare it with the Double Scale Asymptotic Expansion presented in § 6. In § 7 we analyze the macroscopic upscaling technique used by Biot to derive a theory for the wave propagation in a saturated poro-elastic solid and we compare it to the Mixture Theory for Porous Media.

§ 1 Introduction

Porous materials are found in virtually every scientific field. Examples of this large variety of natural and artificial porous media are loose sand, sandstones, soils, concrete, absorbing foams, chemical reactors, bones, lungs, and kidneys. We define a porous medium as a portion of space consisting

of a persistent solid part called *solid matrix* and a pore space which can be occupied by one or more fluid phases (for instance gas, water, or oil). We say that a porous medium is fully saturated when a single or more fluid phases occupy the whole connected porous domain. In a porous medium, the microscopic fields are continuous in each individual phase, but can be discontinuous at the fluid-solid interface, where they may experience an abrupt change in their value, depending on the particular boundary conditions of the problem. This change actually happens at interfaces of vanishing thickness which can be treated as a mathematical discontinuity of the field.

The definition of scale of observation is essential to porous media theories. In fact, we can identify a porous medium only at a macroscopic observation scale, L_x , while we can distinguish the morphology only at a microscopic observation scale L_y . Therefore, a porous medium domain can be considered homogeneous at a macroscopic scale, with respect to any macroscopic geometrical or physical parameter, if this parameter has the same value at all points of the domain. In the same way must be understood the concept of isotropy: a porous medium is isotropic at a point with respect to a given macroscopic property, if that property doesn't vary with the direction starting from that point. If the condition $L_y \ll L_x$ is satisfied, we say that the two scales of observation are separated. Many porous media exhibit multiple separated length scales. This is the case, for instance, of oil reservoirs, in which it is possible to distinguish first the megascopic geological features, and then, going down in observation scale, the macroscopic faults, the fractures, the surface roughness of the fracture, the pore structure of the rock matrix, and finally microscopic clay structures inside the pores. Other porous materials do not show any separation of the scales: this is the case for fractal media (Cushman, 1992).

A complicated micro-structure such as that of a porous medium allows for different descriptions. Due to the wide range of disciplines in which porous media are involved, different conceptual models have been proved equally successful in the description of physical processes in porous media. One of these conceptual models is, for instance, the *array of channels* model depicted in figure 1.1. This model considers the porous medium as

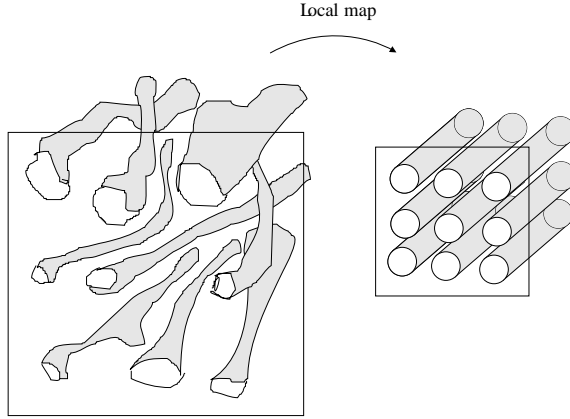


Figure 1.1: *Idealization of a porous medium as a bundle of channels mapped onto a regularly spaced array of straight tubes.*

an array of non-intersecting winding channels of varying cross section. A further idealization then maps these channels onto an array of parallel, regularly spaced, non-intersecting straight circular cylinders, a configuration for which a simple analytical solution exists. This mapping involves the use of macroscopic parameters like the porosity to describe how the channels are spaced, the tortuosity to describe how they are winded and oriented, and the permeability to account for their flow resistance. All these macroscopic parameters will be thoroughly discussed in the following chapters.

While in the *array of channels* model we stress the importance of the flow pathways, in the *network models* the emphasis is given to certain regions of the pore-space identified as pores, their size-distribution, and their mutual interconnection via some generally narrow channels called bonds (Held & Celia, 2001). A network is a graph consisting of a set of vertices (the pores) connected by bonds (the channels). The individual pores are often modelled as arranged on a regular lattice. Sahimi (1995) also discusses the possibility of introducing some surface roughness inside the pores associated with each vertex of the lattice through the use of probabilistic

distributions of protrusions inside each pore, or by the use of fractal-like surfaces.

Another possible idealization of the porous medium is the *grains model* in which the solid matrix is represented as a collection of grains with convex surface (Rubinstein & Torquato, 1989). The grains can be considered either interpenetrated or not, and are packed according some probabilistic distribution. This framework is often used to model unconsolidated materials.

§ 2 The Representative Elementary Volume

Moving up from one scale to another in a porous medium necessitates the use of some kind of average operator on the microscopic fields at the scale L_y , to obtain fields which are significant at the macroscopic scale L_x . This average operator acts on some volume of the porous medium, and assigns a macroscopic value to it. Therefore, the macroscopic fields are, unlike the microscopic fields, smeared over the space. The question arises about the correct size of the averaging volume. We define a *Representative Elementary Volume*, REV in short, as the smallest volume of integration which contains all the characteristic features of the porous medium. The size of the REV, L_x , must be intermediate between a characteristic microscopic length and a characteristic macroscopic length scale of the sample, L_R , viz., $L_y \ll L_x \ll L_R$. Sometimes these length scales depend not only on the micro-structure of the porous medium, but also on the physical process under study. It is also possible that porous media with a clear separation of the geometric scales do not have a REV for a particular physical process. This is the case for the dispersion problem in porous media, for example.

A general definition of the average operator must be made in terms of convolution products of spatial distribution functions (Cushman, 1984; Quintard & Whitaker, 1994). Let the scalar ψ be a general spatial distribution function of a physical quantity defined by

$$\psi = \begin{cases} \psi^f & \text{in the fluid volume } V_f, \\ \psi^s & \text{in the solid volume } V_s. \end{cases} \quad (2.1)$$

An example of such a distribution function is the *fluid phase indicator function* \mathcal{I}_f defined as

$$\mathcal{I}_f = \begin{cases} 1 & \text{in } V_f, \\ 0 & \text{in } V_s. \end{cases} \quad (2.2)$$

Definition (2.1) can be naturally extended to more general tensorial quantities.

The gradient of ψ is given by

$$\nabla\psi = \nabla\psi + \mathbf{n}_{fs}(\psi^f - \psi^s)\delta_{fs}, \quad (2.3)$$

in which the symbol ∇ represents the derivative in the sense of the distributions theory, ∇ is the classical spatial derivative which operates on physical quantities belonging at least to C^1 , the class of differentiable functions, \mathbf{n}_{fs} is the normal vector at A_{fs} , the fluid-solid interface, pointing from the fluid to the solid. The Dirac distribution δ_{fs} is defined as

$$\int_{\mathbb{R}^3} \psi \delta_{fs} dV = \int_{A_{fs}} \psi dA. \quad (2.4)$$

An important theorem is associated with the convolution product of the derivative of a distribution:

$$m * \nabla\psi = \nabla(m * \psi) + m * (\mathbf{n}_{fs}(\psi^f - \psi^s)\delta_{fs}), \quad (2.5)$$

where $*$ is the convolution operator defined by

$$m * \psi \Big|_{\mathbf{x}} = \int_{\mathbf{r} \in \mathbb{R}^3} m(\mathbf{x} - \mathbf{r}) \psi(\mathbf{r}) dV. \quad (2.6)$$

Here, \mathbf{x} is the vector pointing to the coordinates of the centroid of the REV, \mathbf{r} is the integration variable, and we made use of the fact that $\nabla(m * \psi) = m * \nabla\psi$ (Schwartz, 1966). The function $m(\mathbf{r})$ is a test-function such that for $m \in C^\infty$, the class of infinitely differentiable functions, m has a compact support over \mathbb{R}^3 , and $\int_{\mathbf{r} \in \mathbb{R}^3} m(\mathbf{x} - \mathbf{r}) \mathcal{I}_f dV = 1$. Equation (2.5) states that the convolution (generalized average) of the gradient of the distribution of

a physical quantity ψ , equals the gradient (in the classical sense) of the convolution of ψ , plus the convolution of a distribution defined over A_{fs} , the fluid-solid surface. This theorem is the key tool in the volume averaging method (Hassanizadeh & Gray, 1979; Whitaker, 1999). If we choose for m the test function \overline{m}

$$\overline{m} = \begin{cases} \frac{1}{V_f} & |\mathbf{x} - \mathbf{r}| \leq L_x, \\ 0 & |\mathbf{x} - \mathbf{r}| > L_x, \end{cases} \quad (2.7)$$

where V_f is the fluid volume of the REV, the classical definition of the average operator $\langle \rangle$ can be written as (see (2.6))

$$\langle \psi \rangle = \overline{m} * \psi = \frac{1}{V_f} \int_{V_f} \psi dV. \quad (2.8)$$

Substitution of the test function \overline{m} , into equation (2.5) yields

$$\langle \nabla \psi \rangle = \nabla \langle \psi \rangle + \llbracket \psi \rrbracket, \quad (2.9)$$

where we define the surface average operator $\llbracket \rrbracket$

$$\llbracket \psi \rrbracket = \overline{m} * ((\psi^f - \psi^s) \mathbf{n}_{fs} \delta_{fs}) = \frac{1}{V_f} \int_{A_{fs}} (\psi^f - \psi^s) \mathbf{n}_{fs} dA. \quad (2.10)$$

§ 3 Geometric characterization

Porous media can be distinguished into deterministic and stochastic. These attributes refer of course to the micro-geometry of the porous medium.

The idealization underlying the use of stochastic methods is that the irregular geometry is a statistical realization drawn at random from an ensemble of possible geometries, and assumes that the characteristic features of the micro-geometry can be described by some probability distribution. The pore geometry is thus described by random sets in terms of a small number of geometric parameters. On the other hand, a deterministic porous medium can be thought as a spatially periodic repetition of

some given micro-geometry. This occurs for instance in tailored materials, which are sought to satisfy some design specifications not fulfilled by natural materials.

A general characterization of porous media should be well defined in terms of geometric quantities, and should involve only parameters that are directly computable or measurable. It also should require a number of parameters which is commensurate to the process model under study, i.e., the set of parameters must be not too large (to make it economically feasible), nor too small in order to catch all the relevant features of the physical process. Among the most important geometric parameters of pore geometry we can certainly mention the porosity ϕ , which is the ratio of the pore-volume to the total volume of the REV

$$\phi = \frac{V_f}{(V_f + V_s)}. \quad (3.1)$$

We can also define a surface porosity ϕ^a which is the ratio of the fluid area on the boundary of the REV divided by A_t , the total area of the boundary itself

$$\phi^a = \frac{A_{ff}}{A_t}. \quad (3.2)$$

For homogeneous media, the Delesse principle states that the volume porosity, ϕ , can be estimated from the surface porosity, ϕ^a , obtained by image analysis techniques (Ruzyla, 1986). Another very important geometric quantity which characterizes porous media is the tortuosity α_∞ , which gives an idea of the tortuous path that a fluid particle must follow in the filtration movement. A review of the different definitions of the tortuosity proposed in the literature can be found in Diedericks & Du Plessis (1995). In the present work we will make use of the definition of the tortuosity given in Johnson *et al.* (1987). In (§ 11) we relate Johnson's definition of the tortuosity to the so-called added mass effect in the irrotational behavior of an oscillating viscous flow at high frequencies. The tortuosity can experimentally be determined since it relates to the formation factor defined as $\alpha_\infty/\phi = r_s/r_f$, where r_s is the intrinsic resistivity $[\Omega m]$ of a fluid-filled porous insulator, and r_f is the intrinsic fluid resistivity (Brown, 1980).

Furthermore, the tortuosity so defined is also numerically computable by means of the relation $\alpha_\infty = \langle |\mathbf{E}|^2 \rangle / \langle \mathbf{E} \rangle^2$, where \mathbf{E} is defined as the gradient of some potential electric field.

Another macroscopic quantity is the Darcy's permeability k_0 , which describes the flow resistance of the porous medium. The square root of the permeability, $\sqrt{k_0}$, is a length scale characteristic of the microgeometry. Other fundamental characteristic lengths, essential for the description the viscous and thermal dynamic dissipation, are the characteristic thermal length $\Lambda' = 2V_f/A_{fs}$, also known as *hydraulic radius*, and the characteristic viscous length $\Lambda = 2\langle |\mathbf{E}|^2 \rangle / \langle |\mathbf{E}|^2 \rangle$, an electrically weighted pore volume (V_f)-to-pore surface (A_{fs}) ratio (see Chapter III).

Of course it is possible to seek for relationships among the geometric quantities. Examples are the Kozeny-Carman empirical law for the permeability k_0 (see Kostek *et al.* (1992))

$$k_0 = C\Lambda'^2 \frac{\phi^3}{(1-\phi)^2}, \quad (3.3)$$

where C is some constant, and Λ' is the characteristic thermal length. Another example is Archie's law

$$\alpha_\infty = \phi^{1-c} \quad (3.4)$$

which relates the tortuosity to the so-called cementation factor c (Lynch, 1962). In the present work we will analyze in detail the Johnson *et al.* (1987) conjecture which states that the following combination of geometric parameters

$$\frac{8k_0\alpha_\infty}{\phi\Lambda^2} \approx 1 \quad (3.5)$$

for all porous materials.

§ 4 Microscopic vs Macroscopic theories

The correct description of flow and transport in multi-phase systems is a problem of increasing importance and interest in engineering. Therefore

many different theories have been proposed to describe in terms of macroscopic measurable variables the processes taking place at the microscopic level. The starting point for all these porous media theories is the definition of conservation equations for mass, momentum, and energy. This treatment is not different from the classical approach of continuum mechanics. However, unlike classical continuum mechanics, the porous media continuum mechanics introduces an extra unknown, which is due to the coupling between the solid matrix and the fluid phase. Each of these theories needs therefore the introduction of a so-called *closure hypothesis* to account for the interaction between fluid and solid. A *closure hypothesis* is an assumption about the structure of the unknown microscopic fields. For instance, it can be a relationship between the microscopic velocity field and a combination of different velocity scales like in the homogenization approach.

Two possible approaches are generally acknowledged to derive macroscopic equations for porous media: the macroscopic and the microscopic approach.

In the macroscopic approach, the phases are viewed as overlapping continua, which simultaneously exist everywhere and occupy the whole space. Among the macroscopic approaches we can count the Biot approach based on Lagrangian continuum mechanics, and the mixture theory for porous media (see § 7).

In the microscopic approach the system is conceived to be composed of different continua, each occupying only part of the space and separated by highly irregular interfaces. In the microscopic approach, the upscaling of the problem comes from the fact that the scale of system described is altered by averaging the equations over some representative element of volume like in the volume average technique described in § 5, or expanding the unknown functions by means of a small parameter ϵ like in the double-scale asymptotic expansion technique described in § 6. In sections § 5 and § 6, we will try to make a comparison between the two methods studying the Darcy's filtration problem for micro-incompressible fluids. A somewhat simplified form of the double-scale asymptotic expansion technique is also known as the *homogenization*, or *formal asymptotic expansion*. In this sim-

plified form, the expansion of the unknown microscopic physical quantities is assumed to have the form of a polynomial in the small parameter ϵ . Bourgeat *et al.* (1988) described the differences and the common points between the formal asymptotic expansion, and the volume averaging with closure method, taking as an example a linear diffusion problem. In § 10, we will use *formal asymptotic expansion*, to obtain the homogenized equations for wave propagation in porous media.

§ 5 The volume averaging with closure method

The first microscopic upscaling technique we are going to analyze is the so-called *volume averaging method with closure* (Whitaker, 1999).

The method of volume averaging is a technique that can be used to rigorously derive continuum equations for multi-phase systems. This means that equations which are *valid within a particular phase* can be spatially smoothed to produce equations that are *valid everywhere* (Whitaker, 1999).

Once the equations at the scale of the pore are averaged over the pore-volume of the REV, macroscopic equations of equilibrium are obtained which still contain reference to microscopic fields. Therefore, at this point of the method, the introduction of some kind of closure hypothesis is needed. In order to close the system of equations, Slattery (1967) used some postulates of phenomenological nature, while Whitaker (1986) used a order of magnitude analysis argument.

The first step in the volume averaging method is to write the microscopic equations governing the fluid and the solid phase at the microscopic level. The continuity equation, and the momentum balance equation for the fluid phase are written in the form

$$0 = \nabla \cdot \mathbf{v}, \quad (5.1a)$$

$$0 = -\nabla p + g\mathbf{e} + \eta \nabla^2 \mathbf{v}, \quad (5.1b)$$

$$\mathbf{v} = 0 \quad \text{on } A_{fs}, \quad (5.1c)$$

where \mathbf{v} is the microscopic fluid velocity, p is the fluid pressure, $g\mathbf{e}$ is the gravity force, $\mathbf{e} = (0, 0, e_z)$ is the unit vector, and η is the fluid viscosity. The average of the microscopic equations (5.1) is subsequently taken

$$0 = \langle \nabla \cdot \mathbf{v} \rangle, \quad (5.2a)$$

$$0 = -\langle \nabla p \rangle + \langle g\mathbf{e} \rangle + \langle \eta \nabla^2 \mathbf{v} \rangle. \quad (5.2b)$$

Introducing in (5.2) the decomposition of the pressure and velocity

$$p = \langle p \rangle + \overset{\circ}{p}, \quad (5.3a)$$

$$\mathbf{v} = \langle \mathbf{v} \rangle + \overset{\circ}{\mathbf{v}}, \quad (5.3b)$$

where $\overset{\circ}{p}$ and $\overset{\circ}{\mathbf{v}}$ represent the deviations from the average pressure and velocity respectively, and after some algebra and repeated applications of (2.9), equation (5.2) becomes

$$0 = \nabla \cdot \langle \mathbf{v} \rangle, \quad (5.4a)$$

$$0 = -\nabla \langle p \rangle + g\mathbf{e} + \eta \nabla^2 \langle \mathbf{v} \rangle + \llbracket (-\mathbf{I}\overset{\circ}{p} + \eta \nabla \overset{\circ}{\mathbf{v}}) \cdot \rrbracket, \quad (5.4b)$$

$$\overset{\circ}{\mathbf{v}} = -\langle \mathbf{v} \rangle \quad \text{on } A_{fs} \quad (5.4c)$$

$$\overset{\circ}{p}, \overset{\circ}{\mathbf{v}} \quad \text{periodic on } A_{ff}. \quad (5.4d)$$

Subtracting (5.4) from (5.1), the spatial deviation momentum equation takes the form

$$\nabla \cdot \overset{\circ}{\mathbf{v}} = 0, \quad (5.5a)$$

$$0 = -\nabla \overset{\circ}{p} + \eta \nabla^2 \overset{\circ}{\mathbf{v}} - \llbracket (-\mathbf{I}\overset{\circ}{p} + \eta \nabla \overset{\circ}{\mathbf{v}}) \cdot \rrbracket, \quad (5.5b)$$

$$\overset{\circ}{\mathbf{v}} = -\langle \mathbf{v} \rangle \quad \text{on } A_{fs}. \quad (5.5c)$$

The solution is then sought in the form

$$\overset{\circ}{\mathbf{v}} = -\mathbf{B} \cdot \langle \mathbf{v} \rangle + \Upsilon_{\mathbf{B}}, \quad (5.6a)$$

$$\frac{1}{\eta} \overset{\circ}{p} = -\mathbf{b} \cdot \langle \mathbf{v} \rangle + \Upsilon_{\mathbf{b}}, \quad (5.6b)$$

where $\Upsilon_{\mathbf{B}}$, and $\Upsilon_{\mathbf{b}}$ are arbitrary functions, which means that the second order tensor \mathbf{B} and the vector \mathbf{b} can be specified in any way one wishes, for instance in the form

$$0 = \nabla \cdot \mathbf{B}, \quad (5.7a)$$

$$-\nabla \mathbf{b} + \nabla^2 \mathbf{B} = \llbracket (-\mathbf{I} \mathbf{b} + \nabla \mathbf{B}) \cdot \rrbracket \quad (5.7b)$$

$$\mathbf{B} = -\mathbf{I} \quad \text{on } A_{fs}, \quad (5.7c)$$

$$\mathbf{B} \quad \text{periodic on } A_{ff}, \quad (5.7d)$$

$$\langle \mathbf{B} \rangle = 0. \quad (5.7e)$$

This particular choice of \mathbf{B} , and \mathbf{b} (Whitaker, 1986) allows one to prove that the microscopic fields $\Upsilon_{\mathbf{B}}$, and $\Upsilon_{\mathbf{b}}$ are equal to zero. Substituting (5.6) into (5.4b), and neglecting $\nabla^2 \langle \mathbf{v} \rangle$, the so-called Brinkman term, we obtain

$$0 = -\nabla \langle p \rangle + g\mathbf{e} - \eta \llbracket (-\mathbf{I} \mathbf{b} + \nabla \mathbf{B}) \cdot \rrbracket \langle \mathbf{v} \rangle, \quad (5.8)$$

which we recognize as the classical Darcy's law

$$\langle \mathbf{v} \rangle = -\frac{k}{\eta \phi} \cdot (\nabla \langle p \rangle - g\mathbf{e}), \quad (5.9)$$

whose permeability tensor can be written in the form

$$k = -\phi \llbracket (\mathbf{I} \mathbf{b} - \nabla \mathbf{B}) \cdot \rrbracket^{-1}. \quad (5.10)$$

However, if we choose to seek our solution in the form (Sanchez-Palencia, 1980)

$$\eta \mathbf{v} = -\mathbf{D} \cdot \langle (\nabla \langle p \rangle - g\mathbf{e}) \rangle + \Upsilon_{\mathbf{D}}, \quad (5.11a)$$

$$\overset{\circ}{p} = -\mathbf{d} \cdot \langle \mathbf{v} \rangle + \Upsilon_{\mathbf{d}}, \quad (5.11b)$$

and a closure problem for \mathbf{D} , and \mathbf{d} in the form (Barrère *et al.*, 1992)

$$0 = \nabla \cdot \mathbf{D}, \quad (5.12a)$$

$$\mathbf{I} = \nabla \mathbf{d} - \nabla^2 \mathbf{D}, \quad (5.12b)$$

$$\mathbf{D} = 0 \quad \text{on } A_{fs}, \quad (5.12c)$$

$$\mathbf{D} \quad \text{periodic on } A_{ff}, \quad (5.12d)$$

it is also possible to prove that Υ_D , and Υ_d are equal to zero, and that the permeability tensor takes the form

$$k = \phi \langle D \rangle. \quad (5.13)$$

It is possible to derive a relationship between the the closure fields of the two approaches (5.6), and (5.11). We notice that, because of the periodicity of the B and b fields on A_{ff} , the fluid boundary of the REV, the following identity holds

$$\llbracket (-lb + \nabla B) \cdot \rrbracket + \frac{1}{V_f} \int_{A_{ff}} (-lb + \nabla B) \cdot \mathbf{n}_{ff} dA = \langle (-\nabla b + \nabla^2 B) \rangle. \quad (5.14)$$

We also notice that since the permeability tensor k is constant, $\nabla^2(l : k) = 0$. Recalling the definition for k in (5.10), substituting (5.14) in (5.7), and comparing the outcome with (5.12) yields the sought relationship between the B and b fields, and the D and d fields

$$D = (B + l) : k, \quad (5.15a)$$

$$d = b \cdot k. \quad (5.15b)$$

However, though the approaches are completely equivalent, it is clear that the closure problem (5.12) is much simpler to solve than (5.7).

The considerations developed in this section show that the upscaling approach to porous media is non-unique, and that one has to choose the closure hypothesis of the averaged equations in such a way to obtain an appealing form for the final closure problem to solve.

§ 6 Double scale asymptotic expansion

The second homogenization technique we consider is the *double-scale asymptotic expansion*. This technique is based on the mathematical proof of some rather involved convergence theorems. In this section, we only try to give the sketch of the general line of thinking behind the method taking as an example the Darcy's filtration problem. The first rigorous proof of the

convergence of the method for this case was given by Tartar (1980). In the forthcoming, we will follow to the work of Allaire (1996, pp. 45–69). This technique applies essentially to periodic structures with separation of the scales, i.e., porous media in which the microscopic scale y is much smaller than the macroscopic scale x . A parameter ϵ is defined such that $\epsilon = L_y/L_x$, where L_y and L_x are two characteristic lengths of the microscopic and macroscopic scales, respectively. The periodic cell must be a smooth, bounded, connected set in \mathbb{R}^n , and so must be the subdomain which represents the fluid part of it.

The n -dimensional domain V_t is covered by a regular mesh of size ϵ : each cell $V_{t_i}^\epsilon$ is of the type $[0; \epsilon]^n$, and is divided into a fluid part $V_{f_i}^\epsilon$ and a solid part $V_{s_i}^\epsilon$

$$V_f^\epsilon = \bigcup_{i=1}^{N(\epsilon)} V_{f_i}^\epsilon, \quad V_s^\epsilon = \bigcup_{i=1}^{N(\epsilon)} V_{s_i}^\epsilon, \quad (6.1)$$

where the number of cells is $N(\epsilon) = V_t \epsilon^{-n}$.

We now consider the fluid pressure p , and velocity \mathbf{v} to be functions of the ϵ parameter. In this way we can define two sequences of functions \mathbf{v}_ϵ , and p_ϵ , whose elements satisfy the microscopic Stokes equations

$$\nabla p_\epsilon - \epsilon^2 \eta \nabla^2 \mathbf{v}_\epsilon = g \mathbf{e}, \quad (6.2a)$$

$$\nabla \cdot \mathbf{v}_\epsilon = 0, \quad (6.2b)$$

$$\mathbf{v} = 0 \quad \text{on } A_{fs}. \quad (6.2c)$$

The next step is to obtain a priori estimates of the solution \mathbf{v}_ϵ , and p_ϵ which are independent of ϵ . However, in order to do so, the sequences \mathbf{v}_ϵ , and p_ϵ must be defined in a fixed functional space independent of ϵ . This implies the extension of \mathbf{v}_ϵ and p_ϵ to the entire domain V_t . The velocity is naturally extended in the whole domain as follows

$$\check{\mathbf{v}}_\epsilon = \begin{cases} \mathbf{v}_\epsilon & \text{in } V_f^\epsilon \\ 0 & \text{in } V_s^\epsilon \end{cases} \quad (6.3)$$

while the fluid pressure needs to be smeared out also in the solid phase

$$\check{p}_\epsilon = \begin{cases} p_\epsilon & \text{in } V_f^\epsilon \\ \frac{1}{V_{f_i}^\epsilon} \int_{V_{f_i}^\epsilon} p_\epsilon & \text{in } V_{s_i}^\epsilon, \end{cases} \quad (6.4)$$

These extensions $(\check{\mathbf{v}}_\epsilon, \check{p}_\epsilon)$ satisfy the a priori estimates

$$\|\check{\mathbf{v}}_\epsilon\| + \epsilon \|\nabla \check{\mathbf{v}}_\epsilon\| \leq C, \quad (6.5a)$$

$$\|\check{p}_\epsilon\| \leq C, \quad (6.5b)$$

where the constant C does not depend on ϵ , and $\|\cdot\|$ is the norm in the space of the square-integrable functions.

It is possible to prove the following theorem (Allaire, 1996, p. 47)

Theorem. *The extension $(\check{\mathbf{v}}_\epsilon, \check{p}_\epsilon)$ of the solution $(\mathbf{v}_\epsilon, p_\epsilon)$ of (6.2) is such that $\check{\mathbf{v}}_\epsilon$ converges weakly in $L^2(V_t)^N$, the space of square integrable functions, to $\langle \mathbf{v} \rangle(x)$, \check{p}_ϵ converges strongly in $L^2(V_t)^N / \mathbb{R}$ to $p(x)$, where $(\langle \mathbf{v} \rangle(x), p(x))$ is the unique solution of the homogenized problem, a Darcy law*

$$\langle \mathbf{v} \rangle = -\frac{k}{\eta\phi} \cdot (\nabla p(x) - g\mathbf{e}), \quad (6.6a)$$

$$\nabla \cdot \langle \mathbf{v} \rangle = 0, \quad (6.6b)$$

$$\langle \mathbf{v} \rangle \cdot \mathbf{n} = 0 \quad \text{on } A_{ff}, \quad (6.6c)$$

where k is a symmetric, positive definite tensor defined by

$$k = \phi \langle \mathbf{D} \rangle, \quad (6.7)$$

and \mathbf{D} denotes the unique solution of the the local Stokes problem

$$0 = \nabla \cdot \mathbf{D}, \quad (6.8a)$$

$$\mathbf{l} = \nabla \mathbf{d} - \nabla^2 \mathbf{D}, \quad (6.8b)$$

$$\mathbf{D} = 0 \quad \text{on } A_{fs}, \quad (6.8c)$$

$$\mathbf{D} \quad \text{periodic on } A_{ff}. \quad (6.8d)$$

We notice that the incompressibility of the fluid at the microscopic scale is directly translated to the incompressibility at the macroscopic scale. Obviously, starting from compressible fluids at the micro-scale, incompressibility at the macro-scale disappears.

A simplified form of the double-scale asymptotic expansion method is often found in literature under the name of *formal asymptotic expansion method*, or simply *homogenization*. Instead of constructing the a-priori estimates (6.5), and subsequently prove the convergence, it introduces the following *ansatz* on the development of the microscopic fields

$$\psi(x, y) = \psi_0(x, y) + \epsilon \psi_1(x, y) + \epsilon^2 \psi_2(x, y) + \cdots. \quad (6.9)$$

To conclude, we notice that the macroscopic equation (6.6a), is the same as the one obtained by means the volume average method with closure in section § 5 (see (5.9)), and that we obtained the same closure problem (compare (5.12) and (6.8)). The double-scale asymptotic expansion method and the volume average method with closure are therefore equivalent for this problem.

§ 7 Biot's approach to porous media

Biot (1956*a,b*) developed a theory for the wave propagation in a poro-elastic solid containing a compressible viscous fluid, based on a Lagrangian mechanics approach. The essence of Biot's closure hypothesis consists in admitting the existence of definite positive energy density function, \mathcal{K} , and the existence of a macroscopic dissipation function, \mathcal{D} . In this sense this approach can be considered as a macroscopic upscaling approach. With an $\exp(i\omega t)$ dependence for the physical variables, the expression for the kinetic energy per unit volume, \mathcal{K} , was postulated to be in the form

$$\mathcal{K} = \frac{1}{2}(i\omega)^2 \left((1 - \phi)\rho^s \hat{\mathbf{u}}^s \cdot \hat{\mathbf{u}}^s + 2\rho_{12} \hat{\mathbf{u}}^s \cdot \hat{\mathbf{u}}^f + \phi\rho^f \hat{\mathbf{u}}^f \cdot \hat{\mathbf{u}}^f \right), \quad (7.1)$$

where $\hat{\mathbf{u}}^f$ and $\hat{\mathbf{u}}^s$ are the fluid and solid displacement vectors respectively, and ω is the frequency of the oscillation, and $\rho^{12} = -(\alpha_\infty - 1)\phi\rho^f$. The

expression for the dissipation per unit volume, \mathcal{D} , was postulated in the form

$$\mathcal{D} = \frac{1}{2} \frac{\eta \phi^2}{k_0} (i\omega) F(\omega) |\hat{\mathbf{u}}^s - \hat{\mathbf{u}}^f|^2, \quad (7.2)$$

where the complex-valued function $F(\omega)$ depends on the micro-geometry of the porous medium, and accounts for the exchange of momentum between the two phases due to the viscosity η embedding, thus, the viscous losses.

This discussion on the interaction is completely denied by another macroscopic upscaling method based on the extension of mixture theories for gases which often has been proposed in literature. This theory is referred to by de Boer (2000) as the *Theory of Porous Media* (TPM). In this theory, the macro-mechanical quantities are not related to the micro-geometry of the porous medium. Like in the Biot's Lagrangian approach described in § 7 these methods,

“... directly proceed from a macroscopic point of view, that is, in assuming a statistical distribution of the single constituents through the control space (superimposed continua), all mechanical and thermodynamic quantities are described via average functions of the micro-scale” (Ehlers & Kubik, 1994).

The key concept in this approach is the *volume fraction*, by means of which all geometric and physical quantities, such as motion, deformation, and stress, are defined in the total control space, and can be interpreted as the statistical average values of the real quantities. The closure of the system of field equations is avoided by the introduction of some ad-hoc macroscopic constitutive equations which are determined by test observations.

The missing interaction between the fluid and solid phase in the mixture theory approach is clearly exposed in the conclusion drawn by Ehlers and Kubik and stated as

Biot's classical dynamic equations of 1956 could be shown to be close to the correct result and to equal to the correct result, if either dynamic coupling included into ρ^{12} vanishes or if the solid and fluid acceleration coincide ... (Ehlers & Kubik, 1994)

This means that in the TPM approach, the tortuosity α_∞ is implicitly assumed equal to 1.

§ 8 Conclusions

In the present introductory Chapter, we gave the basic definitions common to all porous theories, and compared several upscaling techniques widely used in current literature.

In sections § 2 and § 3 we gave the definitions of porous medium, separation of scales, Representative Elementary Volume (REV), and average quantities which form the basic set of concepts of the following sections, and Chapters. In § 4 we observe that, unlike classical continuum mechanics, the porous media continuum mechanics introduces an extra unknown which is due to the coupling between the solid matrix and the fluid phase. Every theory of porous media needs therefore the introduction of some kind of *closure hypothesis*, which can be of a macroscopic nature (Biot's approach, Mixture theory approach), or of a microscopic nature (Volume Averaging, Double Scale Asymptotic Expansion). We conclude that several possible theories of porous media are possible depending on the problem at hand.

In § 5 we treated the microscopic upscaling technique known as Volume Averaging Method with Closure. From the analysis of the method, we conclude that the choice of the closure hypothesis is in general not unique, even for the same upscaling technique. For instance, Whitaker (1986) defined the closure hypothesis on the microscopic variables in the form (5.6) and derived the closure problem (5.7) with an expression for the permeability tensor (5.10). Later on, Barrère *et al.* (1992) used the same upscaling technique described in Whitaker (1986), but defined the closure hypothesis on the microscopic variables in the form (5.11), and obtained the closure problem (5.12) and the permeability tensor in the form (5.13). The equivalence of the two closure hypothesis is illustrated in (5.15). Notice, however, that the closure problem (5.7) is an integro-differential problem, which is much more difficult to solve than (5.12) which is equivalent to a classical Stokes problem. This point leaves open the question on the existence of a closure hypothesis which could lead to an even simpler closure problem than (5.7).

In § 6 we sketched another microscopic upscaling technique, the Double Scale Asymptotic Expansion. We proved that the resulting closure problems leads to the same closure problem for the microscopic variables as can be seen from the comparison of (5.12), and (6.8). The interpretation of the microscopic variables is however quite different from the Volume Averaging Method with Closure. Contrary to the assumption in § 5 where the fluid pressure is discontinuous at the fluid-solid interface, in § 6 the fluid pressure is smeared also in the solid phase space (see (6.4)), making its physical interpretation quite hard.

In § 7 we analyze the macroscopic upscaling technique used by Biot to derive a theory for the propagation of stress waves in a saturated poroelastic solid. We stress there the meaning of the coupling between fluid and solid phases, which is obtained by means of a macroscopic coefficient like the tortuosity.

CHAPTER II

FROM MICRO TO MACRO

In this chapter we present the derivation of the macroscopic equations relevant for visco-thermal dissipation in a rigid solid matrix, from the equations governing the fluid-phase at the microscopic level. We will base our exposition on the papers of Zhou & Sheng (1989), Smeulders *et al.* (1992), and Lafarge *et al.* (1997), who followed the seminal works of Lévy (1979) and Auriault *et al.* (1985). In § 10 we justify, from the homogenization point of view, the uncoupling of the full visco-thermal problem, into two independent problems, and we derive the macroscopic laws which will be discussed from a more phenomenological point of view in § 11. In § 12 we also give a numerical illustration of the limits of validity of the uncoupling hypothesis for a tube flow subjected to an external harmonic source, and we give an order of magnitude for the separation of scales threshold. In § 13 we present an original derivation of the high-frequency limit for the dynamic thermal response.

§ 9 Microscopic equations

Consider an air-filled porous medium under the excitation of an external harmonic source with frequency ω . We assume that all the quantities of interest can be written in the form $f(\mathbf{r}, t) = \hat{f}(\mathbf{r}, \omega) \exp(i\omega t)$, where $i = \sqrt{-1}$, is the imaginary unit.

The linearized fluid motion is completely characterized, at the microscopic level, by the fluid velocity $\hat{\mathbf{v}}(\mathbf{r}, \omega)$, the excess fluid pressure $\hat{p}(\mathbf{r}, \omega)$, with respect to the fluid pressure at rest \bar{p} , the excess fluid density $\hat{\rho}(\mathbf{r}, \omega)$, with respect to the fluid density at rest $\bar{\rho}$, and the excess fluid temperature $\hat{T}(\mathbf{r}, \omega)$, with respect to the fluid temperature at rest \bar{T} , where all the excess quantities are supposed to be small with respect to the reference quantity at rest. The solid is assumed to be at rest.

The linearized equations governing the fluid phase at the microscopic scale are the conservation of mass

$$i\omega\hat{\rho} + \bar{\rho}\nabla \cdot \hat{\mathbf{v}} = 0; \quad (9.1)$$

the conservation of momentum

$$i\omega\bar{\rho}\hat{\mathbf{v}} = \nabla \cdot \hat{\boldsymbol{\sigma}}, \quad (9.2)$$

where $\hat{\boldsymbol{\sigma}}$ is the fluid stress tensor, and the linearized conservation of energy for the fluid phase

$$i\omega\bar{\rho}\hat{s} = \frac{1}{\bar{T}}\nabla \cdot (\lambda\nabla\hat{T}) + \frac{1}{\bar{T}}(\hat{\boldsymbol{\sigma}} + \hat{p}\mathbf{I}) : \nabla\hat{\mathbf{v}}, \quad (9.3)$$

where s is the fluid entropy, and λ is the thermal conductivity. We notice that the term $(\hat{\boldsymbol{\sigma}} + \hat{p}\mathbf{I}) : \nabla\hat{\mathbf{v}}$, represents the decrease per unit time of the in the kinetic energy owing to dissipation, and can be therefore neglected in our analysis. The quantities $\hat{\rho}$, and \hat{s} are expressed as functions of \hat{p} , and \hat{T} , by means of the relations

$$d\rho = \left. \frac{\partial\rho}{\partial p} \right|_T dp + \left. \frac{\partial\rho}{\partial T} \right|_p dT, \quad (9.4)$$

$$ds = \left. \frac{\partial s}{\partial p} \right|_T dp + \left. \frac{\partial s}{\partial T} \right|_p dT. \quad (9.5)$$

With the definitions of the specific heat at constant pressure c_p ,

$$c_p = \bar{T} \left. \frac{\partial s}{\partial T} \right|_p, \quad (9.6)$$

the coefficient of thermal expansion at constant pressure κ

$$\kappa = -\frac{1}{\bar{\rho}} \frac{\partial \rho}{\partial T} \Big|_p, \quad (9.7)$$

and the isothermal compressibility coefficient K

$$\frac{1}{K} = \frac{1}{\bar{\rho}} \frac{\partial \rho}{\partial p} \Big|_T, \quad (9.8)$$

and noticing that from one of the Maxwell relations

$$\frac{\partial s}{\partial p} \Big|_T = \frac{1}{(\bar{\rho})^2} \frac{\partial \rho}{\partial T} \Big|_p, \quad (9.9)$$

it is possible to write the excess density and entropy as a function of the pressure and the temperature in the form

$$\hat{\rho} = \frac{\bar{\rho}}{K} \hat{p} - \bar{\rho} \kappa \hat{T}, \quad (9.10)$$

$$\hat{s} = \frac{c_p}{T} \hat{T} - \frac{\kappa}{\bar{\rho}} \hat{p}. \quad (9.11)$$

In this study we limit ourselves to consider viscous Newtonian saturating fluids whose stress tensor can be written

$$\hat{\boldsymbol{\sigma}} = -\hat{p} \mathbf{I} + \eta (\nabla \hat{\mathbf{v}} + \hat{\mathbf{v}} \nabla - \frac{2}{3} \mathbf{I} \nabla \cdot \hat{\mathbf{v}}) + \eta' \mathbf{I} \nabla \cdot \hat{\mathbf{v}}, \quad (9.12)$$

where η and η' are the dynamic and bulk fluid viscosities. The notation $\nabla \hat{\mathbf{v}} + \hat{\mathbf{v}} \nabla = \frac{\partial \hat{v}_i}{\partial x_j} + \frac{\partial \hat{v}_j}{\partial x_i}$. We consider all the coefficients in the stress tensor not depending on the frequency, nor on pressure, velocity or temperature. The value of \mathbf{v} at the fluid-solid interface A_{fs} is prescribed by the classical no-slip boundary condition,

$$\hat{\mathbf{v}} = 0. \quad (9.13)$$

The condition for the excess temperature \hat{T} at A_{fs} is

$$\hat{T} = 0, \quad (9.14)$$

which means that the solid matrix has a much larger heat capacity than the fluid phase, and therefore cannot be heated up by any change in temperature of the fluid.

§ 10 Homogenization of the system

In the present work we will restrict ourselves to the study of the fluid viscous and thermal dissipation, in fully saturated permeable porous media. Of course, many other dissipation mechanism could be, and actually are, responsible for the damping of the acoustic waves in a porous medium such as, for instance, the electro-acoustic dissipation in brine-saturated porous media (Pride, 1994), or the squirt-flow mechanism (Parra, 1997).

In § 9 we derived the coupled set of microscopic equations

$$i\omega(\frac{\bar{\rho}}{K}\hat{p} - \bar{\rho}\kappa\hat{T}) + \bar{\rho}\nabla \cdot \hat{\mathbf{v}} = 0, \quad (10.1a)$$

$$i\omega\bar{\rho}\hat{\mathbf{v}} = \nabla \cdot (-\hat{p}\mathbf{I} + \eta(\nabla\hat{\mathbf{v}} + \hat{\mathbf{v}}\nabla - \frac{2}{3}\mathbf{I}\nabla \cdot \hat{\mathbf{v}}) + \eta'\mathbf{I}\nabla \cdot \hat{\mathbf{v}}), \quad (10.1b)$$

$$i\omega\bar{\rho}(\frac{c_p}{T}\hat{T} - \frac{\kappa}{\bar{\rho}}\hat{p}) = \frac{1}{T}\nabla \cdot (\lambda\nabla\hat{T}). \quad (10.1c)$$

The solution of this system of equations is impossible for any non-trivial geometry and its numerical solution also represents a very difficult task. However, in most of the application cases, it is possible to define a small parameter ϵ which enables significant simplifications in the computation of some average quantities of interest. When we perform a measurement in a porous medium it is clear that we have to define the scale of the observation. Thus, for a porous medium of length L_R , the macroscopic pressure gradient is defined on a length scale L_x , such that $L_y \ll L_x \ll L_R$, where L_y is a length scale characteristic of the pore size. We define therefore the small parameter $\epsilon = L_y/L_x$. In order to avoid scattering, we impose that the wavelength $\lambda = 2\pi c_a/\omega \approx L_x$, where c_a is the speed of sound in air, and the frequency ω scales like ν/L_y^2 . For sedimentary rocks saturated with water, $\epsilon \approx 10^{-3}$ (Zhou & Sheng, 1989), whereas $\epsilon \approx 10^{-4}$ for usual acoustic materials saturated with air (Lafarge *et al.*, 1997).

Following Zhou & Sheng (1989) and Lafarge *et al.* (1997), we will express pressure in units of $L_x\eta^2/\bar{\rho}L_y^3$, while the temperature \hat{T} will be expressed in $L_x\eta^3/\bar{\rho}^2\lambda L_y^3$. Let's consider the case of an ideal gas saturating the pore

space. With the above scalings, we can write the system (10.1) in the following non-dimensional form

$$i\omega \hat{\mathbf{v}} = -\epsilon^{-1} \nabla \hat{p} + \nabla^2 \hat{\mathbf{v}} + \left(\frac{1}{3} + \frac{\eta'}{\eta} \right) \nabla (\nabla \cdot \hat{\mathbf{v}}), \quad (10.2a)$$

$$i\omega \left(\hat{p} - \frac{\gamma-1}{\gamma} \text{Pr} \hat{T} \right) = -\frac{1}{\gamma} \epsilon^{-1} \nabla \cdot \hat{\mathbf{v}}, \quad (10.2b)$$

$$i\omega \text{Pr} \hat{T} = i\omega \hat{p} + \nabla^2 \hat{T}, \quad (10.2c)$$

$$\hat{\mathbf{v}} = 0 \quad \text{on } A_{fs}, \quad (10.2d)$$

$$\hat{T} = 0 \quad \text{on } A_{fs}, \quad (10.2e)$$

where $\text{Pr} = \eta c_p / \lambda$ is the Prandtl number and

$$\frac{\bar{T} \kappa^2 K}{\bar{\rho} c_p} = \frac{\gamma-1}{\gamma} \quad (10.3)$$

is a well known thermodynamic identity (Pierce, 1989, p. 30). For an ideal gas $\kappa \bar{T} = 1$. Now we are ready to apply the well known technique of homogenization to equations (10.2). This technique consists essentially of three steps (Sanchez-Palencia, 1980). First we write the unknowns of the problem as a function of the two scales x , and y ,

$$\hat{\mathbf{v}}(x, y) = \hat{\mathbf{v}}_0(x, y) + \epsilon \hat{\mathbf{v}}_1(x, y) + \epsilon^2 \hat{\mathbf{v}}_2(x, y) + \dots \quad (10.4a)$$

$$\hat{p}(x, y) = \hat{p}_0(x, y) + \epsilon \hat{p}_1(x, y) + \epsilon^2 \hat{p}_2(x, y) + \dots \quad (10.4b)$$

$$\hat{T}(x, y) = \hat{T}_0(x, y) + \epsilon \hat{T}_1(x, y) + \epsilon^2 \hat{T}_2(x, y) + \dots, \quad (10.4c)$$

where we made use of the fact that the parameter ϵ is small to write the expansions. Secondly, we write the gradient operator in the form :

$$\nabla = \epsilon \nabla_x + \nabla_y. \quad (10.5)$$

Finally we substitute (10.4), and (10.5) in (10.2), and we collect the terms with the same power of ϵ . This leads to a hierarchy of equations:

$$-\nabla_y \hat{p}_1 + \nabla_y^2 \hat{\mathbf{v}}_0 - i\omega \hat{\mathbf{v}}_0 = \nabla_x \hat{p}_0, \quad (10.6a)$$

$$\nabla_y \cdot \hat{\mathbf{v}}_0 = 0, \quad (10.6b)$$

$$-i\omega \left(\hat{p}_0 - \frac{\gamma-1}{\gamma} \text{Pr} \hat{T}_0 \right) = \frac{1}{\gamma} (\nabla_x \cdot \hat{\mathbf{v}}_0 + \nabla_y \cdot \hat{\mathbf{v}}_1), \quad (10.6c)$$

$$i\omega \text{Pr} \hat{T}_0 = i\omega \hat{p}_0 + \nabla_y^2 \hat{T}_0, \quad (10.6d)$$

$$\nabla_y \hat{p}_0 = 0. \quad (10.6e)$$

Equation (10.6b) states that we can treat the fluid as incompressible at a microscopic scale. Equation (10.6e) states that \hat{p}_0 is a macroscopic variable. We notice that the Stokes equations (10.6a-10.6b), and the heat-transfer equation (10.6d-10.6e) result now uncoupled, which means that the viscous dissipation and the thermal dissipation are two phenomena which are not mutually interfering in porous media with separation of scales. In section § 12, we will compare the classical Rayleigh solution of the coupled Navier-Stokes-Fourier problem with the uncoupled solution for the case of a straight cylinder, and we will discuss for which value of the parameter ϵ the uncoupling hypothesis is valid. Since the fields $\hat{p}_1(x, y)$, $\hat{\mathbf{v}}_0(x, y)$, and $\hat{T}_0(x, y)$, are the solutions of linear systems, they can be formally expressed by means of linear operators acting on the source terms $-\nabla_x \hat{p}_0$ and $i\omega \hat{p}_0$

$$\hat{p}_1 = -\mathbf{P}_\omega(x, y) \cdot \nabla_x \hat{p}_0, \quad (10.7a)$$

$$\hat{\mathbf{v}}_0 = -\mathbf{V}_\omega(x, y) \cdot \nabla_x \hat{p}_0, \quad (10.7b)$$

$$\hat{T}_0 = \mathbf{T}_\omega(x, y) i\omega \hat{p}_0. \quad (10.7c)$$

The linear operators $\mathbf{T}_\omega(x, y)$, $\mathbf{P}_\omega(x, y)$, $\mathbf{V}_\omega(x, y)$ are scalar, vector and second rank tensor operators respectively. Substitution of equations (10.7) into (10.6) yields the following set of partial differential equations

$$i\omega \mathbf{V}_\omega - \nabla_y^2 \mathbf{V}_\omega + \nabla_y \mathbf{P}_\omega = \mathbf{I}, \quad (10.8a)$$

$$\nabla_y \cdot \mathbf{V}_\omega = 0, \quad (10.8b)$$

$$i\omega \text{Pr} \mathbf{T}_\omega - \nabla_y^2 \mathbf{T}_\omega = I, \quad (10.9)$$

with the boundary conditions

$$\mathbf{V}_\omega = 0 \quad (y \in A_{fs}), \quad (10.10)$$

$$\mathbf{T}_\omega = 0 \quad (y \in A_{fs}). \quad (10.11)$$

General expressions like (10.8) and (10.9) are referred in literature as *closure problems*. The terms \mathbf{I} , and I in equations (10.8a), and (10.9) represent the second rank tensor and scalar unit operators respectively.

Averaging of (10.7b) over the y-scale, leads to the macroscopic equation

$$\langle \hat{\mathbf{v}}_0 \rangle = -\langle \mathbf{V}_\omega(x, y) \rangle \cdot \nabla_x \hat{p}_0, \quad (10.12)$$

which is the extension of the classical Darcy law in the frequency domain. We can therefore define a complex tensorial quantity called the dynamic permeability $k(\omega)$, which can be computed by

$$k(\omega) = \phi \langle \mathbf{V}_\omega(x, y) \rangle. \quad (10.13)$$

Note that it is written in dimensionless form here. It was shown by Burrige & Keller (1981) that in the case of a flexible skeleton, the source term $\nabla_x \hat{p}_0$ can be replaced by $\nabla_x \hat{p}_0 + (i\omega)^2 \hat{\mathbf{u}}_0$, where $\hat{\mathbf{u}}_0$ is the solid displacement vector. However, also in this case the same generic set of equations (10.8) and (10.9) needs to be solved.

Averaging of the equation (10.7c) over the y-scale, leads to the macroscopic equation

$$\langle \hat{T}_0 \rangle = \langle \mathbf{T}_\omega(x, y) \rangle (i\omega \hat{p}_0), \quad (10.14)$$

which can be thought as the thermal analogous of the classical Darcy's law. This means that we can define a thermal dynamic permeability

$$k'(\omega) = \phi \langle \mathbf{T}_\omega(x, y) \rangle, \quad (10.15)$$

analogous to the viscous dynamic permeability. Notice, however, that the thermal permeability is a scalar quantity and not a second rank tensor as the viscous permeability.

§ 11 Macroscopic laws

In § 10 we derived the two macroscopic laws which are relevant for the viscous and thermal dissipation. In this section we analyze these response functions in their dimensional form from a more phenomenological point of view.

The dynamic Darcy's law is written as:

$$\langle \hat{\mathbf{v}} \rangle = -\frac{k(\omega)}{\eta\phi} \cdot \nabla \langle \hat{p} \rangle, \quad (11.1)$$

where $\langle \hat{\mathbf{v}} \rangle$ is the macroscopic velocity, $\langle \hat{p} \rangle$ is the macroscopic pressure, ϕ the porosity, and η the fluid viscosity. At low enough frequencies, the region of the fluid which is submitted to the viscous dissipation encompasses the entire pore volume. So, from a phenomenological point of view, we can think equation (11.1), as a natural extension of the classical Darcy's law in which the permeability factor is complex-valued. The low frequency limit $k_0 = \lim_{\omega \rightarrow 0} k(\omega)$ is the classical static Darcy permeability which can be computed by

$$\frac{k_0}{L_y^2} = \phi \langle \mathbf{V}_0 \rangle, \quad (11.2)$$

where \mathbf{V}_0 is the solution of (10.8) for a frequency $\omega = 0$. At high enough frequencies, the bulk of the pores experience a potential fluid motion, while the viscous dissipation occurs only in a very tiny boundary layer near the fluid-solid surface A_{fs} . In this case the inertial forces predominate over the viscous forces and the macroscopic law which describes the fluid flow is given by

$$i\omega\bar{\rho}\alpha_\infty \cdot \langle \hat{\mathbf{v}} \rangle = -\nabla \langle \hat{p} \rangle, \quad (11.3)$$

where $\alpha_\infty > 1$ accounts for the so called *added mass* due to the resistance offered by the tortuous microscopic paths to the flow. This parameter is usually called the *tortuosity* of the porous medium. The definition of the tortuosity is given by

$$\alpha_\infty = \langle \mathbf{E} \cdot \mathbf{E} \rangle \cdot (\langle \mathbf{E} \rangle \cdot \langle \mathbf{E} \rangle)^{-1}, \quad (11.4)$$

where \mathbf{E} , is the gradient of some potential field, from which we see that the tortuosity is a purely geometric parameter. As the imaginary unit on the left hand side of (11.3) suggests, the phase shift of the microscopic velocity field with respect to the driving force is equal to $\pi/2$ over the entire pore volume. However, when the frequency is high but not infinite, a viscous boundary layer still exists. It is therefore natural to define a dynamic complex-valued tortuosity depending on the frequency. The viscous interaction between the solid and the fluid as a result of a wave propagation can be therefore rewritten in terms of the dynamic tortuosity tensor $\alpha(\omega)$ as

$$i\omega\bar{\rho}\alpha(\omega) \cdot \langle \hat{\mathbf{v}} \rangle = -\nabla \langle \hat{p} \rangle. \quad (11.5)$$

From (11.1) and (11.5), we notice that the dynamic parameters are inter-related:

$$\frac{\alpha(\omega)}{\alpha_\infty} = \frac{k_0}{k(\omega)} \frac{\omega_c}{i\omega}, \quad (11.6)$$

where

$$\omega_c = \frac{\eta\phi}{\alpha_\infty k_0 \bar{\rho}}, \quad (11.7)$$

is the viscous roll-over frequency, which is characteristic of the transition between the viscous and the inertia dominated regimes: for sake of simplicity, a scalar notation has been used.

In a perfect analogous way to the viscous case, Lafarge (1993) proposed a description for the thermal dissipation in the form of a thermal permeability $k'(\omega)$ or a thermal tortuosity $\alpha'(\omega)$:

$$\frac{\lambda\phi}{k'(\omega)} \langle \hat{T} \rangle = i\omega \langle \hat{p} \rangle, \quad (11.8)$$

$$i\omega\alpha'(\omega)\rho c_p \langle \hat{T} \rangle = i\omega \langle \hat{p} \rangle, \quad (11.9)$$

which relate the macroscopic temperature $\langle \hat{T} \rangle$ to the time derivative of the macroscopic pressure. An alternate formulation to the $k'(\omega)$ is via the dynamic compressibility $\beta(\omega)$, which accounts for the frequency-dependent thermal effects that take place at the pore scale:

$$i\omega \frac{\beta(\omega)}{\gamma\bar{p}} \langle \hat{p} \rangle = -\nabla \cdot \langle \hat{\mathbf{v}} \rangle, \quad (11.10)$$

with γ the specific heat ratio and \bar{p} the ambient pressure. The low frequency limit $k'_0 = \lim_{\omega \rightarrow 0} k'(\omega)$ is the so-called static thermal permeability which can be computed by

$$k'_0 = \phi \langle T_0 \rangle L_y^2, \quad (11.11)$$

where T_0 is the solution of (10.9) for a frequency $\omega = 0$. The dynamic thermal permeability $k'(\omega)$ is of course directly related to $\beta(\omega)$ (Lafarge *et al.*, 1997). Averaging (10.6c) we can write, in dimensionless quantities

$$-i\omega \left(\hat{p}_0 - \frac{\gamma - 1}{\gamma} \text{Pr} \langle \hat{T}_0 \rangle \right) = \frac{1}{\gamma} (\nabla_x \cdot \langle \hat{\mathbf{v}}_0 \rangle + \langle \nabla_y \cdot \hat{\mathbf{v}}_1 \rangle). \quad (11.12)$$

The term $\langle \nabla_y \cdot \hat{\mathbf{v}}_1 \rangle = 0$ (Lafarge *et al.*, 1997, eq. A14). Substituting (10.14) and (11.11) into (11.12), we obtain

$$\frac{-\nabla_x \cdot \langle \hat{\mathbf{v}}_0 \rangle}{i\omega \hat{p}_0} = \gamma - (\gamma - 1) \text{Pr} \frac{k'(\omega)}{\phi} i\omega, \quad (11.13)$$

from which the desired relation between $\beta(\omega)$ and $k'(\omega)$ follows after introduction of the dimensions

$$\beta(\omega) = \gamma - (\gamma - 1) \frac{i\omega \rho \text{Pr}}{\eta \phi} k'(\omega). \quad (11.14)$$

From (11.8) and (11.8), we notice that $\alpha'(\omega)$ and $k'(\omega)$ are related:

$$\alpha'(\omega) = \frac{k'_0}{k'(\omega)} \frac{\omega'_c}{i\omega}, \quad (11.15)$$

where we defined the characteristic thermal frequency

$$\omega'_c = \frac{\lambda \phi}{\bar{\rho} c_p k'_0}. \quad (11.16)$$

The viscous and thermal functions can be thought as transfer functions and must therefore satisfy the causality requirement, i.e., the condition that no effect can precede its cause. Johnson *et al.* (1987) proved that, based on a theorem on the unforced oscillations of the Stokes equations, the response

functions $k(\omega)$ and $\alpha(\omega)$ are analytic everywhere in the complex-frequency $\hat{\omega} = \tilde{\omega} + i\check{\omega}$ plane except for values of $\tilde{\omega}$ on the positive imaginary axis. Lafarge (1993) gave an analogous proof for the response functions $k'(\omega)$ and $\alpha'(\omega)$. This means that the macroscopic response functions are minimum phase shift.

From the two fundamental macroscopic equations (11.5) and (11.10) is now possible to derive the macroscopic wave equation for the pressure disturbance \hat{p} . For sake of simplicity, and without any loss of generality, let's consider the case of an isotropic porous medium for which we can write

$$i\omega\bar{\rho}\alpha(\omega)\langle\hat{\mathbf{v}}\rangle = -\nabla\langle\hat{p}\rangle, \quad (11.17a)$$

$$i\omega\frac{\beta(\omega)}{\gamma\bar{p}}\langle\hat{p}\rangle = -\nabla\cdot\langle\hat{\mathbf{v}}\rangle. \quad (11.17b)$$

Application of the divergence operator $\nabla\cdot$ to (11.17a), and subsequent substitution into (11.17b) yields

$$\nabla^2\langle\hat{p}\rangle - \frac{\bar{\rho}}{\gamma\bar{p}}\alpha(\omega)\beta(\omega)(i\omega)^2\langle\hat{p}\rangle = 0 \quad (11.18)$$

which is the desired wave equation for the pressure disturbance \hat{p} . The wave velocity c is thus equal to

$$c = i\frac{c_a}{\Gamma} = \frac{c_a}{\sqrt{\alpha(\omega)\beta(\omega)}}, \quad (11.19)$$

where $c_a = \sqrt{\gamma\bar{p}/\bar{\rho}}$ is the adiabatic sound speed in the gas, and Γ is the so-called propagation constant.

§ 12 Analytic solution for a cylindrical tube

In § 10 we showed that, under the assumption of the separation of scales ($\epsilon \ll 1$), it is possible to simplify considerably the problem under study decoupling the full thermo-viscous problem into two independent problems, viz., the viscous and the thermal one. However, analytic solutions for both the coupled and the uncoupled problems do exist only for the simple case

of a straight tube (and the corresponding 2D case of slit flow) for example. In this section we present these classical analytical solutions. One might ask why so much emphasis is given to such a micro-geometry which is not even close to the classical image of a porous medium. The answer lies in the fact that we can imagine our porous medium as an ensemble of pores of different sizes connected by individual channels. In general these channels are neither straight nor of constant width, and the pores can be of different sizes and shapes. Yet, the solution for a straight tube of constant width can be an example for the class of all porous media.

Let x and r be the coordinates measured along the longitudinal and radial directions of the tube of radius R . Introducing the dimensionless axial symmetric coordinates $\xi = \omega x/c_a$, and $\zeta = r/R$, and neglecting the effects due to the bulk viscosity η' , the fully coupled thermo-viscous problem (10.2) can be rewritten in the form (Tijedman, 1975)

$$i\hat{v}_\xi = -\frac{1}{\gamma} \frac{\partial \hat{p}}{\partial \xi} + \frac{1}{\text{Wo}^2} \left[\text{He}^2 \frac{\partial^2 \hat{v}_\xi}{\partial \xi^2} + \frac{\partial^2 \hat{v}_\xi}{\partial \zeta^2} + \frac{1}{\zeta} \frac{\partial \hat{v}_\xi}{\partial \zeta} + \right. \\ \left. \text{He} \frac{1}{3} \frac{\partial}{\partial \xi} \left(\text{He} \frac{\partial \hat{v}_\xi}{\partial \xi} + \frac{\partial \hat{v}_\zeta}{\partial \zeta} + \frac{\hat{v}_\zeta}{\zeta} \right) \right], \quad (12.1a)$$

$$i\hat{v}_\zeta = -\frac{1}{\gamma} \frac{1}{\text{He}} \frac{\partial \hat{p}}{\partial \zeta} + \frac{1}{\text{Wo}^2} \left[\frac{\partial^2 \hat{v}_\zeta}{\partial \zeta^2} + \frac{1}{\zeta} \frac{\partial \hat{v}_\zeta}{\partial \zeta} - \frac{\hat{v}_\zeta}{\zeta^2} + \text{He}^2 \frac{\partial^2 \hat{v}_\zeta}{\partial \xi^2} + \right. \\ \left. \frac{1}{3} \frac{\partial}{\partial \xi} \left(\text{He} \frac{\partial \hat{v}_\xi}{\partial \xi} + \frac{\partial \hat{v}_\zeta}{\partial \zeta} + \frac{\hat{v}_\zeta}{\zeta} \right) \right], \quad (12.1b)$$

$$i\hat{p} = -\frac{1}{\text{He}} \left[\text{He} \frac{\partial \hat{v}_\xi}{\partial \xi} + \frac{\partial \hat{v}_\zeta}{\partial \zeta} + \frac{\hat{v}_\zeta}{\zeta} \right], \quad (12.1c)$$

$$\hat{p} = \hat{\rho} + \hat{T}, \quad (12.1d)$$

$$i\hat{T} = \frac{1}{\text{Pr}} \frac{1}{\text{Wo}^2} \left[\frac{\partial^2 \hat{T}}{\partial \zeta^2} + \frac{1}{\zeta} \frac{\partial \hat{T}}{\partial \zeta} + \text{He}^2 \frac{\partial^2 \hat{T}}{\partial \xi^2} \right] + i \frac{\gamma - 1}{\gamma} \hat{p}, \quad (12.1e)$$

where the Helmholtz number He is equal to

$$He = \omega R/c, \quad (12.2)$$

and the Womersley number Wo is equal to

$$Wo = R\sqrt{\omega/\nu}. \quad (12.3)$$

The solution for the pressure perturbation, \hat{p} , of the fully coupled thermo-viscous problem (12.1), can be put in the form

$$\hat{p} = A(\zeta)e^{\Gamma\zeta} + B(\zeta)e^{-\Gamma\zeta} \quad (12.4)$$

where Γ is the propagation constant, and A , and B are two real valued functions of the radial coordinate ζ . The real part of Γ represents the attenuation in the longitudinal axis direction, and the imaginary part of Γ represent the phase shift over the same direction. The solution to the fully-coupled problem was given by Kirchhoff (Rayleigh, 1894, vol.2), in the form of a transcendental complex frequency equation. After some algebra the solution can be rewritten as (Tijdeman, 1975)

$$\begin{aligned} f(\Gamma) = & i\Gamma^2 \left(\Gamma^2 - i\frac{Wo^2}{He^2} \right)^{-\frac{1}{2}} \left(\frac{1}{x_1} - \frac{1}{x_2} \right) \frac{J_1(y_1)}{J_0(y_1)} \\ & + \left(\frac{\gamma}{Pr} \frac{He^2}{Wo^2} - i\frac{1}{x_1} \right) (\Gamma^2 - x_1)^{\frac{1}{2}} \frac{J_1(y_2)}{J_0(y_2)} \\ & - \left(\frac{\gamma}{Pr} \frac{He^2}{Wo^2} - i\frac{1}{x_2} \right) (\Gamma^2 - x_2)^{\frac{1}{2}} \frac{J_1(y_3)}{J_0(y_3)} = 0, \end{aligned} \quad (12.5a)$$

where

$$y_1 = He \left(\Gamma^2 - i\frac{Wo^2}{He^2} \right)^{\frac{1}{2}}, \quad y_2 = He (\Gamma^2 - x_1)^{\frac{1}{2}}, \quad y_3 = He (\Gamma^2 - x_2)^{\frac{1}{2}}, \quad (12.5b)$$

and x_1 and x_2 are the two roots of

$$1 + \left(1 + i\frac{He^2}{Wo^2} \left(\frac{4}{3} + \frac{\gamma}{Pr} \right) \right) x + i\frac{\gamma}{Pr} \frac{He^2}{Wo^2} \left(\frac{1}{\gamma} + i\frac{4}{3} \frac{He^2}{Wo^2} \right) x^2 = 0. \quad (12.5c)$$

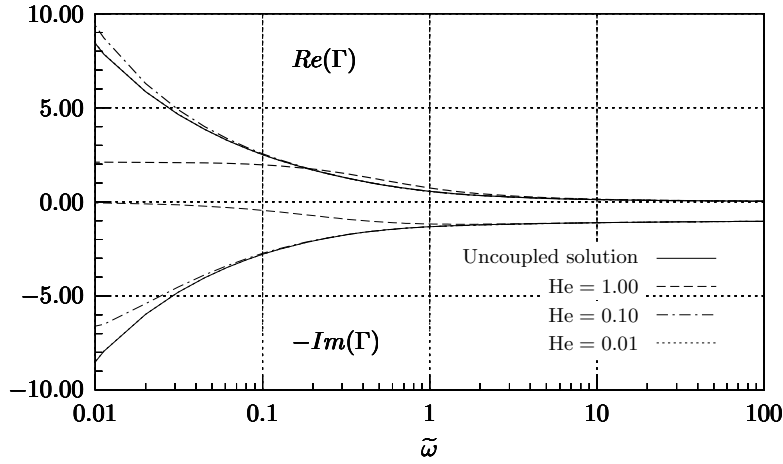


Figure 12.1: Comparison of the uncoupled solution (12.6) (solid line) with the coupled solution (12.5) for several values of the Helmholtz number He , and $Pr = 1$. The curve corresponding to the uncoupled solution $He = 0.01$ is practically indistinguishable from the fully coupled solution.

Equation (12.5) can be solved by means of a simple Newton-Raphson method.

The propagation constant Γ for the uncoupled problem is given by (Zwikker & Kosten, 1949)

$$\Gamma = \sqrt{\frac{J_0(i^{3/2} Wo)}{J_2(i^{3/2} Wo)}} \sqrt{\gamma + (\gamma - 1) \frac{J_2(i^{3/2} Wo Pr^{1/2})}{J_0(i^{3/2} Wo Pr^{1/2})}}, \quad (12.6)$$

where J_n is the Bessel function of the first kind of order n . We can now compare the solutions for Γ of (12.6) to those of (12.5) as a function of the Helmholtz number He . In figure 12.1 we plotted the propagation constant Γ vs the non-dimensional frequency $\tilde{\omega}$, both for the uncoupled (solid line) and coupled case, the latter for three different values of He . The Prandtl number was assumed $Pr = 1$. We notice that in the high frequency range,

the coupled and uncoupled solutions practically coincide, while differences can be appreciated in the low frequency range. We also notice that the curve corresponding to the uncoupled solution $\text{He} = 0.01$ is practically indistinguishable from the coupled solution, which gives us a threshold for the validity of the uncoupling hypothesis for wave propagation in porous media.

§ 13 Dynamic thermal behavior

Smeulders *et al.* (1992) derived the high frequency behavior of the dynamic viscous tortuosity based on a micro-structural approach. The first step in order to derive the high-frequency behavior for the thermal dissipation is to rewrite the expressions of the real and imaginary part of the dynamic thermal tortuosity $\alpha'(\omega)$. From (10.15), (11.11), and (11.15) we have that

$$i\tilde{\omega}\alpha'(\omega)\langle\tilde{T}_\omega\rangle = 1, \quad (13.1)$$

where $\tilde{\omega} = \omega/\omega'_e$, and the excess temperature was normalized with $\langle T_0 \rangle$. We now take the complex conjugate expression of (13.1):

$$-i\tilde{\omega}\alpha'^*(\omega)\langle\tilde{T}_\omega^*\rangle = 1, \quad (13.2)$$

and we multiply (13.1) and (13.2) by $\langle\tilde{T}_\omega^*\rangle$ and $\langle\tilde{T}_\omega\rangle$ respectively to obtain

$$i\tilde{\omega}\alpha'(\omega)|\langle\tilde{T}_\omega\rangle|^2 = \langle\tilde{T}_\omega^*\rangle, \quad (13.3)$$

$$-i\tilde{\omega}\alpha'^*(\omega)|\langle\tilde{T}_\omega\rangle|^2 = \langle\tilde{T}_\omega\rangle. \quad (13.4)$$

The temperature field T_ω satisfies:

$$i\tilde{\omega}\tilde{T}_\omega - \nabla^2\tilde{T}_\omega = 1. \quad (13.5)$$

We take the complex conjugate of (13.5)

$$-i\tilde{\omega}\tilde{T}_\omega^* - \nabla^2\tilde{T}_\omega^* = 1, \quad (13.6)$$

and we multiply (13.5) and (13.6) for \tilde{T}_ω^* and \tilde{T}_ω respectively to obtain

$$i\tilde{\omega}|\tilde{T}_\omega|^2 - \tilde{T}_\omega^* \nabla^2 \tilde{T}_\omega = \tilde{T}_\omega^*, \quad (13.7)$$

$$-i\tilde{\omega}|\tilde{T}_\omega|^2 - \tilde{T}_\omega \nabla^2 \tilde{T}_\omega^* = \tilde{T}_\omega. \quad (13.8)$$

Adding to and subtracting (13.7) and (13.8) from each other, and taking the pore-volume average we obtain:

$$\langle \tilde{T}_\omega^* + \tilde{T}_\omega \rangle = -\langle \tilde{T}_\omega^* \nabla^2 \tilde{T}_\omega + \tilde{T}_\omega \nabla^2 \tilde{T}_\omega^* \rangle, \quad (13.9)$$

$$\langle \tilde{T}_\omega^* - \tilde{T}_\omega \rangle = 2i\tilde{\omega} \langle |\tilde{T}_\omega|^2 \rangle - \langle \tilde{T}_\omega^* \nabla^2 \tilde{T}_\omega - \tilde{T}_\omega \nabla^2 \tilde{T}_\omega^* \rangle. \quad (13.10)$$

Now we also add to and subtract (13.3) and (13.4) from each other

$$i\tilde{\omega} (\alpha'(\omega) + \alpha'^*(\omega)) |\langle \tilde{T}_\omega \rangle|^2 = \langle \tilde{T}_\omega^* \rangle - \langle \tilde{T}_\omega \rangle, \quad (13.11)$$

$$i\tilde{\omega} (\alpha'(\omega) - \alpha'^*(\omega)) |\langle \tilde{T}_\omega \rangle|^2 = \langle \tilde{T}_\omega^* \rangle + \langle \tilde{T}_\omega \rangle. \quad (13.12)$$

If we now substitute (13.9) and (13.10) into (13.11) and (13.12) and we use the well known algebraic identity

$$z = \frac{z + z^*}{2} + i \frac{z - z^*}{2i}, \quad (13.13)$$

we obtain an expression for the dynamic thermal tortuosity

$$\text{Re}[\alpha'(\omega)] = \frac{\langle |\mathbf{T}_\omega|^2 \rangle}{|\langle \mathbf{T}_\omega \rangle|^2} + \frac{\nu}{2i\omega \text{Pr}} \frac{\langle \mathbf{T}_\omega^* \nabla^2 \mathbf{T}_\omega - \mathbf{T}_\omega \nabla^2 \mathbf{T}_\omega^* \rangle}{|\langle \mathbf{T}_\omega \rangle|^2}, \quad (13.14a)$$

$$\text{Im}[\alpha'(\omega)] = \frac{\nu}{2\omega \text{Pr}} \frac{\langle \mathbf{T}_\omega^* \nabla^2 \mathbf{T}_\omega + \mathbf{T}_\omega \nabla^2 \mathbf{T}_\omega^* \rangle}{|\langle \mathbf{T}_\omega \rangle|^2}, \quad (13.14b)$$

in which the dimensions have been reintroduced. From (13.5) we notice that the high-frequency solution of the microscopic closure problem for the excess temperature is $i\tilde{T}_\infty = 1$, which means that the excess temperature is constant over the bulk of the pore and out of phase with respect to the external source when $\delta' \rightarrow 0$, i.e., when $\omega \rightarrow \infty$. From (13.14) we observe that the high-frequency limit for the real part of the dynamic tortuosity

is therefore always equal to one. For high enough frequencies the adiabatic thermal problem is confined into a thermal boundary layer which is small compared to the dimensions of the pore. Substituting the classical temperature profile of a flat-wall thermal boundary layer

$$\tilde{T}_\omega = \tilde{T}_\infty \left(1 - e^{-\sqrt{i}n}\right), \quad (13.15)$$

in (13.14), we obtain

$$\operatorname{Re}[\alpha'(\omega)] = 1 + \frac{\delta'}{\Lambda'}, \quad (13.16a)$$

$$\operatorname{Im}[\alpha'(\omega)] = \frac{\delta'}{\Lambda'}, \quad (13.16b)$$

where

$$\frac{2}{\Lambda'} = \frac{A_{fs}}{V_f}, \quad (13.17)$$

is a characteristic thermal length, analogous of the Kozeny-Karman radius. The normalized dynamic thermal permeability $\tilde{k}'(\omega)$ can be written

$$\lim_{\omega \rightarrow \infty} \tilde{k}'(\omega) = -i\tilde{\omega} + \frac{1}{2}(1+i)\sqrt{M'}\tilde{\omega}^{-\frac{3}{2}}, \quad (13.18)$$

where

$$M' = \frac{8k'_0}{\phi\Lambda'^2}. \quad (13.19)$$

§ 14 Conclusions

In the present Chapter we studied the upscaling problem for the visco-thermal dissipation in porous materials. In § 10 we derived, in the framework of homogenization theory, the macroscopic equations for the visco-thermal dissipation in porous media, starting from the microscopic equations for the fluid and the solid phase described in § 9. We proved that, when the separation of length scales constraint is satisfied, then it is possible to uncouple the elastic, the viscous, and the thermal problems. In § 11 we

defined the macroscopic parameters of the viscous and thermal macroscopic dynamic laws in terms of the microscopic fields defined on the microgeometry of the porous medium. In § 12, we showed that, for the simple tube flow problem, the uncoupling of the viscous and thermal problems is justified when the ratio between the microscopic and the macroscopic length scales is order 10^{-2} , a condition fulfilled by many porous materials. In § 13, we discussed the high frequency thermal dynamic behavior.

CHAPTER III

ON THE VISCOUS LENGTH SCALE OF WEDGE-SHAPED POROUS MEDIA¹

This work revisits some numerical computations by Kostek et al. [Kostek S, Schwartz LM, Johnson DL Phys. Rev. B 1992;45:186], Smeulders et al. [Smeulders DMJ, Van Hassel RR, Van Dongen MEH, Jansen JKM. Int. J. Engng. Sci. 1994;32(6):979], and Firdaouss et al. [Firdaouss M, Guermond JL, Lafarge D. Int. J. Engng. Sci. 1998;36:1035]. It concerns the acoustic properties of 2D porous media whose internal surface contains sharp-edged wedges. We especially focus on the viscous length parameter Λ of these porous media, as Firdaouss et al. reported discrepancies between their Λ computations and the ones by Smeulders et al., which has consequences for the behavior of Johnson's shape factor M . Using Schwartz-Christoffel Transformations, we found that M remains of the order of unity if the pore throat is pinched by a wedge of constant angle, which confirms the Finite-Element computations by Firdaouss et al. Discrepancies with respect to the Finite-Element computations by Kostek et al., however, remain.

§ 15 Introduction

Wave propagation through porous media is of a capital importance for many application fields. With air as the pore fluid, applications can be found in

¹published in Int. J. Engng Sci.

noise control and modelling of sound absorbing materials. In the oil industry, acoustic borehole logging is an example of wave propagation through liquid-saturated porous media. A borehole is drilled in a potential hydrocarbon reservoir and probed with an acoustic tool. The inversion process then comprises the delineation of the reservoir properties from the acoustic signals. We assume that the pore fluid motions can be described at the microscopic level by the incompressible Stokes flow equations. By means of averaging methods, such as the homogenization theory (Lévy, 1979), it is possible to build effective medium theories, provided that we introduce two hypotheses on the separation of the length scales, viz., we firstly assume that the characteristic length of the pores is much smaller than the characteristic length scale of the representative elementary volume, and secondly we assume that the characteristic wave length is much larger than the characteristic length of the pore space. Moreover, we assume that the Reynolds number characterizing the flow is small so we can neglect all the deviations due to the non-linearities of the flow. An important aspect of these effective medium theories is the permeability k , i.e., the macroscopic consequence of the microscopic fluid-solid interaction. When the fluid saturating the porous medium is submitted to a macroscopic pressure gradient $\nabla \langle p \rangle$, we find the classical Darcy's law to express the linear proportionality between $\nabla \langle p \rangle$ and the macroscopic fluid velocity $\langle \mathbf{u} \rangle$. The symbol $\langle \cdot \rangle$ denotes a spatial average over the fluid phase. Considering a harmonic dependence on time of the form $\exp(i\omega t)$, the classical Darcy's law transforms into a complex-valued linear relationship:

$$\frac{\eta\phi}{k(\omega)} \langle \hat{\mathbf{u}} \rangle = -\nabla \langle \hat{p} \rangle, \quad (15.1)$$

where η is the dynamic viscosity and ϕ the porosity. The limit of the dynamic permeability $k(\omega)$ for $\omega \rightarrow 0$ is the classical Darcy steady-state real-valued permeability k_0 . Here it is understood that we are focussing only on the isotropic case formalism, the anisotropic extension being rather cumbersome and not giving any more insight. We can also introduce the dynamic tortuosity $\alpha(\omega)$:

$$i\omega\rho_f\alpha(\omega) \langle \hat{\mathbf{u}} \rangle = -\nabla \langle \hat{p} \rangle, \quad (15.2)$$

with the obvious relationship: $i\omega\rho_f\alpha(\omega) = \eta\phi/k(\omega)$. The limit of $\alpha(\omega)$ for $\omega \rightarrow \infty$ is the real-valued tortuosity (Johnson *et al.*, 1987):

$$\alpha_\infty = \frac{\langle |\mathbf{u}_p|^2 \rangle}{\langle |\mathbf{u}_p| \rangle^2}, \quad (15.3)$$

where \mathbf{u}_p is the velocity resulting from a potential problem. We note that since the boundary layer $\delta(\omega) = \sqrt{2\eta/\rho_f\omega}$ is arbitrary small for high enough frequencies, the walls of the pore appear to be flat in the boundary region. Then it is possible to write a second order approximation for the high frequency limit of $\alpha(\omega)$ (Johnson *et al.*, 1987):

$$\lim_{\omega \rightarrow \infty} \alpha(\omega) = \alpha_\infty \left[1 + (1-i)\frac{\delta(\omega)}{\Lambda} \right], \quad (15.4)$$

where Λ is the viscous length scale, defined as a velocity-weighted pore volume (V)-to-pore surface (S) ratio:

$$\frac{2}{\Lambda} = \frac{\int |\mathbf{u}_p|^2 dS}{\int |\mathbf{u}_p|^2 dV}. \quad (15.5)$$

Johnson *et al.* (1987) proposed to write Λ as a combination of the tortuosity, porosity and steady-state permeability, by the introduction of a so-called shape factor M :

$$\Lambda = \sqrt{\frac{12\alpha_\infty k_0}{\phi M}}. \quad (15.6)$$

Moreover, they suggested M to be 1, at least approximately. For 3D flows the factor 12 must be replaced by a factor 8. It was noted that M is of paramount importance for the modelling of dynamic flow behavior (Johnson *et al.*, 1987; Smeulders *et al.*, 1992).

In 1994, Smeulders *et al.* (1994) showed that M could substantially deviate from unity for wedge-shaped pore geometries. A schematic of such geometries is given in figure 16.1. The flow channel is partially obstructed

by wedges of angle $\gamma\pi$ leaving a pore throat opening aL_w . Previous considerations on these geometries were already presented by Kostek *et al.* (1992) for fluid permeability predictions. Smeulders *et al.* (1994) found high M -values for both the cases of small γ and small a using a Schwartz-Christoffel technique in their computations. In 1998, Firdaouss *et al.* (1998), using a Finite-Element method, claimed that M only deviated substantially from unity for small γ -values and not for small a -values. As the α_∞ and k_0 computations in Firdaouss *et al.* (1998) and Smeulders *et al.* (1994) were equal, the difference was caused by the Λ calculations according to (15.5). We will correct a mistake in the original computations (Smeulders *et al.*, 1994), and show that this leads to a perfect agreement with the results by Firdaouss *et al.* (1998). Discrepancies with respect to the Kostek *et al.* (1992) results, however, remain. Moreover, we will introduce an alternative method for the Λ computations, confirming these findings.

§ 16 Wedge-shaped geometries

Numerical calculations are performed on the polygonal periodic cell $P_1 \dots P_7$, depicted in figure 16.1. Indicated in figure 16.1 are the x_1 - and x_2 -axes. The distance between P_5 and P_6 , $d(P_5, P_6) = d(P_1, P_7) = HL_w$. The distance $d(P_1, P_5) = d(P_6, P_7) = L_w$. The wedge $P_2P_3P_4$ is defined by the parameters $0 < b < 1$ and $0 \leq h < H$. For various b and h values we will now compute α_∞ and Λ . In the two-dimensional case, we may write from (15.3) and (15.5):

$$\alpha_\infty = A_w \iint |\mathbf{u}_p|^2 dA_w / \left[\iint u_{p1} dA_w \right]^2 \quad (16.1)$$

$$\frac{2}{\Lambda} = \int_{P_1}^{P_5} |\mathbf{u}_p|^2 |dw| / \iint |\mathbf{u}_p|^2 dA_w, \quad (16.2)$$

where A_w denotes the pore area enclosed by the polygon $P_1 \dots P_7$, and u_{p1} is the x_1 -component of \mathbf{u}_p . The line integral in the numerator of (16.2) is over the pore wall $P_1P_2P_3P_4P_5$. Obviously, $|dw| = (dx_1^2 + dx_2^2)^{1/2}$. We thus aim to solve the steady potential flow problem $\mathbf{u}_p = \nabla_y \psi$, where $\psi = \psi_0 = 0$

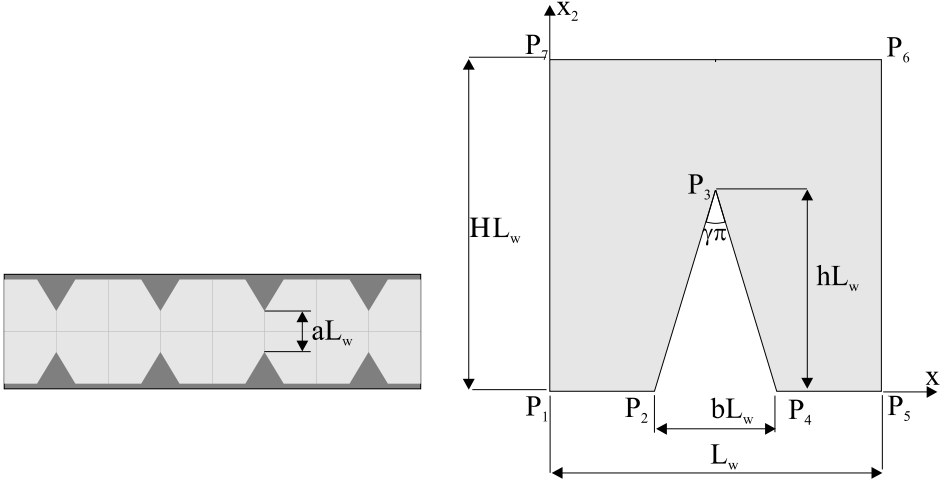


Figure 16.1: *Geometry of 2D channel with intrusive wedges (left). Geometry of the periodic cell (right).*

at line element P_1P_7 and $\psi = \psi_L$ at line element P_5P_6 . The inflow and outflow are perpendicular to line elements P_1P_7 and P_5P_6 (see figure 16.1). We shall rewrite (16.1) by considering an incompressible flow at microscale:

$$|\mathbf{u}_p|^2 = \nabla_y \cdot (\psi \cdot \nabla_y \psi) \quad (16.3)$$

Integration over the pore area A_w and application of Green's theorem yields:

$$\iint |\mathbf{u}_p|^2 dA_w = \oint_c \left(\psi \frac{\partial \psi}{\partial x_1} dx_2 - \psi \frac{\partial \psi}{\partial x_2} dx_1 \right), \quad (16.4)$$

where c is the contour $P_1 \dots P_7$. Evaluation of the RHS of (16.4) yields:

$$\iint |\mathbf{u}_p|^2 dA_w = Q\psi_L, \quad (16.5)$$

where we have introduced the flow rate $Q = \int_{P_5}^{P_6} u_{p1} dx_2 = - \int_{P_7}^{P_1} u_{p1} dx_2$. For the integral in the denominator of (16.1) we may write:

$$\iint u_{p1} dA_w = \iint u_{p1} dx_2 dx_1 = Q \int dx_1 = QL_w. \quad (16.6)$$

We are now able to rewrite (16.1):

$$\alpha_\infty = \frac{\psi_L^2}{L_w^2} \frac{A_w}{\iint |\mathbf{u}_p|^2 dA_w}. \quad (16.7)$$

In order to solve the integrals in (16.2) and (16.7), we will apply the conformal transformation technique.

§ 17 Schwartz–Christoffel Transformations

Although the Schwartz-Christoffel Transformations were described in a previous paper (Smeulders *et al.*, 1994), we would like to revisit them as they are treated in more detail here, and moreover, a mistake in Smeulders *et al.* (1994) is corrected. In general, a conformal mapping function $f : G_z \rightarrow G_w$; $G_z, G_w \subset \mathbb{C}$, transforms the region G_z into the region G_w . A schematic of the regions is presented in figure 17.1. G_w is identified as the pore geometry defined in figure 16.1, and G_z as the region bounded by the unit circle. Moreover, a third rectangular region G_v is defined, which results from the transformation of G_z through the mapping function g . We therefore notice that

$$(g \circ f^{-1})(w) = g(z) = v, \quad (17.1)$$

$$(f \circ g^{-1})(v) = f(z) = w. \quad (17.2)$$

The mapping functions f and g are assumed analytic and bijective and have nonzero complex derivatives over their entire domain. Such mappings preserve the angles between intersecting arcs in the domain and image

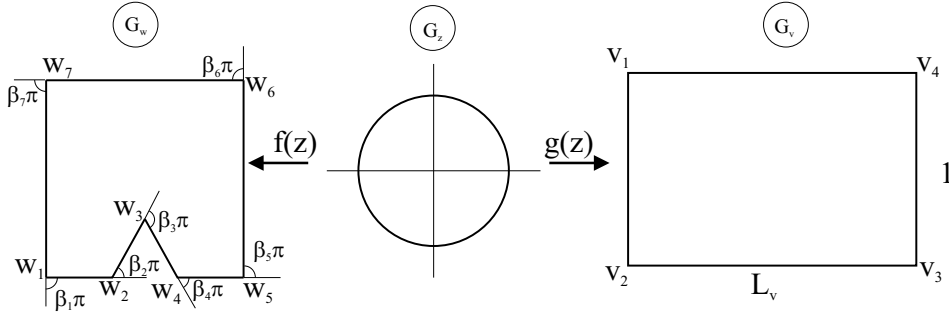


Figure 17.1: *Complex domains used for the conformal mapping calculations.*

regions. The Riemann Mapping Theorem (Henrici, 1991) asserts that any simply connected region in \mathbb{C} can be mapped in this way onto any other such region. For the pore geometry G_w , the coordinates of the vertices w_1, \dots, w_7 are given by $w_1 = 0$, $w_2 = \frac{1}{2}(1-b)L_w$, $w_3 = (\frac{1}{2} + ih)L_w$, $w_4 = \frac{1}{2}(1+b)L_w$, $w_5 = L_w$, $w_6 = (1+i)HL_w$, $w_7 = iHL_w$, with $0 \leq b < 1$ and $0 \leq h < H$. For each $0 \leq k \leq 7$, we denote $\beta_k^f \pi$ the angle of w_k , where $-1 \leq \beta_k^f < 1$ (see figure 17.1). Positive angles are counterclockwise. We thus have the simple relationship

$$\sum_{k=1}^7 \beta_k^f = -2.$$

The analytic function f , conformally mapping G_z onto G_w may now be written in the form (Henrici, 1991):

$$w = f(z) = w_c + C^f \int_0^z \prod_{k=1}^7 \left(1 - \frac{z'}{z_k^f}\right)^{\beta_k^f} dz', \quad (17.3)$$

for a suitable choice of parameters $\{z_k^f \mid |z_k^f| = 1\}$, C^f and w_c . Please note that the parameters z_k^f are numbered in counterclockwise order. To determine the map uniquely, the complex values w_c and C^f are fixed. The

simplicity of the explicit formula (17.3) is attractive. The inverse mapping $z = f^{-1}(w)$ is also a conformal mapping and may be thought as a solution of an ordinary differential equation in one complex variable w :

$$\frac{dz}{dw} = \frac{1}{C^f} \prod_{k=1}^7 \left(1 - \frac{z}{z_k^f}\right)^{-\beta_k^f}. \quad (17.4)$$

In general, the inverse mapping $z = f^{-1}(w)$ is computed numerically (Trefethen, 1979). On the unit circle is thus obtained $z_k^f = f^{-1}(w_k)$, with $|z_k^f| = 1$ and $k = 1, \dots, 7$.

The rectangular region $G_v \subset \mathcal{C}$ is defined by its vertices $v_1 = g(z_7) = i$, $v_2 = g(z_1) = 0$, $v_3 = g(z_5) = L_v$ and $v_4 = g(z_6) = L_v + i$. The aspect ratio $0 < L_v \in \mathbb{R}$ obviously depends on the geometry of G_w , i.e., on b , h , and H . The choice for L_w does not affect L_v , which means that any congruent polygonal is mapped onto the same rectangle G_v . The analytic function g may be written in the form:

$$v = g(z) = v_c + C^g \int_0^z \prod_{k=1}^4 \left(1 - \frac{z'}{z_k^g}\right)^{\beta_k^g} dz', \quad (17.5)$$

where the parameters v_c and C^g are fixed. Also the vertices v_k , $k = 1, \dots, 4$, are computed numerically (Trefethen, 1979).

Since the fluid may be regarded incompressible and irrotational on the microscopic level, the potential ψ is harmonic, i.e., it satisfies the Laplace equation $\Delta\psi = 0$. We may also define the conjugate harmonic function ζ satisfying the Laplace equation and the Cauchy–Riemann equations $\partial\psi/\partial x_2 = \partial\zeta/\partial x_1$, $-\partial\psi/\partial x_1 = \partial\zeta/\partial x_2$. The function $\theta(w) = \psi(w) + i\zeta(w)$ is called the complex potential on G_w and satisfies the Laplace equation on G_w ,

$$\Delta_w \theta(w) = 0. \quad (17.6)$$

In G_v , the complex potential Ω is given by $\Omega(v) = v\Omega_L/L_v$, with $\Omega = 0$ at v_1v_2 and $\Omega = \Omega_L$ at v_3v_4 . Using (17.1), the complex potential θ on G_w is

given by

$$\theta(w) = \Omega\left((g \circ f^{-1})(w)\right) = \frac{\Omega_L}{L_v}\left(g \circ f^{-1}\right)(w). \quad (17.7)$$

For the velocity, we know that

$$|\mathbf{u}_p|^2 = |\theta'(w)|^2 = \frac{\Omega_L^2}{L_v^2} |(g \circ f^{-1})'(w)|^2, \quad (17.8)$$

where the $'$ denotes the derivative with respect to the relevant variable, i.e., w in this case. Using (17.1) and (17.2), the expression for the velocity may be rewritten in the G_z region:

$$|\mathbf{u}_p|^2 = \frac{\Omega_L^2}{L_v^2} \left| \frac{g'(z)}{f'(z)} \right|^2, \quad (17.9)$$

where the $'$ refers to a derivation with respect to z in this case. This means that the line integral in the numerator of (16.2) now becomes:

$$\int_{w_1}^{w_5} |\mathbf{u}_p|^2 |dw| = \frac{\Omega_L^2}{L_v^2} \int_{z_1}^{z_5} \frac{|g'(z)|^2}{|f'(z)|} |dz| \quad (17.10)$$

Substitution of the expressions for g' and f' , obtained from (17.3) and (17.5), yields:

$$\begin{aligned} \int_{w_1}^{w_5} |\mathbf{u}_p|^2 |dw| &= \frac{\Omega_L^2}{L_v^2} \frac{|C^g|^2}{|C^f|} \\ &\cdot \int_{z_1}^{z_5} \left| \frac{[(1 - z/z_1)(1 - z/z_5)(1 - z/z_6)(1 - z/z_7)]^{-1/2}}{(1 - z/z_2)^{\beta_2}(1 - z/z_3)^{\beta_3}(1 - z/z_4)^{\beta_4}} \right| |dz|, \end{aligned} \quad (17.11)$$

where we have used that $z_1^g = z_7^f$, $z_2^g = z_1^f$, $z_3^g = z_5^f$, and $z_4^g = z_6^f$. In (17.11), the superscripts f in z_k and β_k are implicitly understood. A scaling factor is involved here, as we found that $|C_f|$ is linearly proportional to L_w . Because

of the symmetry of G_w (see figure 17.1), we find that $\beta_2 = \beta_4 = -\beta_3/2 < 0$. Consequently, the integrand of (17.11) has singularities in z_k , $k = 1, 3, 5, 6, 7$. As the singularities in z_6 and z_7 are not in the integration domain, they are of no further concern. The remaining singularities are integrable, as we will see.

Performing the transformation $G_w \rightarrow G_v$, for the area integral in G_w the integrand (17.8) has to be multiplied by $|J| = |(f \circ g^{-1})'(v)|^2$, which can also be written as $|J| = |(g \circ f^{-1})'(w)|^{-2}$. We obtain:

$$\iint_{G_w} |\mathbf{u}_p|^2 dA_w = \frac{\Omega_L^2}{L_v^2} \iint_{G_v} dA_v = \frac{\Omega_L^2}{L_v^2} A_v = \frac{\Omega_L^2}{L_v}. \quad (17.12)$$

In the last step of (17.12), we have used that L_v and A_v are equal, because the height of G_v is always 1. Substituting (17.11) and (17.12) into (16.2), we may now write for the length scale parameter:

$$\frac{2}{\Lambda} = \frac{1}{L_v} \frac{|C^g|^2}{|C^f|} \int_{z_1}^{z_5} \left| \frac{[(1 - z/z_1)(1 - z/z_5)(1 - z/z_6)(1 - z/z_7)]^{-1/2}}{(1 - z/z_2)^{\beta_2}(1 - z/z_3)^{\beta_3}(1 - z/z_4)^{\beta_4}} \right| |dz|. \quad (17.13)$$

Unfortunately, the term $1/L_v$ in (17.13) was not present in the previous paper (Smeulders *et al.*, 1994), which caused the differences reported by Firdaouss *et al.* (1998). For the tortuosity, we infer from (16.7) that

$$\alpha_\infty = \frac{\psi_L^2}{\Omega_L^2} \frac{L_v}{L_w^2} A_w. \quad (17.14)$$

Setting $\psi_L = \Omega_L = 1$, we arrive at the expression reported previously (Smeulders *et al.*, 1994). In the limiting case for $b = h \rightarrow 0$ (no wedge), we find that $L_v = 1/H$, which means that from (17.14) it can be seen that $\alpha_\infty = 1$.

§ 18 Numerical results

Using the identity $z = e^{i\varphi}$, where $0 = \varphi_7 < \varphi_1 < \dots < \varphi_6 < \pi$, we obtain for the length scale parameter:

$$\frac{2}{\Lambda} = \frac{1}{4A_v} \frac{|C^g|^2}{|C^f|} \cdot \int_{\varphi_1}^{\varphi_5} \frac{|\sin \frac{1}{2}(\varphi - \varphi_1) \sin \frac{1}{2}(\varphi - \varphi_5) \sin \frac{1}{2}(\varphi - \varphi_6) \sin \frac{1}{2}(\varphi - \varphi_7)|^{-1/2}}{|\sin \frac{1}{2}(\varphi - \varphi_2)|^{\beta_2} |\sin \frac{1}{2}(\varphi - \varphi_3)|^{\beta_3} |\sin \frac{1}{2}(\varphi - \varphi_4)|^{\beta_4}} d\varphi. \quad (18.1)$$

Because of the symmetry of the problem, i.e., $\int_{\varphi_1}^{\varphi_2} \dots d\varphi = \int_{\varphi_4}^{\varphi_5} \dots d\varphi$, and $\int_{\varphi_2}^{\varphi_3} \dots d\varphi = \int_{\varphi_3}^{\varphi_4} \dots d\varphi$, we only need to evaluate two integrals, say

$$\int_{\varphi_1}^{\varphi_2} \frac{f_1(\varphi)}{\sin^{1/2} \frac{1}{2}(\varphi - \varphi_1)} d\varphi \quad \text{and} \quad \int_{\varphi_3}^{\varphi_4} \frac{f_2(\varphi)}{\sin^{\beta_3} \frac{1}{2}(\varphi - \varphi_3)} d\varphi, \quad (18.2)$$

where we have made explicit the singularities in $\varphi = \varphi_1$ and $\varphi = \varphi_3$. The functions f_1 and f_2 do not contain any singularities and are defined as follows:

$$f_1(\varphi) = \frac{\sin^{-\beta_2} \frac{1}{2}(\varphi_2 - \varphi) \sin^{-\beta_4} \frac{1}{2}(\varphi_4 - \varphi)}{\{\sin \frac{1}{2}(\varphi_5 - \varphi) \sin \frac{1}{2}(\varphi_6 - \varphi) \sin \frac{1}{2}(\varphi - \varphi_7)\}^{1/2}} \frac{1}{\sin^{\beta_3} \frac{1}{2}(\varphi_3 - \varphi)}, \quad (18.3)$$

$$f_2(\varphi) = \frac{\sin^{-\beta_2} \frac{1}{2}(\varphi - \varphi_2) \sin^{-\beta_4} \frac{1}{2}(\varphi_4 - \varphi)}{\{\sin \frac{1}{2}(\varphi_5 - \varphi) \sin \frac{1}{2}(\varphi_6 - \varphi) \sin \frac{1}{2}(\varphi - \varphi_7)\}^{1/2}} \frac{1}{\sin^{1/2} \frac{1}{2}(\varphi - \varphi_1)}. \quad (18.4)$$

The singularities in the two integrals of (18.2) are overcome by splitting both integrands into two parts each. The second integrand in (18.2), for example, can be split into the parts $(f_2(\varphi) - f_2(\varphi_3))/\sin^{\beta_3} \frac{1}{2}(\varphi - \varphi_3)$ and $f_2(\varphi_3)/\sin^{\beta_3} \frac{1}{2}(\varphi - \varphi_3)$. As the limit of the first part now goes to zero for $\varphi \rightarrow \varphi_3$, it can be evaluated numerically. We used a trapezium rule with iterative step refining to obtain an accuracy better than 10^{-5} .

The second part $f_2(\varphi_3)/\sin^{\beta_3} \frac{1}{2}(\varphi - \varphi_3)$ can be written as a binomial series expansion in $z = \frac{1}{2}(\varphi - \varphi_3)$ for $z < \pi$ (Abramowitz & Stegun, 1970):

$$\begin{aligned} \frac{1}{\sin^{\beta_3} z} &= \left(\frac{1}{z}\right)^{\beta_3} + \frac{\beta_3}{6} z^{2-\beta_3} + \frac{\beta_3(5\beta_3+2)}{360} z^{4-\beta_3} \\ &\quad + \frac{\beta_3(35\beta_3^2+42\beta_3+16)}{45360} z^{6-\beta_3} + O(z^{8-\beta_3}). \end{aligned} \quad (18.5)$$

Straightforward termwise integration by hand of the above relation yields the integral of the second part as a series expansion. Also here the accuracy is better than 10^{-5} . We checked our computations against the MATHEMATICATM package, which can handle (18.1) directly. Because of the symmetry of the problem, the integration was performed over the domain from φ_1 to φ_3 , and a substitution of the form $t = \sin \frac{1}{2}(\varphi - \varphi_3)$ was used. The results were in perfect agreement. In the limiting case for $b = h \rightarrow 0$, we find that

$$|C^g| \int_{\varphi_1}^{\varphi_5} \frac{|\sin \frac{1}{2}(\varphi - \varphi_1) \sin \frac{1}{2}(\varphi - \varphi_5) \sin \frac{1}{2}(\varphi - \varphi_6) \sin \frac{1}{2}(\varphi - \varphi_7)|^{-1/2}}{|\sin \frac{1}{2}(\varphi - \varphi_2)|^{\beta_2} |\sin \frac{1}{2}(\varphi - \varphi_3)|^{\beta_3} |\sin \frac{1}{2}(\varphi - \varphi_4)|^{\beta_4}} d\varphi = \frac{4}{H}, \quad (18.6)$$

and that $|C^g|/|C^f| = 1/HL_w$. This means that from (18.1) it can be inferred that $\Lambda = 2HL_w$, which is twice the pore volume-to-surface ratio as predicted by (15.5).

Our Scharz-Christoffel transformations are now compared with the Finite-Element computations by Firdaouss *et al.* (1998) and Kostek *et al.* (1992). In the former case the dimensions of the wedge are varied, whereas the height of the unit cell H is kept constant ($H = 1$). In the latter case, a Koch-curve based geometry is used, where the wedge has equal sides ($b = 1/3; h = \sqrt{3}/6$), and H is varied. From table 18.1 we notice that there is a perfect agreement with the Firdaouss *et al.* (1998) results. We would like to remark however, that the Schwartz-Christoffel Transformations imply a significant reduction in computation time over the Finite-Element procedure described by Firdaouss *et al.* (1998). A graphical representa-

b	Λ/L_w for $h = b$		Λ/L_w for $h = 0.5$	
	present	Firdaouss <i>et al.</i> (1998)	present	Firdaouss <i>et al.</i> (1998)
0.00	2.	2.	0.	0.
0.01	1.913	1.915	0.015	
0.02	1.833		0.031	
0.05	1.627		0.076	
0.10	1.369	1.373	0.149	0.151
0.15	1.183		0.219	
0.20	1.044	1.047	0.287	0.288
0.25	0.937		0.350	
0.30	0.852	0.855*	0.410	0.412
0.40	0.719	0.728	0.519	0.516
0.50	0.612	0.616	0.612	0.616
0.60	0.516	0.525	0.692	0.693
0.70	0.422	0.423	0.760	0.765
0.80	0.323	0.325	0.817	0.822
0.90	0.205	0.207	0.864	0.870
0.92	0.177	0.177	0.873	
0.94	0.145	0.146	0.881	
0.96	0.109	0.111	0.889	
0.98	**	0.066		
0.988	**	0.046		

Table 18.1: A comparison of Λ parameters for $H = 1.0$. *: corrected typo in Firdaouss et al. (1998). **: configuration could not be mapped numerically.

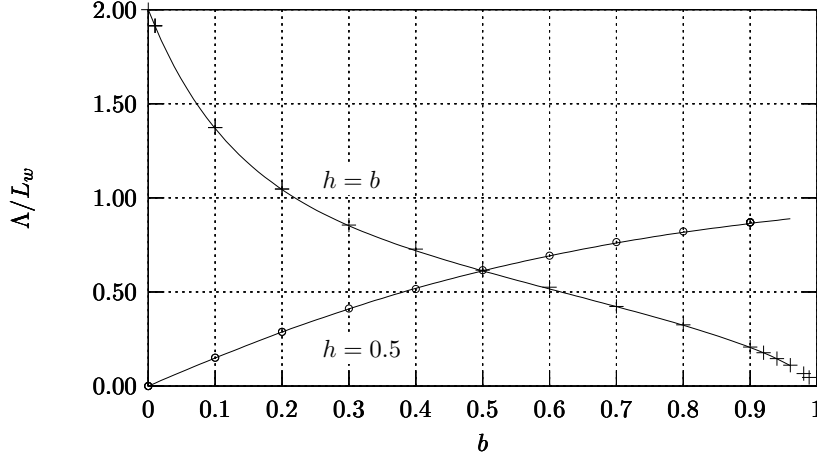


Figure 18.1: Characteristic length scale Λ/L_w as a function of b for $h = 0.5$ (o), and $h = b$ ($+$). The curves represent the present results, whereas the markers represent the results from Firdaouss *et al.* (1998).

tion of the Λ -parameter is given in figure 18.1. We notice that Λ tends to zero for pinched pore throats ($b \rightarrow 1$, $h = b$), and in the limit of sharp wedge angles ($b \rightarrow 0$, $h = 0.5$). It was calculated by Firdaouss *et al.* (1998) that only in the latter case $M \rightarrow \infty$, as can be seen from (15.6), because α_∞ and k_0 are virtually not affected by $b \rightarrow 0$ (Firdaouss *et al.*, 1998; Smeulders *et al.*, 1994). In the former case, they calculated that M remains of the order of unity, and $\Lambda \rightarrow 0$ is caused by $k_0 \rightarrow 0$ Firdaouss *et al.* (1998); Smeulders *et al.* (1994). From table 18.2, we notice that there is a significant discrepancy with respect to the Kostek *et al.* (1992) results. This is probably due to the relatively coarse mesh used by Kostek *et al.* in their Finite-Element computations. Indeed, as it was shown by Firdaouss *et al.* (1998), an accurate refinement of the mesh around the tip of the edge is needed in order to obtain the correct value for Λ . Please note that the unit length used in Kostek *et al.* (1992) equals $\sqrt{3}L_w/486$.

H	Λ/L_w for $b = 1/3$; $h = \sqrt{3}/6$	
	present	Kostek <i>et al.</i> (1992)
1.0	0.94974	
0.8	0.72957	
0.6	0.50598	
0.4	0.25348	
$16\sqrt{3}/81$	0.15444	0.2310
$15\sqrt{3}/81$	0.10762	0.1637
0.3	0.04930	
$14\sqrt{3}/81$	0.04719	0.0892

Table 18.2: A comparison of Λ parameters for variable H . The unit length used in Kostek *et al.* (1992) equals $\sqrt{3}L_w/486$.

§ 19 Pore variation technique

In 1992, Smeulders *et al.* (1992) derived an alternative expression for the characteristic length Λ based on small pore variations. Introducing the formation factor $F = \alpha_\infty/A_w$, and using (16.7), their relation can be written as:

$$\frac{2}{\Lambda_\phi} = - \frac{\left(\frac{\partial}{\partial r} \iint |\mathbf{u}_p|^2 dA_w \right)_{\nabla\Psi}}{\iint |\mathbf{u}_p|^2 dA_w} = \frac{1}{F} \left(\frac{\partial F}{\partial r} \right)_{\nabla\Psi}, \quad (19.1)$$

where dr is defined as a inward displacement of the pore walls in the normal direction at constant flow potential gradient $\nabla\Psi$. After some manipulations, (19.1) can be shown identical to

$$\frac{2}{\Lambda_\phi} = \frac{1}{A_w} \frac{\partial A_w}{\partial r} \frac{\partial \ln F}{\partial \ln A_w} = - \frac{S}{A_w} \frac{\partial \ln F}{\partial \ln A_w}, \quad (19.2)$$

as for infinitesimal variations $dA_w = -S dr$, where S is the pore wall surface $P_1 P_2 P_3 P_4 P_5$. Relation (19.2) appears to be the 2D version of an expression presented by Johnson *et al.* Johnson *et al.* (1986). We used a second order

backward difference scheme to compute Λ_ϕ from (19.1):

$$\frac{2}{\Lambda_\phi} = \frac{1}{F_0} \frac{3F_0 - 4F_{-1} + F_{-2}}{2\Delta r}, \quad (19.3)$$

where Δr is $5 \cdot 10^{-4}$ and F_i is computed from Schwartz–Christoffel Transformations. It is understood that P_2 translates over $\Delta r((\cos \beta - 1)/\sin \beta + i)$, P_3 over $i\Delta r/\cos \beta$, and P_4 over $\Delta r((1 - \cos \beta)/\sin \beta + i)$, where $\beta = -\beta_2\pi = -\beta_4\pi = \arctan(2b/h)$. We find that up to the fourth digit, the computed Λ_ϕ values are identical to the Λ values obtained earlier.

§ 20 Conclusions

We revisited the computations by Kostek *et al.* (1992), Smeulders *et al.* (1994), and Firdaouss *et al.* (1998) concerning the viscous length scale of wedge-shaped porous media. Correcting a mistake in Smeulders *et al.* (1994), we showed that the Finite-Element results of Firdaouss *et al.* (1998) and the conformal mapping results of Smeulders *et al.* (1994) are now in perfect agreement. This implies that the viscous length goes to zero both in the limit of sharp wedges, and in the limit of pinched pore throats. However, in the former case the shape factor M , used in modelling dynamic flow behavior, deviates significantly from unity, whereas in the latter case it does not. Significant discrepancies were found with respect to the results of Kostek *et al.* (1992) for a Koch-curve based geometry. This is probably due to the relatively coarse mesh used in the Finite-Element computations of Kostek *et al.* (1992). Moreover, we applied a pore variation technique to compute Λ . These results fully confirm the previous findings.

CHAPTER IV

INFLUENCE OF PORE ROUGHNESS ON HIGH-FREQUENCY PERMEABILITY¹

The high-frequency behavior of the fluid velocity patterns for smooth and corrugated pore channels is studied. The classical approach of Johnson, D., Koplik, J., and Dashen, R. (1987, *J. Fluid Mech.* **176** pp. 379–402) for smooth geometries is obtained in different manners, thus clarifying differences with Sheng, P. and Zhou, M. (1988, *Phys. Rev. Lett.* **61**, No 14 pp. 1591–1594) and Avellaneda & Torquato (1991, *Phys. Fluids A* **3** (11) pp. 2529–2540) treatments. For wedge-shaped pore geometries, the classical approach is modified by a non-analytic extension proposed by Achdou, Y. and Avellaneda, M. (1992, *Phys. Fluids A* **4** (12) pp. 2561–2673) The dependency of the non-analytic extension on the apex angle of the wedge was derived. Precise numerical computations for various apex angles in two-dimensional channels confirmed this theoretical dependency, which is somewhat different from the original Achdou & Avellaneda predictions. Moreover, it was found that the contribution of the singularities does not alter the parameters of the classical theory by Johnson et al.

§ 21 Introduction

The problem of fluid flow through porous media is of paramount importance in many technological areas. In air-filled sound absorbing media, a

¹submitted to *Phys. Fluids*

precise prediction of sound absorption versus frequency is needed (Lafarge *et al.*, 1997). In the oil-industry, exploration wells are probed by acoustic tools and reservoir properties are delineated from the recorded wave trains (Wisse, 1999). The dynamic permeability $k(\omega)$, and the dynamic tortuosity $\alpha(\omega)$ are important properties to describe the macroscopic flow through porous media subjected to an oscillatory pressure gradient. Here, the term macroscopic refers to a length scale L_x that is much larger than any pore size L_y . L_x is defined as characteristic wavelength being the product of the fluid sound speed c_a , and an intrinsic viscous relaxation time L_y^2/ν , where ν is the kinematic viscosity of the pore fluid (Smeulders *et al.*, 1992; Lafarge *et al.*, 1997). Introducing an $\exp(i\omega t)$ dependence for the fluid pressure p and the macroscopic fluid velocity \mathbf{U} , $k(\omega)$ and $\alpha(\omega)$ are defined by:

$$\frac{\eta\phi}{k(\omega)}\hat{\mathbf{U}} = -\nabla\hat{p} \quad (21.1)$$

$$i\omega\rho\alpha(\omega)\hat{\mathbf{U}} = -\nabla\hat{p} \quad (21.2)$$

In these two expressions, η is the fluid viscosity, ρ is the fluid density, and ϕ is the porosity. These relations take into account, in an averaged sense, the fluid motion that takes place in the pore structure, so that $k(\omega)$ and $\alpha(\omega)$ depend on the morphology of the pore space. Johnson *et al.* (1987), and later Sheng & Zhou (1988), and Zhou & Sheng (1989) argued that the transition from low-frequency viscous behavior to high-frequency inertia behavior must be determined by the ratio π_1 of the length-scales $\sqrt{Fk_0}$ and δ . Here k_0 is the stationary Darcy permeability, and F is the formation factor, a non-dimensional parameter which is related to the effective electrical conductivity of the porous medium saturated with a conductive fluid. The viscous skin depth $\delta = \sqrt{2\nu/\omega}$. It was consequently postulated that $k(\omega)$ satisfies a universally valid scaling function

$$k(\omega) = k_0 f\left(\frac{Fk_0}{\delta^2}\right). \quad (21.3)$$

This also means that a characteristic frequency $\omega_c = \nu/Fk_0$ can be defined where the viscous forces and the inertia forces are of the same order of

magnitude. Experimental work by Charlaix *et al.* (1988), and Smeulders *et al.* (1992) show very good agreement of such theory on a wide variety of porous samples. Detailed theoretical analysis, however, showed that the structure function f of (21.3) must also depend on the ratio $\pi_2 = \delta/\Lambda$, where Λ is an electrically weighted pore volume-to-pore surface ratio (Johnson *et al.*, 1987). Surprisingly, for a wide variety of morphologies, π_1 and π_2 were found not to be independent, i.e., their product was found to be $\sqrt{1/8}$, at least approximately. These morphologies had in common that they were smooth on the pore scale, i.e., the pore surface had bounded curvature. The possibility of departure from the structure function f for corrugated morphologies was investigated by several authors such as Kostek *et al.* (1992), Smeulders *et al.* (1994), Firdaouss *et al.* (1998), and Cortis & Smeulders (2001). It appeared that high values for $\pi_1 \times \pi_2$ could be reached for special cases, but these investigations still did not consider any comparison over the frequency domain. In other words, only the assumption that $\pi_1 \times \pi_2 \approx \sqrt{1/8}$ was invalidated for some cases, but the structure function f could still be fully correct, if we rewrite it as a function of two parameters (Johnson *et al.*, 1987; Smeulders *et al.*, 1992):

$$k(\omega) = k_0 f\left(\frac{Fk_0}{\delta^2}, \frac{Fk_0}{\Lambda^2}\right). \quad (21.4)$$

In a paper by Achdou & Avellaneda (1992) however, departures from (21.4) were observed for micro-geometries consisting of corrugated tubes. For high frequencies, they observed a slower convergence of $k(\omega)$ to its asymptotic limit than predicted from universality theory. A non-analytic correction to the structure function (21.4) was proposed. The aim of this paper is to study this non-analytic correction factor. From microstructure, the dynamic permeability and tortuosity relations will be derived. Then, analyzing in detail the fluid velocity pattern in the bulk fluid and the boundary layer, the classical Johnson *et al.* (1987) high-frequency limit for smooth geometries will be obtained in different manners, making apparent the discrepancy with the Sheng & Zhou (1988) treatment, and clarifying the asymptotic boundary layer analysis proposed by Avellaneda & Torquato (1991). For microgeometries consisting of corrugated tubes, this leads to

a somewhat different high-frequency correction than proposed by Achdou & Avellaneda (1992). Furthermore, the theoretical predictions will be numerically evaluated for 2D channels that have wedge-shaped asperities.

§ 22 Oscillating Stokes flow

Considering the unsteady Stokes equation for the fluid velocity field \mathbf{v} , we may write

$$i\omega\rho\hat{\mathbf{v}} = -\nabla\hat{p} + \eta\nabla^2\hat{\mathbf{v}} + \hat{g}\mathbf{e}, \quad (22.1)$$

where \mathbf{e} is the unit vector (e_x, e_y, e_z) , and \hat{g} is a spatially uniform oscillating source term, which is expressed in Nm^{-3} . In Achdou & Avellaneda (1992), \hat{g} is an external oscillatory pressure gradient, which also appears quite naturally if the conventional technique of homogenization is used. Zhou & Sheng (1989), Smeulders *et al.* (1992), and Lafarge *et al.* (1997) denote this externally applied pressure gradient $-\nabla_x p_0$. Indeed, the actual pressure p in the fluid can be viewed as the sum of its local mean value $p_0 = \langle p \rangle$ and its deviatoric part $\hat{p} = p - \langle p \rangle$, where $\langle \cdot \rangle$ denotes averaging over the pore fluid volume V_f . The local mean value p_0 varies at the macroscopic length scale L_x , thus its gradient may be considered a spatial constant in V_f . The deviatoric part \hat{p} varies at the pore scale L_y and is a stationary field of zero mean value. This means that, on the average, it does not increase or decrease in the direction of \mathbf{e} . It is fluctuating at the microscopic level because of the pore geometry, but it does not change from place to place when averages are considered. For periodic microstructures, the stationary character of \hat{p} is expressed by periodic boundary conditions. Furthermore, it can be obtained from homogenization theory that, because of the scale separation $L_x \gg L_y$, the fluid is locally incompressible

$$\nabla \cdot \hat{\mathbf{v}} = 0. \quad (22.2)$$

Introducing the scaled velocity $\tilde{\mathbf{v}} = \eta\hat{\mathbf{v}}/\hat{g}$ expressed in m^2 , and the scaled pressure $\tilde{p} = \hat{p}/\hat{g}$ expressed in m , the unsteady Stokes problem may be

written

$$i\omega\tilde{\mathbf{v}}/\nu = -\nabla\tilde{p} + \nabla^2\tilde{\mathbf{v}} + \mathbf{e}, \quad (22.3a)$$

$$\nabla \cdot \tilde{\mathbf{v}} = 0, \quad (22.3b)$$

$$\tilde{\mathbf{v}} = 0 \quad \text{on the pore walls}, \quad (22.3c)$$

$$\tilde{p} : \text{ stationary}, \quad (22.3d)$$

where ν is the kinematic viscosity of the fluid. The solution to this problem can be expressed as a sum of normal modes (Avellaneda & Torquato, 1991):

$$\tilde{\mathbf{v}}(\mathbf{r}, \omega) = \sum_{n=1}^{\infty} b_n \mathbf{\Psi}_n(\mathbf{r}) \frac{\sigma_n}{1 + i\omega\sigma_n/\nu}, \quad (22.4a)$$

$$\tilde{p}(\mathbf{r}, \omega) = \sum_{n=1}^{\infty} b_n Q_n(\mathbf{r}) \frac{1}{1 + i\omega\sigma_n/\nu} + \Phi(\mathbf{r}). \quad (22.4b)$$

Here, the dimensionless vector eigenfunctions $\mathbf{\Psi}_n$ satisfy

$$-\nabla^2 \mathbf{\Psi}_n = \frac{1}{\sigma_n} (\mathbf{\Psi}_n - \nabla Q_n), \quad (22.5a)$$

$$\nabla \cdot \mathbf{\Psi}_n = 0, \quad (22.5b)$$

$$\mathbf{\Psi}_n = 0 \quad \text{on the pore walls}, \quad (22.5c)$$

$$Q_n : \text{ stationary}, \quad (22.5d)$$

and the parameters σ_n , expressed in m^2 , are the inverse eigenvalues of the Stokes operator. They determine the viscous relaxation times $\Theta_n = \sigma_n/\nu$ corresponding to purely damped modes $\tilde{\mathbf{v}} = \sigma_n \mathbf{\Psi}_n e^{-t/\Theta_n}$ as a solution to the homogeneous unsteady Stokes problem, i.e., with the external excitation term $g = 0$ in (22.3a). The functions Q_n , which are non-zero in general, have dimensions of length and determine the corresponding stationary pressures $\tilde{p} = Q_n e^{-t/\Theta_n}$. The largest value σ_1 is obviously of order $\mathcal{O}(L_y^2)$ and the parameters σ_n , sorted such that $\sigma_{n+1} < \sigma_n$, accumulate to 0 when $n \rightarrow \infty$. Using the conditions (22.5), it can be verified that the

eigenfunctions Ψ are orthogonal. They are complete in the subspace of the square integrable divergence-free fields having zero normal component on the pore walls. Furthermore, they are chosen orthonormal

$$\frac{1}{V_f} \int_{V_f} \Psi_n \cdot \Psi_m dV = \delta_{nm}. \quad (22.6)$$

The dimensionless expansion coefficients b_n are defined as

$$b_n = \frac{1}{V_f} \int_{V_f} \Psi_n \cdot \mathbf{e} dV. \quad (22.7)$$

Now substituting (22.4a) and (22.4b) in the Stokes equation (22.3a), we see that (22.3a) is verified if

$$\sum_{n=1}^{\infty} b_n \Psi_n = \mathbf{e} - \nabla \Phi. \quad (22.8)$$

Note that there is a unique solution \mathbf{E}, Φ to the following electric problem

$$\mathbf{E} = \mathbf{e} - \nabla \Phi, \quad (22.9a)$$

$$\nabla \cdot \mathbf{E} = 0, \quad (22.9b)$$

$$\mathbf{E} \cdot \mathbf{n} = 0 \quad \text{on the pore walls}, \quad (22.9c)$$

$$\Phi : \text{stationary}, \quad (22.9d)$$

where \mathbf{n} is the unit outward normal from the pore region. In particular, the identity $\sum_{n=1}^{\infty} b_n \Psi_n = \mathbf{E}$ holds. The field \mathbf{E} , which solves the corresponding electrical conduction problem for a porous medium filled with a conducting fluid and having an insulating solid phase, can be interpreted as the scaled electric field, i.e., the local electric field divided by the applied macroscopic potential gradient. Decomposition (22.9a) is referred to by Avellaneda & Torquato (1991) as the so-called Hodge decomposition. We notice that there is a direct relation to the tortuosity factor α_{∞} which determines the effective electric conductivity of the porous medium. Applying the unit electric field \mathbf{e} , the microscopic current in the saturating fluid is $\mathbf{j} = \sigma_f \mathbf{E}$,

where σ_f is the fluid electric conductivity. The macroscopic current $\mathbf{J} = \phi \langle \mathbf{j} \rangle$ then obeys a macroscopic Ohm's law $\mathbf{J} = \sigma_{\text{eff}} \mathbf{e}$, with $\sigma_{\text{eff}} = \phi \sigma_f / \alpha_\infty$, and

$$\alpha_\infty = \frac{1}{\langle \mathbf{E} \rangle \cdot \mathbf{e}} = \frac{\langle \mathbf{E} \cdot \mathbf{E} \rangle}{\langle \mathbf{E} \rangle \cdot \langle \mathbf{E} \rangle}. \quad (22.10)$$

We assumed unidirectional or isotropic porous space so that the tortuosity is a scalar. Taking the mean value of (22.8), the identity

$$\sum_{n=1}^{\infty} b_n^2 = \frac{1}{\alpha_\infty} \quad (22.11)$$

immediately follows.

On the macro-level, Darcy's law describes the linear response of the macroscopic velocity $\hat{\mathbf{U}}$ to the source term $\hat{g}\mathbf{e}$:

$$\frac{\eta\phi}{k(\omega)} \hat{\mathbf{U}} = \hat{g}\mathbf{e}, \quad (22.12)$$

where $k(\omega)$ is the frequency-dependent, complex-valued dynamic permeability. This relation is the counterpart of the classical Darcy's law for steady-state flow, and reduces to it for $\omega \rightarrow 0$. In general, the dynamic permeability is a second-rank tensor which reduces to a scalar in the case of unidirectional, isotropic, or simple-cubic micro-structures. In this case, the macroscopic flow $\hat{\mathbf{U}}$ is in the same direction as the source term $\hat{g}\mathbf{e}$, which means that $\hat{\mathbf{U}} = \langle \hat{\mathbf{v}} \cdot \mathbf{e} \rangle \mathbf{e}$. From (22.12), we now easily find that

$$\frac{k(\omega)}{\phi} = \langle \tilde{\mathbf{v}} \cdot \mathbf{e} \rangle. \quad (22.13)$$

Substitution of (22.4a) yields a series expansion for $k(\omega)$:

$$\frac{k(\omega)}{\phi} = \sum_{n=1}^{\infty} \frac{b_n^2 \sigma_n}{1 + i\omega \sigma_n / \nu}. \quad (22.14)$$

Another form of (22.13) is particularly useful. For any divergence-free vector field \mathbf{w} which has zero normal components on the interface, there is identity

$$\langle \mathbf{w} \cdot \mathbf{e} \rangle = \langle \mathbf{w} \cdot \mathbf{E} \rangle, \quad (22.15)$$

which follows directly from (22.9a) after integrating by parts and using the stationary character of the fields. Thus we also have

$$\frac{k(\omega)}{\phi} = \langle \tilde{\mathbf{v}} \cdot \mathbf{E} \rangle. \quad (22.16)$$

The velocity response of the fluid to the source term $\hat{g}\mathbf{e}$ can also be defined in analogy with the response of an ideal fluid:

$$\rho\alpha(\omega)i\omega\hat{\mathbf{U}} = \hat{g}\mathbf{e}, \quad (22.17)$$

where $\alpha(\omega)$ is the frequency-dependent, complex-valued tortuosity

$$\alpha(\omega) = \frac{\nu\phi}{i\omega k(\omega)}. \quad (22.18)$$

Using (22.4a), (22.14), and (22.18), it may be verified that the following energetic representation of $\alpha(\omega)$ is valid

$$\alpha(\omega) = \frac{\langle \tilde{\mathbf{v}} \cdot \tilde{\mathbf{v}}^* \rangle}{\langle \tilde{\mathbf{v}} \rangle \cdot \langle \tilde{\mathbf{v}}^* \rangle} - \frac{\nu}{i\omega} \frac{\langle \tilde{\mathbf{v}} \cdot \nabla^2 \tilde{\mathbf{v}}^* \rangle}{\langle \tilde{\mathbf{v}} \rangle \cdot \langle \tilde{\mathbf{v}}^* \rangle}, \quad (22.19)$$

where $*$ denotes complex conjugation. The proof is given in Appendix § 29. Using homogenization theory, this result was also obtained by Smeulders *et al.* (1992). Physically speaking, this result expresses the condition that the work performed by the external force per unit time is equal to the rate of change of the kinetic energy plus the dissipated energy per unit time. The real part of (22.19) is related to the kinetic energy, and the imaginary part is related to the mean rate of energy dissipation.

In the forthcoming, we will be mainly concerned with the high frequency limit $\omega L_y^2/\nu \rightarrow \infty$ of the dynamic permeability and tortuosity. In this limit, the denominators in (22.14) may be replaced by the factors $i\omega\sigma_n/\nu$ up to high values of n , thus showing that $k(\omega) \rightarrow \nu\phi/i\omega\alpha_\infty$, according to (22.11). Indeed, assuming that the viscous term $\nabla^2\tilde{\mathbf{v}}$ is negligibly small compared to the inertial term in (22.3a), the Stokes problem (22.3) degenerates into the electric or ideal fluid problem (22.9), and $\tilde{\mathbf{v}} \rightarrow \mathbf{E}\nu/i\omega$. Substitution of this result for $\tilde{\mathbf{v}}$ in (22.13) or (22.16) again yields the above leading behavior of $k(\omega)$ at high frequencies, while substitution in (22.18) shows that the corresponding result for the dynamic tortuosity is $\alpha(\omega) \rightarrow \alpha_\infty$.

§ 23 High-frequency velocity pattern in smooth geometries

We now examine the precise limit of the Stokes problem (22.3) for $\varepsilon/L_y \rightarrow 0$, where ε is the complex viscous skin depth parameter $\varepsilon = \sqrt{\nu/i\omega} = (1-i)\delta/2$. Writing the pressure \tilde{p} in the form $\tilde{p} = \tilde{q} + \Phi$ (see (22.4b)) and substituting in (22.3a) we get

$$\tilde{\mathbf{v}} = \varepsilon^2(\mathbf{E} - \nabla\tilde{q} + \nabla^2\tilde{\mathbf{v}}). \quad (23.1)$$

Taking the curl of (23.1), we obtain the diffusion equation for the vorticity, $\nabla \times \tilde{\mathbf{v}} - \varepsilon^2 \nabla^2 \nabla \times \tilde{\mathbf{v}} = 0$. Following Johnson *et al.* (1987), we note that in the limit of high frequencies the viscous skin depth $\delta = 2|\varepsilon|$ eventually becomes much smaller than any characteristic pore size L_y . Any vorticity generated at the pore walls decays to zero as one moves away distances of the order δ from the wall into the bulk of the pore. Thus, the Laplacian $\nabla^2\tilde{\mathbf{v}} = -\nabla \times \nabla \times \tilde{\mathbf{v}}$, vanishes in the bulk fluid except for a boundary layer of thickness δ near the pore walls. It follows that outside this boundary layer, the fluid motion is that of potential flow, with

$$\tilde{\mathbf{v}} = \tilde{\mathbf{v}}_p = \varepsilon^2(\mathbf{E} - \nabla\tilde{q}). \quad (23.2)$$

It will be seen below that the presence of the pressure gradient term $-\nabla\tilde{q}$ is a small $\mathcal{O}(\varepsilon/L_y)$ correction to the leading $\mathcal{O}(1)$ flow pattern \mathbf{E} which appears because small *normal components* of the velocity are created at the virtual interface between the bulk potential flow region and the viscous boundary layer. Clearly, such normal components would not exist in straight channels for obvious symmetry reasons, and must therefore be related to the curvature of the pore walls. The *tangential* components of the velocity in the boundary layer can be directly evaluated to leading order in terms of the \mathbf{E} field only. Indeed, since δ is arbitrarily small at high enough frequencies, the walls of the pore appear to be flat in the region where the tangential velocity goes from 0 at the pore wall to the value $\varepsilon^2\mathbf{E}$ in the pore region. Thus, the tangential components of the velocity may be written to leading order (Landau & Lifschitz, 1959, p. 87)

$$\tilde{\mathbf{v}} = \varepsilon^2\mathbf{E}(\mathbf{r}_w) \left(1 - e^{-\beta/\varepsilon}\right), \quad (23.3)$$

where β is a local coordinate measured from the pore wall at position \mathbf{r}_w into the bulk of the pore: $\mathbf{r} - \mathbf{r}_w = -\beta \mathbf{n}$. Since \mathbf{E} varies at the pore scale $L_y \gg \delta$, no distinction is to be made between \mathbf{r} and \mathbf{r}_w in (23.3). Thus, we may combine (23.2) and (23.3) and consider the velocity field $\tilde{\mathbf{v}}$, including leading order tangential and normal components, as the solution of the problem

$$\tilde{\mathbf{v}} = \sigma(\mathbf{r}) (\mathbf{E} - \nabla \Pi), \quad (23.4a)$$

$$\nabla \cdot \tilde{\mathbf{v}} = 0, \quad (23.4b)$$

$$\sigma(\mathbf{r}) = \varepsilon^2 \left(1 - e^{-\beta/\varepsilon}\right), \quad (23.4c)$$

where we have introduced a stationary field Π , which is related to \tilde{q} , and defined as

$$\nabla \Pi = \left(1 - e^{-\beta/\varepsilon}\right)^{-1} \nabla \tilde{q}, \quad (23.5a)$$

in the boundary layer, and

$$\nabla \Pi = \nabla \tilde{q}, \quad (23.5b)$$

outside. The field $\tilde{\mathbf{v}}$ then solves the electrical conduction problem for a porous medium having an insulating solid phase and filled with a conducting fluid of conductivity $\sigma(\mathbf{r})$. Current conservation gives

$$-\nabla \cdot (\sigma \nabla \Pi) + \mathbf{E} \cdot \nabla \sigma = 0. \quad (23.6)$$

In the limit $\varepsilon/L_y \rightarrow 0$, only derivatives normal to the pore walls need to be considered in the boundary layer and it is convenient to introduce the stretched coordinate $\zeta = \beta/\varepsilon$ to express the fact that σ is a function of ζ only. In addition, the normal component of the unperturbed electric field E_β , which varies at scale a and is zero on the pore walls, may be replaced by its first order term $\varepsilon \zeta \left(\frac{\partial E_\beta}{\partial \beta}\right)_{\beta=0}$. Equation (23.6) is easily integrated to yield

$$\frac{\partial \Pi}{\partial \beta} = \varepsilon \left(\frac{1 - (1 + \zeta)e^{-\zeta}}{1 - e^{-\zeta}} \right) \left(\frac{\partial E_\beta}{\partial \beta} \right)_{\beta=0}. \quad (23.7)$$

We conclude that outside the boundary layer, the perturbed electric field is of the form

$$-\nabla\Pi = \varepsilon\mathbf{N}, \quad (23.8)$$

where \mathbf{N} is the unique solution of the problem

$$\mathbf{N} : \quad \text{gradient of a stationary field}, \quad (23.9a)$$

$$\nabla \cdot \mathbf{N} = 0, \quad (23.9b)$$

$$\mathbf{N} \cdot \mathbf{n} = \left(\frac{\partial E_\beta}{\partial \beta} \right)_{\beta=0} \quad \text{on the pore walls.} \quad (23.9c)$$

We note that since Π is a stationary field, the perturbed field $\varepsilon\mathbf{N}$ is orthogonal to \mathbf{E} in an averaged sense:

$$\langle \mathbf{E} \cdot \mathbf{N} \rangle = 0. \quad (23.10)$$

This can be seen from the same reasoning used to obtain (22.15): because \mathbf{E} is divergence-free and has zero normal components on the interface, we have $\langle \mathbf{E} \cdot \Pi \rangle = 0$ after integrating by parts and using the stationary character of the fields. Explicit expressions for the velocity field inside and outside the boundary layer result immediately. Inside the boundary layer we find, using (23.4a), (23.4c), and (23.7):

$$\tilde{\mathbf{v}} = \varepsilon^2(1 - e^{-\beta/\varepsilon})\mathbf{E}(\mathbf{r}_w) + \varepsilon^3 \left(1 - \left(1 + \frac{\beta}{\varepsilon} \right) e^{-\beta/\varepsilon} \right) \left(\frac{\partial E_\beta}{\partial \beta} \right)_{\beta=0} \mathbf{n}, \quad (23.11a)$$

and outside the boundary layer we have, (using (23.2), (23.5b), and (23.8)):

$$\tilde{\mathbf{v}} = \varepsilon^2 (\mathbf{E}(\mathbf{r}) + \varepsilon\mathbf{N}(\mathbf{r})). \quad (23.11b)$$

As mentioned previously, small normal components of the velocity are induced in the boundary layer, and these act as a source for the additional ideal fluid flow $\varepsilon^3\mathbf{N}$ in the bulk. Note that, though \mathbf{N} is an ideal fluid flow, it is related to the viscous nature of the fluid. This flow is orthogonal to the main flow $\varepsilon^2\mathbf{E}$, and has non vanishing mean value. This precise representation of the velocity pattern, which however does not include higher order

boundary layer tangential terms $\mathcal{O}(\varepsilon^3/L_y)$ in (23.11a) and higher order bulk terms $\mathcal{O}(\varepsilon^4/L_y^2)$ in (23.11b), is used in the next section to clarify the algebra involved in the high-frequency behavior of the dynamic permeability and tortuosity.

§ 24 High-frequency permeability and tortuosity

As suggested in the previous section by the analysis of the velocity field for materials with bounded curvature of the pore-surface interface, the high frequency development of the dynamic permeability and tortuosity may be written in successive powers of the viscous skin depth parameter:

$$\alpha(\omega) = \alpha_\infty (1 + C\varepsilon + D\varepsilon^2 + \dots), \quad (24.1a)$$

$$\frac{k(\omega)}{\phi} = \frac{\varepsilon^2}{\alpha_\infty} (1 - C\varepsilon + (C^2 - D)\varepsilon^2 + \dots). \quad (24.1b)$$

Three equivalent determinations of the C parameter will now be considered, using either (22.13), (22.16), or (22.19). The first is a new derivation which supplements in the proper manner the incomplete determination by Sheng & Zhou (1988). The second is equivalent to the original arguments by Johnson *et al.* (1987), and the third was employed by Avellaneda & Torquato (1991) though they did not capture all the details involved. The third method is the simplest one, and will also be applied in § 25 to capture some of the effects related to the presence of sharp edges in the pore wall geometry. We will show that in that case the set of equations (24.1) is modified as follows:

$$\alpha(\omega) = \alpha_\infty (1 + C\varepsilon + C_1\varepsilon^{2q} + \dots), \quad (24.2a)$$

$$\frac{k(\omega)}{\phi} = \frac{\varepsilon^2}{\alpha_\infty} (1 - C\varepsilon - C_1\varepsilon^{2q} + \dots), \quad (24.2b)$$

with the same inverse length C as before and the exponent q related to the apex angle of the edges.

To proceed now in the most direct manner, we substitute (23.11a) and (23.11b) into (22.13). Integrating the velocity field in the whole fluid volume

we have

$$\int_{V_f} \tilde{\mathbf{v}} \cdot \mathbf{e} dV = \varepsilon^2 \int_{V_f} \mathbf{E} \cdot \mathbf{e} dV - \varepsilon^2 \int_{BL} e^{-\beta/\varepsilon} \mathbf{E} \cdot \mathbf{e} dV + \varepsilon^3 \int_{IF} \mathbf{N} \cdot \mathbf{e} dV, \quad (24.3)$$

where the subscripts BL and IF denote integration over the boundary layer and the ideal fluid region, respectively. Note that we have not written the negligible contribution of the normal components of the velocity in the boundary layer. Such contribution would be associated with the constant D in (24.1a) and (24.1b) and is meaningless due to the higher order tangential terms $\mathcal{O}(\varepsilon^3/L_y)$ not written in (23.11a) and the higher order bulk terms $\mathcal{O}(\varepsilon^4/L_y^2)$ not written in (23.11b). The boundary layer contribution reduces exactly to a boundary integral $-\varepsilon^3 \int_{S_p} \mathbf{E} \cdot \mathbf{e} dS$ which is performed on the boundary walls. Moreover, extending with negligible error the volume of integration in third term of (24.3) to be that of the whole fluid, and using the orthogonality property (23.10), this third contribution is written $\varepsilon^3 \int_{V_f} \nabla \Phi \cdot \mathbf{N} dV$. Integrating by parts, this latter contribution is also written as a boundary integral on the pore walls, namely $\varepsilon^3 \int_{S_p} \Phi \mathbf{N} \cdot \mathbf{n} dS$. We thus obtain the result

$$\frac{k(\omega)}{\phi} = \frac{\varepsilon^2}{\alpha_\infty} (1 - C\varepsilon + \dots), \quad (24.4)$$

with

$$C = \frac{\alpha_\infty}{V_f} \int_{S_p} (\mathbf{E} \cdot \mathbf{e} - \Phi \frac{\partial E_\beta}{\partial \beta}) dS = \int_{S_p} (\mathbf{E} \cdot \mathbf{e} - \Phi \frac{\partial E_\beta}{\partial \beta}) dS \Big/ \int_{V_f} \mathbf{E}^2 dV. \quad (24.5)$$

This is an important result, which allows us to compare earlier results from literature. As it holds that

$$\int_{S_p} \Phi \frac{\partial \mathbf{E}_\beta}{\partial \beta} dS = \int_{S_p} \mathbf{E} \cdot \nabla \Phi dS, \quad (24.6)$$

(see Appendix § 30), we may write that

$$C = \frac{2}{\Lambda} = \frac{\int_{S_p} \mathbf{E}^2 dS}{\int_{V_f} \mathbf{E}^2 dV}. \quad (24.7)$$

where we have used (22.9a). This is the classical expression of Johnson *et al.* (1987), who were the first to define the length-scale parameter Λ as the electrically-weighted pore volume (V_f)-to-pore surface (S_p) ratio. For tube flow, Λ equals the tube radius.

Equation (24.7) can also be obtained using the following energetic arguments. From (24.1a) we derive that, to the leading order in the high frequency limit,

$$\frac{\text{Im}[\alpha(\omega)]}{\text{Re}[\alpha(\omega)]} = -C \frac{\delta}{2}. \quad (24.8)$$

On the other hand, from (22.19), we have that

$$\frac{\text{Im}[\alpha(\omega)]}{\text{Re}[\alpha(\omega)]} = \frac{\delta^2}{2} \frac{\langle \tilde{\mathbf{v}} \cdot \nabla^2 \tilde{\mathbf{v}}^* \rangle}{\langle \tilde{\mathbf{v}} \cdot \tilde{\mathbf{v}}^* \rangle}. \quad (24.9)$$

This means that we may write:

$$C = \lim_{\delta/a \rightarrow 0} \delta \frac{\langle \tilde{\mathbf{v}} \cdot \nabla^2 \tilde{\mathbf{v}}^* \rangle}{\langle \tilde{\mathbf{v}} \cdot \tilde{\mathbf{v}}^* \rangle}. \quad (24.10)$$

Substituting $\tilde{\mathbf{v}} \approx \tilde{\mathbf{v}}^* \approx \mathbf{E}$, and $\nabla^2 \tilde{\mathbf{v}}^* \approx -\mathbf{E}e^{-\beta/\varepsilon^*}$ (see (23.3)), and performing the integrals immediately yields (24.7). Note that because of the Laplacian in the numerator, there is no integration in the bulk but only a boundary layer contribution. Note also that there is no first order contribution of the perturbed potential flow $\varepsilon \mathbf{N}$ to the denominator due to the orthogonality with the unperturbed flow \mathbf{E} .

Finally, another method to obtain (24.7) is to use (22.16). From (24.1b) we have that

$$\lim_{\delta/a \rightarrow 0} \text{Re}\left[\frac{k(\omega)}{\phi}\right] = \frac{1}{\sqrt{2}} \frac{C}{\alpha_\infty} \left(\frac{\nu}{\omega}\right)^{\frac{3}{2}} = \frac{\sqrt{2}}{\Lambda \alpha_\infty} \left(\frac{\nu}{\omega}\right)^{\frac{3}{2}}. \quad (24.11)$$

Thus, from (22.16) it follows that

$$C = \lim_{\delta/a \rightarrow 0} \sqrt{2} \alpha_\infty \left(\frac{\omega}{\nu}\right)^{\frac{3}{2}} \text{Re}[\langle \tilde{\mathbf{v}} \cdot \mathbf{E} \rangle]. \quad (24.12)$$

Now, substituting the velocity pattern (23.11), there is no bulk contribution from the perturbed potential flow $\varepsilon^3 \mathbf{N}$ which is orthogonal to \mathbf{E} . There is also no bulk contribution from the unperturbed leading-order term $\varepsilon^2 \mathbf{E}$ which is purely imaginary. There is only a simple boundary layer contribution to evaluate, which again leads to (24.7).

In literature other expressions for Λ can be found. The expression obtained by Sheng & Zhou (1988) and Zhou & Sheng (1989) was as follows:

$$\frac{2}{\Lambda} = \frac{\int_{S_p} \mathbf{E} \cdot \mathbf{e} dS}{\int_{V_f} \mathbf{E}^2 dV}. \quad (24.13)$$

We notice that this is only the first term in (24.5). The origin of the incompleteness is the use of the “linear” average (22.13) without taking into account the bulk contribution from the small perturbed potential field $\varepsilon^3 \mathbf{N}$. The same expression (24.13) can be found in Pride (1994) in the context of electrokinetic effects for sound propagation in a porous medium saturated with a conductive fluid. Avellaneda & Torquato (1991) tried to clarify the discrepancy between (24.7) and (24.13) by considering higher order terms in the boundary layer calculation suggested by Sheng & Zhou (1988). However, the missing contribution is a bulk term and their boundary layer analysis was still incomplete.

The effect of the perturbed bulk contribution can elegantly be illustrated in the case of corrugated pore channels, where we will show that the use of (22.13) instead of (22.16) yields erroneous predictions for q in (24.2a) and (24.2b).

§ 25 Corrugated pore channels

We will now investigate the influence of wedge-shaped surface asperities on high-frequency permeability for 2D media. The wedge is depicted in figure 25.1. It is defined by its external angle θ_0 , or complementary apex angle $\gamma = 2\pi - \theta_0$. The potential field $\mathbf{E}(r, \theta)$ is given by Landau & Lifschitz

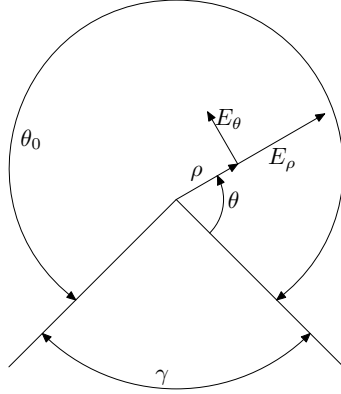


Figure 25.1: *Schematic of the wedge and potential field \mathbf{E} .*

(1959):

$$E_r = Aqr^{q-1} \cos q\theta \quad (25.1)$$

$$E_\theta = -Aqr^{q-1} \sin q\theta, \quad (25.2)$$

where A is a constant and $q = \pi/\theta_0$. Introducing the dimensionless stretched boundary layer variable $\varrho = r/\varepsilon$, we find that

$$E_r = Aq\varepsilon^{q-1}\varrho^{q-1} \cos q\theta = \mathcal{O}(\varepsilon^{q-1}), \quad (25.3)$$

$$E_\theta = -Aq\varepsilon^{q-1}\varrho^{q-1} \sin q\theta = \mathcal{O}(\varepsilon^{q-1}). \quad (25.4)$$

To evaluate the high-frequency limit of the permeability, we will consider the limit of the real part of (22.16):

$$\lim_{\varepsilon/a \rightarrow 0} \frac{\text{Re}[k(\omega)]}{\phi} = \lim_{\varepsilon/a \rightarrow 0} \text{Re}\langle [\tilde{\mathbf{v}} \cdot \mathbf{E}] \rangle. \quad (25.5)$$

The integral may be split in the bulk fluid contribution from the potential flow region and the boundary layer contribution. The general argument leading to the decomposition (23.2) in the bulk fluid was not concerned

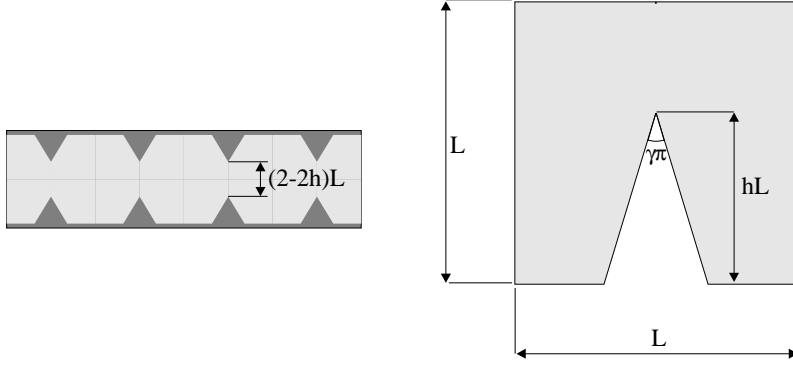


Figure 25.2: *Geometry of two-dimensional channel with intrusive wedges (top). Geometry of the periodic cell (bottom).*

with any detailed calculation of what actually happens in the boundary layer. Similarly, the orthogonality property $-\langle \mathbf{E} \cdot \nabla \tilde{q} \rangle = 0$ between the “ground state” field \mathbf{E} and the perturbed field $-\nabla \tilde{q}$ is essentially due to the stationary character of the pressure field \tilde{q} and is not concerned with the specific distribution of this field. This is why there is, as before, no contribution to (25.5) from the potential flow region. We only have to evaluate the boundary layer contribution. The boundary layer may be divided in two different parts. “Far” from the tip of the wedges, the boundary layer will have the usual flat-surface profile. “Near” the tip of the wedges, the boundary layer profile will be significantly different from the flat-surface profile. The pertinent length scale giving these notions of “far” and “near” is obviously the diffusion length of the vorticity, i.e., the viscous skin depth $\delta = \sqrt{2\nu/\omega}$. Let L be the separation between the tips of the wedges along the pore surface (see figure 25.2). Clearly, as δ/L goes to zero, the region of extent δ along the pore surface where the boundary layer

is of the non-plane “near”-type is small compared to the region of extent L where the boundary layer has the usual flat-surface profile. As will be verified below, the leading correction $-C\varepsilon$ in the developments (24.1) is not affected. Here we assumed that the apex angle γ is strictly larger than zero, so that the Johnson *et al.* (1987) Λ parameter remains defined. The contributions of the wedges to (25.5) due to the non-plane “near”-type boundary layers is now shown to produce correction terms between the second and the third term in (24.1) as indicated in (24.2).

We consider Stokes equation (23.1)

$$\tilde{\mathbf{v}} - \varepsilon^2 \nabla^2 \tilde{\mathbf{v}} = \varepsilon^2 (\mathbf{E} - \nabla \tilde{q}) \quad (25.6)$$

in the “near”-region around the tip. In the flat-surface case, the gradient $-\nabla \tilde{q}$ was a small correction with an extra factor ε compared to \mathbf{E} . This may not be the case now. The pressure gradient term $-\nabla \tilde{q}$ describes the modification to the inertial reaction force between solid and fluid which is due to the viscous effects. Its averaged value $\langle -\nabla \tilde{q} \rangle$ will be smaller, in magnitude, than the external unit force \mathbf{e} . Thus, using the estimate (25.3)-(25.4) we may conclude that, to the leading order, $\tilde{\mathbf{v}} = \mathcal{O}(\varepsilon^{q+1})$. Now performing the integral in (25.5) around the tip of the wedge, we find that

$$\begin{aligned} \text{Re} \left[\int_0^\beta \int_0^{\theta_0} \tilde{\mathbf{v}} \cdot \mathbf{E} dV \right] &= \text{Re} \left[\varepsilon^2 \int_0^{\beta/\varepsilon} \int_0^{\theta_0} \tilde{\mathbf{v}} \cdot \mathbf{E} \rho d\theta d\rho \right] = \\ &= \text{Re} [\varepsilon^2 \mathcal{O}(\varepsilon^{2q})] = \text{Re} [\mathcal{O}(\varepsilon^{2q+2})], \end{aligned} \quad (25.7)$$

thus showing the form expressed in (24.2a) and (24.2b). This means that for high-frequencies, using the definition of ε , from (25.5) and (25.7) it can be written that

$$\lim_{\varepsilon/a \rightarrow 0} \text{Re} \left[\frac{k(\omega)}{\phi} \right] = \text{Re} [\mathcal{O}(\omega^{-(q+1)})] = \text{Re} [\mathcal{O}(\omega^{n-\frac{3}{2}})], \quad (25.8)$$

where $n = \frac{1}{2} - q$. The reason for the introduction of n will become apparent in § 27.

In a paper by Achdou & Avellaneda (1992) an analogous reasoning was followed for the problem of corrugated pore channels. However, they did

not multiply the velocity field $\tilde{\mathbf{v}}$ by the electric field \mathbf{E} in (25.7), thus obtaining an $\mathcal{O}(\varepsilon^{q+3})$ dependence (see Achdou & Avellaneda (1992, eq. E7)). However, when the linear average (22.13) is employed it is not possible to evaluate the high frequency limit of the permeability by only considering what happens in the boundary layer. There is a missing contribution from the perturbed potential flow in the bulk. The significant difference between (25.7) and the Achdou & Avellaneda (1992) result shows that in the case of wedges the bulk contribution dominates the boundary layer contribution, whereas in the bounded curvature case both contributions were of the same order. The behavior of the real part of the dynamic permeability will now be investigated analytically for non-corrugated channels where (24.11) should apply and numerically for corrugated channels where (25.7) should apply.

§ 26 Non-corrugated channels

As porous media models, Biot (1956*b*) discussed an ensemble of identical slits within a 2D-solid and an ensemble of identical cylindrical tubes within a 3D-solid. The slit opening is $2R$, and the tube radius is R . The number density of slits and tubes is represented by the porosity ϕ . When the fluid flow is oriented along the cylinder axis of the tube model, it was already shown by Zwikker & Kosten (1949) that:

$$\frac{k(\omega)}{k_0} = \tilde{k}(\omega) = \frac{8}{i \text{Wo}^2} \left(1 - \frac{2J_1(i^{3/2} \text{Wo})}{i^{3/2} \text{Wo} J_0(i^{3/2} \text{Wo})} \right), \quad (26.1)$$

where $\text{Wo} = R\sqrt{\omega/\nu}$ is the so-called Womersley number, and J_0 and J_1 are Bessel functions of the zeroth and first order. From the relation for Poiseuille flow, we find that $k_0 = \frac{1}{8}\phi R^2$. This means that the characteristic frequency $\omega_c = \nu\phi/k_0\alpha_\infty$, where transition from viscous to inertial behavior is expected is equal to $8\nu/R^2$ in this case, and $\text{Wo} = \sqrt{8\omega/\omega_c}$. For high frequencies, it can be shown that (Biot, 1956*b*):

$$\lim_{\omega \rightarrow \infty} \tilde{k} = \frac{1}{i\tilde{\omega}} \left(1 - \frac{1-i}{2\sqrt{\tilde{\omega}}} \right), \quad (26.2)$$

where we have introduced $\tilde{\omega} = \omega/\omega_c$. This expression is in agreement with (24.11). This is most conveniently shown by writing (24.11) as $\lim_{\omega \rightarrow \infty} \tilde{k} = \frac{1}{2} \sqrt{M} \tilde{\omega}^{-3/2}$, where M is the so-called shape-factor:

$$M = 8k_0\alpha_\infty/\phi\Lambda^2, \quad (26.3)$$

which is identical to 1 in this case. Similarly, when the flow is oriented along the slit layers, it can be shown that (Biot, 1956*b*):

$$\tilde{k}(\omega) = \frac{k(\omega)}{k_0} = \frac{3}{i \text{Wo}^2} \left(1 - \frac{\tanh(i^{1/2} \text{Wo})}{i^{1/2} \text{Wo}} \right). \quad (26.4)$$

Here we find that $k_0 = \frac{1}{3}\phi R^2$, so that for this configuration $\omega_c = 3\nu/R^2$, and $\text{Wo} = \sqrt{3\omega/\omega_c}$. The high-frequency limit is now given by:

$$\lim_{\omega \rightarrow \infty} \tilde{k} = \frac{1}{i\tilde{\omega}} \left(1 - \frac{1-i}{\sqrt{6\tilde{\omega}}} \right). \quad (26.5)$$

Also this expression is in agreement with (24.11), because for slit flow $M = 2/3$.

The real and imaginary parts of the dynamic permeability for both the tube model and the slit model are plotted in figure 26.1. We notice that there are only minor differences between both models. For low frequencies, the real part of the dynamic permeability approaches the stationary Darcy permeability, whereas the imaginary part tends to zero. For high frequencies, the imaginary part of the dynamic permeability shows a $-1/\tilde{\omega}$ dependency for both tube and slit model, whereas for the real part the $\tilde{\omega}^{-3/2}$ behavior can be discerned. We also notice that the rollover from low-frequency viscous behavior to high-frequency inertia behavior is observed at $\omega \approx \omega_c$ indeed.

§ 27 Numerical computations

Numerical computations were performed on the periodic polygon $P_1 \dots P_7$, depicted in figure 25.2. The cell $P_1 P_5 P_6 P_7$ is a square with sides L_w . The

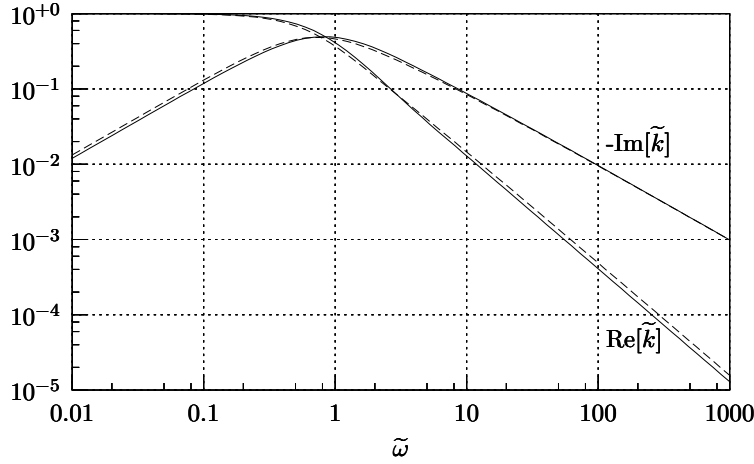


Figure 26.1: *Dynamic permeability for tube flow (dashed line) and slit flow (solid line)*

apex angle of the wedge is γ , and its height is hL_w , thus leaving a channel opening $(2 - 2h)L_w$ (see figure 25.2). Numerical results are presented for varying γ where h is set 0.5, and for varying h , where $\tan \gamma/2$ is set 0.5. Taking the pressure gradient in the horizontal direction, the Stokes problem (22.3a), (22.3b) was solved using a Finite-Element code based on a Uzawa decomposition method. A Dirichlet-type boundary condition was prescribed at the pore walls: $\tilde{\mathbf{v}} = 0$. The solution to the Stokes problem is approximated by means of N_1 finite elements and by using the variational formulation of the problem. To ensure accuracy, we have used an iterative automatic method, i.e., the solution is computed on the N_1 mesh, next an a-posteriori estimate of the error is computed, and finally the mesh is locally refined accordingly by means of a Delaunay technique developed by Rebay (1993). Successful use of this refinement method on sharp-edged wedges was reported by Firdaouss *et al.* (1998). Once the flow field is known, the dynamic permeability is computed using (22.13).

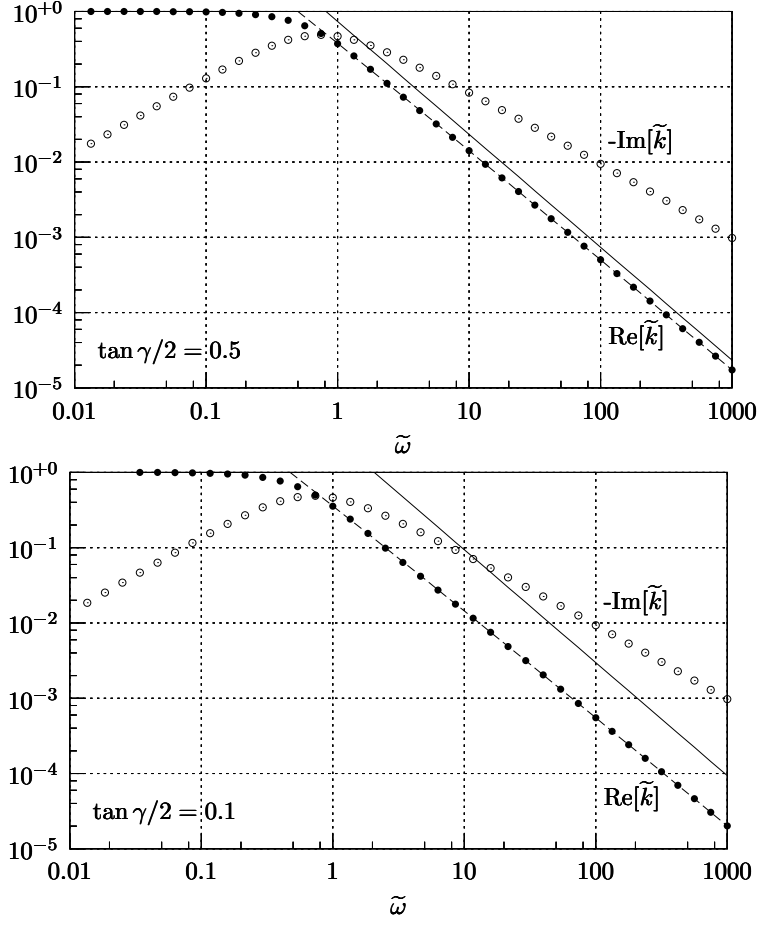


Figure 27.1: *Dynamic permeability for $\tan \gamma/2 = 0.5$ (top), and $\tan \gamma/2 = 0.1$ (bottom). In both figures $h = 0.5$. The circles and dots represent the numerical results. Both classical (drawn lines) and improved (dashed lines) high-frequency approximations for $\text{Re}[\tilde{k}]$ are plotted.*

Two typical results are shown in figures 27.1, where the real and imaginary parts of the dynamic permeability are plotted for $\tan \gamma/2 = 0.5$ and for $\tan \gamma/2 = 0.1$. In both cases, $h = 0.5$. The high-frequency approximation $\frac{1}{2}\sqrt{M}\tilde{\omega}^{-3/2}$ is drawn as straight lines in both plots. An improved high-frequency approximation is also drawn (dashed line), which will be discussed in the forthcoming. The parameters M and ω_c were computed independently (Cortis & Smeulders, 2001). We notice that in both cases the $-1/\tilde{\omega}$ -dependency for the imaginary part of the dynamic permeability is preserved for high frequencies. For the real part of the dynamic permeability, however, significant departures from the predicted $\frac{1}{2}\sqrt{M}\tilde{\omega}^{-3/2}$ behavior are found. Apparently, these discrepancies become more significant for smaller apex angle, i.e., for sharper edges (see figures 27.1). These findings are in agreement with those of Achdou & Avellaneda (1992) who reported that the presence of a wedge in the flow channel induces a non-analytic dependence on the viscous skin depth $\delta = \sqrt{2\nu/\omega}$, and a slower convergence of $\tilde{k}(\omega)$ to its asymptotic limit than predicted by (24.11). They subsequently argue that the high-frequency behavior should be described as the combination of the asymptotic expansion (24.11) for laminar boundary layers and the contribution of the singularity as described in § 24:

$$\lim_{\omega \rightarrow \infty} \operatorname{Re}[\tilde{k}(\omega)] = \frac{1}{2}\sqrt{M} \tilde{\omega}^{-\frac{3}{2}} (1 + C_1 \tilde{\omega}^n), \quad (27.1)$$

or alternatively

$$\lim_{\omega \rightarrow \infty} \tilde{\omega}^{\frac{3}{2}} \operatorname{Re}[\tilde{k}(\omega)] = \frac{1}{2}\sqrt{M} + \frac{1}{2}C_1 \tilde{\omega}^n \sqrt{M}, \quad (27.2)$$

where C_1 is a numerical constant and the exponent n is related to the wedge angle γ . In § 24 it is derived that $n = \frac{1}{2} - q = -\frac{1}{2}\gamma/(2\pi - \gamma)$ whereas Achdou & Avellaneda (1992) arrived at $n = -\frac{1}{2}q = -\frac{1}{2}\pi/(2\pi - \gamma)$. We notice that for $C_1 = 0$, we find back the asymptotic behavior (24.11). Our precise numerical computations now offer the possibility of determining the values of n and also M independently. In figure 27.2, we plotted the derivative $\partial[\tilde{\omega}^{3/2}\operatorname{Re}\tilde{k}(\omega)]/\partial\tilde{\omega}$ against $\tilde{\omega}$ on a double logarithmic scale for various apex angles γ . This derivative was computed by means of a three point centered

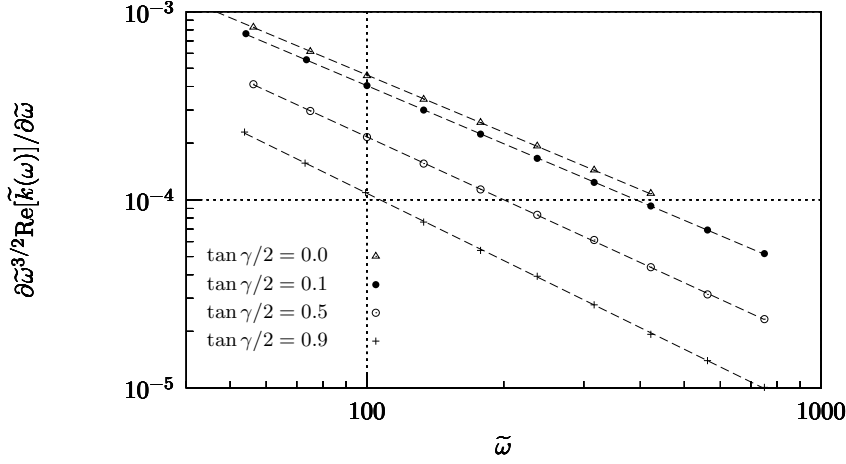


Figure 27.2: Regression lines to determine the n parameter for $h=0.5$. We notice that the computed values fit very well the regression lines.

finite difference method. We notice that for high frequencies, these curves become straight lines, which is in agreement with (27.2). Linear regression now yields the slope of the curve $(n - 1)$, and the value $\frac{1}{2}C_1n\sqrt{M}$. Consequently, the value of $\frac{1}{2}C_1\sqrt{M}$ is also known. Finally, M is obtained from linear regression of $\tilde{\omega}^{\frac{3}{2}}\text{Re}[\tilde{k}(\omega)]$ versus $\tilde{\omega}^n$.

The results are given in table 27.1, and figures 27.3 and 27.4. We notice that the present theory is only slightly overestimating the numerical results. The Achdou & Avellaneda (1992) predictions give a considerable underestimation of the computations. In the limiting case of knife-edge singularities ($\gamma = 0$), there is a good agreement between the computations and the present theory. We also notice that the M values are in good agreement with the classical value (Johnson *et al.*, 1987) $M = 8Fk_0/\Lambda^2$. This suggests that this definition for M is also correct in the case of surface roughness, and that the contribution of the singularities can indeed be captured in a non-analytic extension of the existing theory without affecting

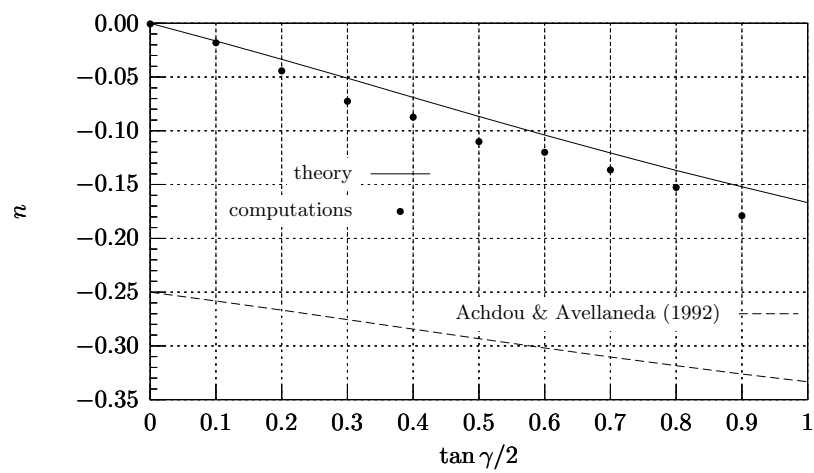


Figure 27.3: *Computed and theoretical n values for $h = 0.5$.*

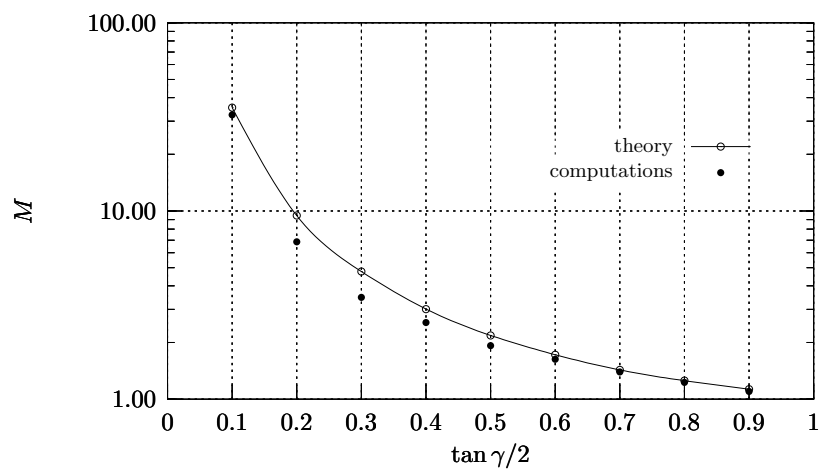


Figure 27.4: *Computed and theoretical M values for $h = 0.5$.*

$\tan \gamma/2$	n			M	
	present work		A&A	present work	JKD
	computations	theory	theory	computations	theory
0.0	-0.006	-0.0000	-0.2500	992.74	∞
0.1	-0.018	-0.0164	-0.2582	32.42	35.4123
0.2	-0.044	-0.0335	-0.2668	6.86	9.4607
0.3	-0.073	-0.0511	-0.2756	3.47	4.7652
0.4	-0.087	-0.0689	-0.2845	2.55	3.0124
0.5	-0.110	-0.0866	-0.2933	1.92	2.1820
0.6	-0.120	-0.1039	-0.3019	1.62	1.7223
0.7	-0.137	-0.1207	-0.3103	1.39	1.4299
0.8	-0.153	-0.1368	-0.3184	1.22	1.2543
0.9	-0.179	-0.1521	-0.3261	1.09	1.1305

Table 27.1: Values of the n -parameter obtained from linear regression applied to our numerical computations are compared with present work ($n = 1/2 - q$) and Achdou & Avellaneda (1992) (A&A) predictions ($n = -q/2$). Values of the M -parameter obtained from linear regression are compared with the Johnson et al. (1987) (JKD) theory. $h = 0.5$.

the parameters of such theory. We notice that when $\gamma = 0$, our computations yield a large though finite value for M , while the value obtained from the theory is infinite. The obtained results for n and M are substituted in the high-frequency correction (27.1), which is plotted in figures 27.1. As expected, we find excellent agreement.

The effect of the channel opening was checked by varying the intrusion height h , while keeping $\tan \gamma/2 = 0.5$. Obviously this should not affect the value for n , which only depends on the apex angle γ . It can be predicted that $n = -0.0866$, whereas Achdou & Avellaneda (1992) arrive at $n = -0.2933$. Our computations are summarized in table 27.2. We notice that for very small intrusion heights, the computations start to deviate from the theory, because the effect of the flat wall is predominant over the effect of the singularity. On the other hand, for very small openings, the results also deviate from theory since the presence of the opposite wedge disturbs the

h	n
	computations
0.1	-0.215
0.2	-0.174
0.3	-0.108
0.4	-0.117
0.5	-0.110
0.6	-0.121
0.7	-0.134

Table 27.2: Computed n -values for $\tan \gamma/2 = 0.5$. The predicted value is -0.0866 . The Achdou & Avellaneda (1992) prediction is -0.2933 .

flow field with respect to the assumptions made in § 24. We notice that good results are obtained for $h = 0.5$, which is the value we used for the computations in table 27.1.

§ 28 Conclusions

We analyzed in detail the high-frequency fluid velocity patterns in the bulk fluid and the boundary layer for smooth and corrugated geometries. The classical Johnson *et al.* (1987) high-frequency limit for smooth geometries was obtained in different manners, thus clarifying the discrepancy with the Sheng & Zhou (1988) treatment and the Avellaneda & Torquato (1991) approach. The discrepancies were illustrated for corrugated pore channels, where the bulk contribution dominates the contribution from the boundary layer, which causes a slower convergence of $k(\omega)$ to its asymptotic limit than predicted from the classical theory by Johnson *et al.* (1987). This behavior is captured in a non-analytic extension of the classical expressions as was proposed by Achdou & Avellaneda (1992). This extension represents the contribution of the wedge-shaped singularity. We investigated the dependency of the extension term on the wedge angle of the intrusion in the corrugated channels. For various angles, we numerically computed the dynamic permeability by means of a precise Finite Element

solver for the Stokes' flow. The effect of varying channel opening was investigated separately. The dependency of the extension term on the wedge angle was validated by our numerical results, whereas the Achdou & Avelaneda (1992) predictions underestimated them. Moreover, we found that the contribution of the singularities does not affect the original parameters of Johnson *et al.* (1987) theory.

APPENDICES TO CHAPTER IV

§ 29 Energetic representation of the dynamic tortuosity

Here we derive the relation (22.19) using the eigenmode formalism. First define the notation

$$\tilde{\sigma}_n = \frac{\sigma_n}{1 + i\omega\sigma_n/\nu} \quad (29.1)$$

and the mean symbol

$$\|X_n\| = \sum_{n=1}^{\infty} b_n^2 X_n. \quad (29.2)$$

Then (22.14) and (22.18) read

$$\frac{k(\omega)}{\phi} = \|\tilde{\sigma}_n\|, \quad (29.3)$$

and

$$\alpha(\omega) = \frac{\nu}{i\omega\|\tilde{\sigma}_n\|}. \quad (29.4)$$

From (29.4) we write

$$\alpha(\omega) = \frac{\nu}{i\omega} \frac{\|\tilde{\sigma}_n^*\|}{\|\tilde{\sigma}_n\| \|\tilde{\sigma}_n^*\|}, \quad (29.5)$$

where $*$ denotes complex conjugation. Combining (29.5) with the identity

$$\|\tilde{\sigma}_n^*\| = \frac{i\omega}{\nu} \|\tilde{\sigma}_n \tilde{\sigma}_n^*\| + \|\tilde{\sigma}_n \tilde{\sigma}_n^* \sigma_n^{-1}\| \quad (29.6)$$

we get

$$\alpha(\omega) = \frac{\|\tilde{\sigma}_n \tilde{\sigma}_n^*\|}{\|\tilde{\sigma}_n\| \|\tilde{\sigma}_n^*\|} + \frac{\nu}{i\omega} \frac{\|\tilde{\sigma}_n \tilde{\sigma}_n^* \sigma_n^{-1}\|}{\|\tilde{\sigma}_n\| \|\tilde{\sigma}_n^*\|}, \quad (29.7)$$

where the form of (22.19) may be recognized. Using (22.4a), it is easy to verify that

$$\langle \tilde{\mathbf{v}} \rangle \cdot \mathbf{e} = \|\tilde{\sigma}_n\| \quad (29.8)$$

and

$$\langle \tilde{\mathbf{v}} \cdot \tilde{\mathbf{v}}^* \rangle = \|\tilde{\sigma}_n \tilde{\sigma}_n^*\|. \quad (29.9)$$

Using (22.5a) we finally verify that

$$-\langle \tilde{\mathbf{v}} \cdot \nabla^2 \tilde{\mathbf{v}}^* \rangle = \|\tilde{\sigma}_n \tilde{\sigma}_n \sigma_n^{-1}\|. \quad (29.10)$$

§ 30 Proof of the identity (40)

We want to prove the identity

$$\int_{S_p} \mathbf{E} \cdot \nabla \Phi \, dS = \int_{S_p} \Phi \frac{\partial \mathbf{E}_\beta}{\partial \beta} \, dS. \quad (30.1)$$

Let us denote with ξ^i and ξ_i contravariant and covariant quantities respectively. The metric is such that $g_{\mu\nu} d\xi^\mu d\xi^\nu = ds^2$. Let the indices μ and ν run over 1,2,3, and the indices i and j run over 1,2.

$$\begin{aligned} \int_{S_p} \mathbf{E} \cdot \nabla \Phi \, dS &= \int_{S_p} (e^\mu - g^{\mu\nu} \Phi_{,\nu}) \Phi_{,\mu} \, dS = \\ &= \int_{S_p} [(e^\mu - g^{\mu\nu} \Phi_{,\nu}) \Phi]_{,\mu} \, dS - \int_{S_p} \Phi (e^\mu - g^{\mu\nu} \Phi_{,\nu})_{,\mu} \, dS. \end{aligned} \quad (30.2)$$

The second integral on the RHS immediately vanishes: $e^\mu_{,\mu}$ is the divergence $\nabla \cdot \mathbf{e} = 0$, and $(g^{\mu\nu} \Phi_{,\nu})_{,\mu} = \Phi^{\prime\prime\mu}_{,\mu}$ is the Laplacian $\nabla^2 \Phi = 0$. The first integral is

$$\begin{aligned} \int_{S_p} [(e^\mu - g^{\mu\nu} \Phi_{,\nu}) \Phi]_{,\mu} \, dS &= \\ &= \int_{S_p} [(e^i - g^{ij} \Phi_{,j}) \Phi]_{,i} \, dS + \int_{S_p} [(e^3 - g^{33} \Phi_{,3}) \Phi]_{,3} \, dS. \end{aligned} \quad (30.3)$$

The first term in the RHS vanishes because of the stationarity character of the fields. In the second term there is no difference between the covariant and the contravariant position. We get

$$\int_{S_p} (e^3 \Phi_{,3} - \Phi_{,3} \Phi_{,3} - \Phi \Phi_{,3,3}) dS = \int_{S_p} -\Phi \Phi_{,3,3} dS. \quad (30.4)$$

Making the identification $_{,3} = \partial_\beta$ we obtain the desired result.

CHAPTER V

NUMERICAL VALIDATION OF SCALING FUNCTIONS FOR VISCOUS AND THERMAL RELAXATION IN GAS-FILLED POROUS MEDIA

In this Chapter, we investigate two general analytical scaling functions describing the viscous and thermal dynamic behavior. In § 31 we introduce the Johnson *et al.* (1987) and Pride *et al.* (1993) viscous models, and the Champoux & Allard (1991) and Lafarge *et al.* (1997) thermal models. In § 32 the macroscopic parameters governing these viscous and thermal scaling functions are computed for regular ensembles of cylindrical and squared fibers at different porosities. Analytical solutions valid for the cylindrical fibers at high porosities are compared to the numerical data. In § 33, we present Finite Element numerical computations of the viscous and thermal frequency-dependent tortuosity for these arrangements of cylindrical and squared fibers, and we compare them to the scaling functions predictions. In § 34, the causality condition for the Pride scaling function is investigated. Finally, in Appendix § 36, a new scaling function is proposed.

§ 31 Scaling functions

In this section we introduce a general analytical scaling functions for both the viscous and thermal effects. It was noted by Johnson *et al.* (1987) that

$$\frac{k(\omega)}{k_0} = [F(\omega) + i\tilde{\omega}]^{-1}, \quad (31.1)$$

where

$$F(\omega) = \sqrt{1 + \frac{M}{2}i\tilde{\omega}}. \quad (31.2)$$

This function satisfies both the high-frequency behavior discussed in Chapter IV and the low-frequency behavior

$$\lim_{\omega \rightarrow 0} k(\omega) = k_0. \quad (31.3)$$

Based on arguments of similarity, Champoux & Allard (1991) defined a thermal scaling function

$$F'(\omega) = \sqrt{1 + \frac{M'}{2}i\tilde{\omega}'}, \quad (31.4)$$

where $\tilde{\omega}' = \omega/\omega'_c$, and $M' = 8k'_0/\phi\Lambda'^2$. It was noted by Pride *et al.* (1993) that for some numerical and experimental data large discrepancies occurred between the data and the scaling functions for the imaginary part of $k(\omega)$ at low frequencies. It was argued that the reason for these discrepancies is that the scaling function (31.2) does not require the imaginary part of $k(\omega)$ to satisfy the exact frequency dependency in the limit $\omega \ll \omega_c$. They therefore introduced a modified scaling function

$$F(\omega) = 1 - m + m\sqrt{1 + \frac{1}{2}\frac{M}{m^2}i\tilde{\omega}}, \quad (31.5)$$

where m is a correction factor for low frequencies. We notice that for $m = 1$, both scaling functions (31.2) and (31.5) are equal. In this Chapter, we will compare (31.2) and (31.5) with numerically obtained dynamic permeability values for a variety of two-dimensional configurations, whereas Pride *et al.* (1993) only gave analytical solutions of sinusoidally varying tubes.

Another important aspect of porous media acoustics is the heat exchange between the fluid and the solid constituents. Similar to the viscous case, where the dissipation of energy is governed by the viscous relaxation time L_y^2/ν , the thermal dissipation is governed by the thermal relaxation time L_y^2/a_f , where a_f is the thermal diffusivity of the fluid. For

water, $a_f = 144 \times 10^{-5} \text{ m}^2/\text{s}$, which means that thermodynamic effects can be ignored for usual acoustic materials with $L_y \approx 10^{-4} \text{ m}$. For air, $a_f = 1.87 \times 10^{-5} \text{ m}^2/\text{s}$ however, which means that significant deviations from isothermal conditions may occur in the higher frequency range. This is a well-known phenomenon in damping phenomena of pulsating gas bubbles in liquids (Devin, 1959), where the heat conduction between the gas and the liquid is taken into account by introducing a frequency-dependent gas bulk modulus $K_f(\omega) = n(\omega)K_{f0}$, meaning that the isothermal gas bulk modulus K_{f0} is modified by the polytropic coefficient $n(\omega)$. To account for the thermal dissipation in gas-filled porous media, it seems reasonable to replace the gas bubble radius by the pore volume-to-surface ratio $2V_p/S$ as the characteristic length scale. This ratio is sometimes referred to as the Kozeny radius Λ' . It generalizes the notion of hydraulic radius for arbitrary geometries, and reduces to it for cylindrical pores. Champoux & Allard (1991) used the concept of dynamic permeability to obtain a general phenomenological frequency dependence for the dynamic bulk modulus $K_f(\omega)$. In later years, the analogy between viscous and thermal dissipation was implemented further by Lafarge *et al.* (1997) who defined a thermal permeability $k'(\omega)$ and a thermal tortuosity $\alpha'(\omega)$:

$$\frac{\lambda\phi}{k'(\omega)}\langle\hat{T}\rangle = i\omega\langle\hat{p}\rangle, \quad (31.6)$$

$$i\omega\alpha'(\omega)\rho_f c_p\langle\hat{T}\rangle = i\omega\langle\hat{p}\rangle, \quad (31.7)$$

where $\langle\hat{T}\rangle$ is the macroscopic excess temperature, and λ and c_p are the thermal conductivity and the specific heat at constant pressure, respectively. This implies that thermal scaling functions analogous to (31.2) and (31.5) can be introduced to describe the transition from low-frequency isothermal to high-frequency isoentropic behavior.

These viscous and thermal scaling functions will be compared with numerical results for regular ensembles of cylindrical and squared fibers.

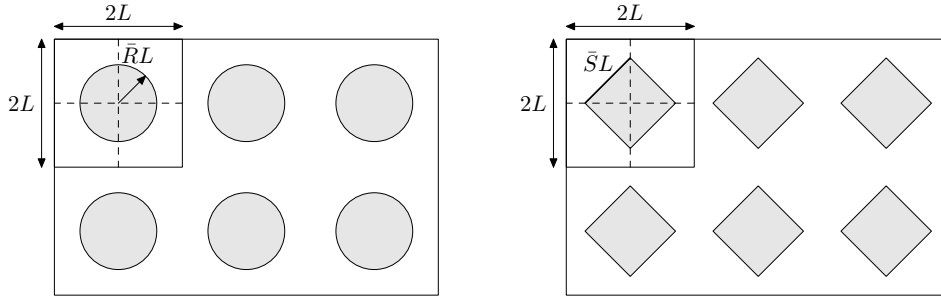


Figure 32.1: *Configurations studied: (A) 2D arrangement of solid cylinders surrounded by fluid; (B) 2D arrangement of solid squares surrounded by fluid.*

§ 32 Viscous and thermal coefficients

Numerical computations of viscous and thermal dynamic permeability were performed for two types of porous media presented in figures 32.1. They consist of regular ensembles of cylindrical (figure 32.1A) and squared (figure 32.1B) fibers, having center points $2L$ apart. These materials are subjected to a stationary flow field perpendicular to the fibers. The problem is thus two-dimensional. The radius of the cylinder, R , varied between $0.113L$ and $0.944L$, so that the corresponding porosity $\phi = 1 - \pi(R/L)^2/4$ varied between 0.99 and 0.3. The side of the square, S , varied between $0.2L$ and $\sqrt{1.8}L$, so that the porosity $\phi = 1 - (S/L)^2/4$ varied between 0.99 and 0.55 in this case.

For the regular arrangement of cylinders depicted in figure 32.1A, it is possible to write analytical solutions, valid in the limit of high porosities, for both the viscous and the thermal problems. In fact, at high-porosities, it should not be a problem to replace the square boundary of the unit cell by a circle as we expect that the flow field has practically no variation far away from the obstacle (Kuwabara, 1959). We choose the radius of this circle equal to $R/\sqrt{1-\phi}$ such that the porosity remains unchanged. The

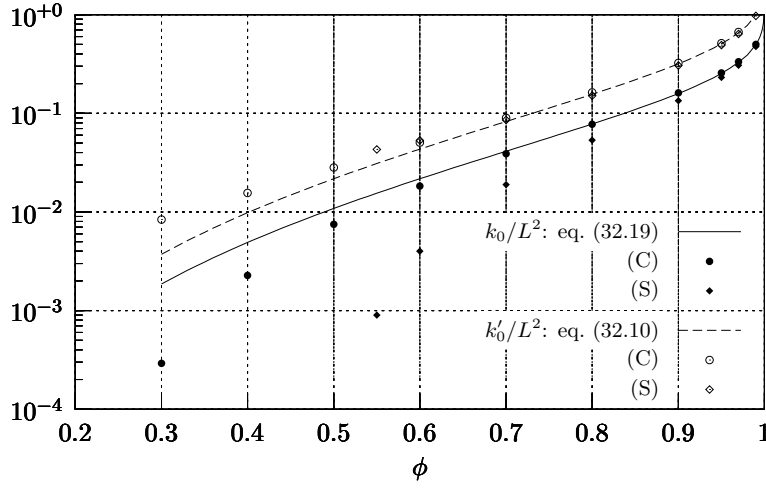


Figure 32.2: *Plot of the static viscous and thermal permeabilities k_0 and k'_0 for the cylinders (C) and the squares (S) compared with the analytical solution for a dilute cylinder configuration (lines).*

vorticity and the normal component of the velocity can thus be assumed to be zero at a radial distance $R/\sqrt{1-\phi}$ from the center. Let us assume a system of cylindrical coordinates (r, θ) normalized with respect to R .

For the potential problem, the velocity field \mathbf{v}_∞ can be expressed as

$$\mathbf{v}_\infty(r, \theta) = -\nabla\psi(r, \theta), \quad (32.1)$$

where the potential ψ satisfies

$$\nabla^2\psi(r, \theta) = 0, \quad (32.2)$$

with the impermeability condition on the boundary wall

$$\frac{\partial\psi}{\partial r} = 0 \quad \text{for } r = 1, \quad (32.3a)$$

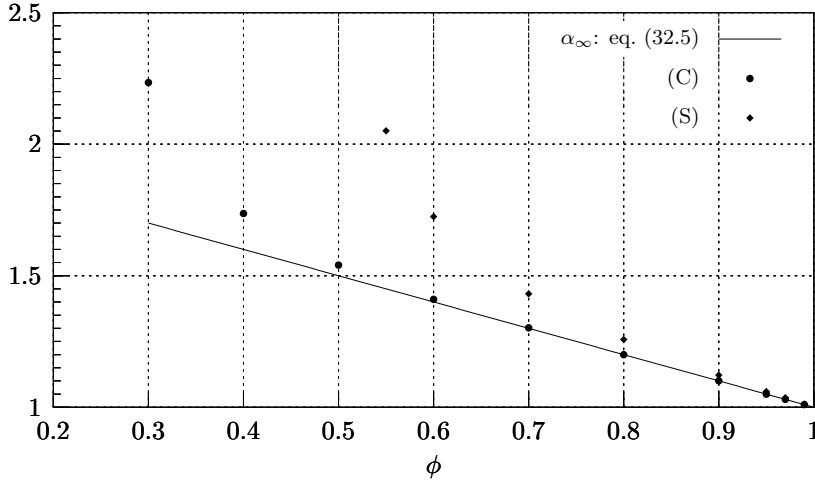


Figure 32.3: Plot of the viscous tortuosity α_∞ for the cylinders (C) and the squares (S) are compared with the analytical solution for a dilute cylinder configuration (lines).

and the condition on the average velocity, $\langle \mathbf{v}_\infty \rangle = 1$,

$$\frac{1}{c-1} \int_1^c \frac{\partial \psi}{\partial \theta} = -1, \quad (32.3b)$$

where $c = 1/\sqrt{1-\phi}$ is the normalized distance of the boundary from the center of the fiber. The solution of (32.2) and (32.3) reads:

$$\psi(r, \theta) = -\frac{c}{c+1} \left(r + \frac{1}{r} \right) \cos \theta. \quad (32.4)$$

Substituting (32.4) in (22.10) and (24.13) yields the following expressions for the tortuosity α_∞

$$\alpha_\infty = \frac{c^2 + 1}{c^2}, \quad (32.5)$$

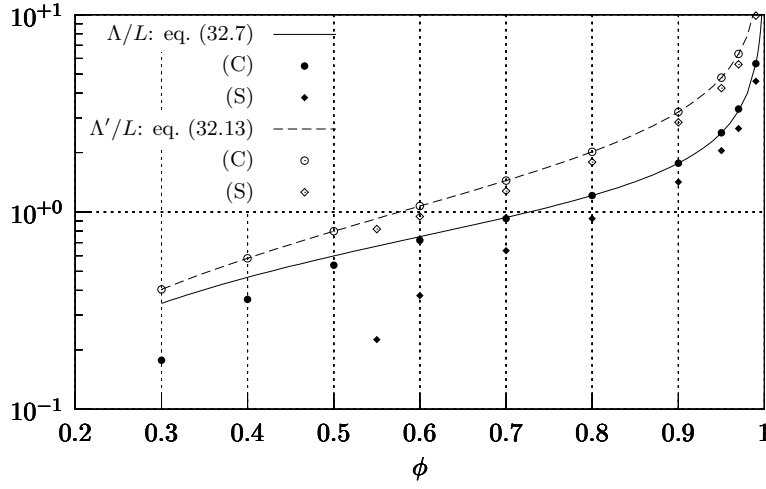


Figure 32.4: *Plot of the characteristic viscous and thermal lengths Λ and Λ' for the cylinders (C) and the squares (S) compared with the analytical solution for a dilute cylinder configuration (lines).*

and the characteristic viscous length Λ

$$\frac{\Lambda}{R} = \frac{(c^2 - 1)(c^2 + 1)}{2c^2}, \quad (32.6)$$

which normalized with respect to L reads

$$\frac{\Lambda}{L} = \frac{1}{\sqrt{\pi}} \frac{(c^2 - 1)(c^2 + 1)}{c^3}. \quad (32.7)$$

For the thermal problem, the temperature field $T(r)$, solution of $\nabla^2 T = -1$, with the boundary conditions $T(1) = 0$, and $\partial T(c)/\partial r = 0$, can be written

$$T(r) = \frac{1 - r^2}{4} + \frac{c^2}{2} \ln r. \quad (32.8)$$

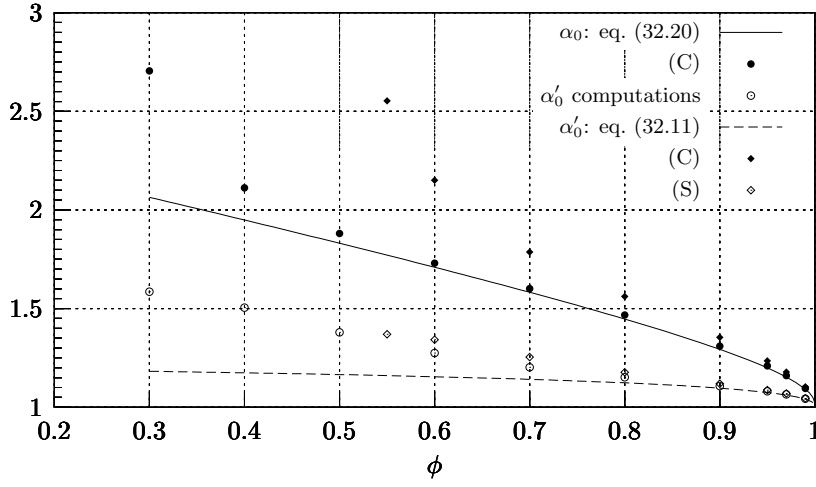


Figure 32.5: Plot of the characteristic viscous and thermal tortuosities α_0 and α'_0 for the cylinders (C) and the squares (S) compared with the analytical solution for a dilute cylinder configuration (lines).

Substituting (32.8) in (11.11), it is possible to write an expression for the thermal permeability k'_0

$$\frac{k'_0}{R^2} = \phi \frac{4c^4 \ln c - 3c^4 + 4c^2 - 1}{8(c^2 - 1)}, \quad (32.9)$$

which normalized with L^2 reads

$$\frac{k'_0}{L^2} = \frac{4 \ln c - 3 + 4c^{-2} - c^{-4}}{2\pi}. \quad (32.10)$$

For the static thermal tortuosity $\alpha'_0 = \lim_{\omega \rightarrow 0} \alpha'(\omega) = \langle T^2 \rangle / \langle T \rangle^2$, we find that

$$\alpha'_0 = \frac{2(-1 + c^2)}{3(1 - 4c^2 + 3c^4 - 4c^4 \ln(c))^2} \left[-2 + 15c^2 - 30c^4 + 17c^6 + 12c^4 \ln c(2 - 3c^2 + 2c^2 \ln c) \right]. \quad (32.11)$$

We notice that for characteristic thermal length $\Lambda' = 2V_f/A_{fs}$ we have the exact expression

$$\frac{\Lambda'}{R} = c^2 - 1, \quad (32.12)$$

valid for all porosities. Normalizing (32.12) with respect to L yields

$$\frac{\Lambda'}{L} = \frac{1}{\sqrt{\pi}} \frac{c^2 - 1}{c}. \quad (32.13)$$

For the Stokes flow, the velocity $\mathbf{v} = (v_r, v_\theta)$ can be expressed in terms of the stream function Ψ as $v_r = r^{-1} \partial \Psi / \partial \theta$, and $v_\theta = -\partial \Psi / \partial r$. The stream function Ψ satisfies the equation

$$\nabla^2(\nabla^2 \Psi) = 0, \quad (32.14a)$$

with the boundary conditions on the velocity

$$v_r = U \cos \theta, \quad \text{for } r = c, \quad (32.14b)$$

$$\nabla^2 \Psi = 0, \quad \text{for } r = c, \quad (32.14c)$$

$$v_r = v_\theta = 0, \quad \text{for } r = 1, \quad (32.14d)$$

where U is the velocity of the mean flow parallel to the line $\theta = 0$. The solution of (32.14) reads

$$\Psi(r, \theta) = \frac{c^2}{(4 \ln c - 3)c^4 + 4c^2 - 1} \left[(2c^2 - 1) \frac{1}{r} - (2c^2 - 2)r + 4c^2 r \ln r - r^2 \right] \sin \theta. \quad (32.15)$$

From the Stokes equation $\nabla p = \eta \nabla^2 \mathbf{v}$, it is possible to compute the pressure

$$p(r, c) = -8 \frac{c^2}{(4 \ln c - 3)c^4 + 4c^2 - 1} \left(\frac{c^2}{r} + \frac{r}{c^2} \right) \cos \theta + C, \quad (32.16)$$

where C is an additive constant. The macroscopic pressure gradient $\nabla_x \langle p \rangle$ along the x direction can be written as

$$\nabla_x \langle p \rangle = \frac{-p(c, \pi - \theta) + p(c, \theta)}{2c \cos \theta} = -8 \frac{c^2}{(4 \ln c - 3)c^4 + 4c^2 - 1}. \quad (32.17)$$

Writing the Darcy equation in the form $\phi \eta U = -k_0 \nabla_x \langle p \rangle$, we obtain an expression for the permeability k_0

$$\frac{k_0}{R^2} = \phi \frac{(4 \ln c - 3)c^4 + 4c^2 - 1}{16(c^2 - 1)}, \quad (32.18)$$

and normalizing with respect to L^2

$$\frac{k_0}{L^2} = \frac{4 \ln c - 3 + 4c^{-2} - c^{-4}}{4\pi}. \quad (32.19)$$

For the static thermal tortuosity $\alpha_0 = \lim_{\omega \rightarrow 0} \alpha(\omega) = \langle |\mathbf{v}|^2 \rangle / \langle |\mathbf{v}| \rangle^2$, we find that

$$\alpha_0 = \frac{(-1 + c^2)}{3(-c + 4c^3 - 3c^5 + 4c^5 \ln c)^2} \left[(c^2 - 1)(3 - 13c^2 - 7c^4 + 41c^6) + 24c^4(1 - 3c^4 + 2c^4 \ln c) \ln c \right]. \quad (32.20)$$

It is also possible to compute the viscous and thermal coefficients numerically. The viscous permeability k_0 , the tortuosity α_∞ , the static viscous tortuosity α_0 and the characteristic viscous length Λ are computed using a Finite Element code developed by Guermond based on the Uzawa decomposition method (Cortis *et al.*, 2001). The thermal permeability k'_0 and the thermal tortuosity α'_0 are computed using the Finite Element package SEPRAN (Cuvelier *et al.*, 1986).

ϕ	k_0/L^2	α_∞	α_0	Λ/L	M	M_{dil}
0.30	2.9200×10^{-4}	2.2345	2.7051	0.1773	0.5536	0.7122
0.40	2.2680×10^{-3}	1.7366	2.1121	0.3601	0.6074	0.7225
0.50	7.5100×10^{-3}	1.5400	1.8805	0.5365	0.6429	0.7269
0.60	1.8356×10^{-2}	1.4105	1.7297	0.7186	0.6685	0.7211
0.70	3.8876×10^{-2}	1.3020	1.6009	0.9256	0.6753	0.6969
0.80	7.7630×10^{-2}	1.2001	1.4675	1.2093	0.6371	0.6373
0.90	1.6107×10^{-1}	1.0999	1.3092	1.7668	0.5045	0.4976
0.95	2.5708×10^{-1}	1.0500	1.2096	2.5189	0.3583	0.3542
0.97	3.3243×10^{-1}	1.0300	1.1605	3.3228	0.2558	0.2637
0.99	5.0113×10^{-1}	1.0099	1.0955	5.6533	0.1280	0.1276

Table 32.1: *Characteristic viscous parameters for the arrangement of cylinders.*

ϕ	k'_0/L^2	α'_0	Λ'/L	M'	M'_{dil}
0.30	8.3940×10^{-3}	1.5854	0.4046	1.3673	0.6054
0.40	1.5589×10^{-2}	1.5043	0.5827	0.9183	0.5780
0.50	2.8297×10^{-2}	1.3799	0.7979	0.7112	0.5452
0.60	5.0514×10^{-2}	1.2750	1.0705	0.5878	0.5048
0.70	8.9835×10^{-2}	1.2020	1.4421	0.4937	0.4530
0.80	1.6329×10^{-1}	1.1514	2.0186	0.4007	0.3824
0.90	3.2507×10^{-1}	1.1074	3.2117	0.2801	0.2737
0.95	5.1506×10^{-1}	1.0803	4.7946	0.1887	0.1860
0.97	6.6519×10^{-1}	1.0654	6.3207	0.1373	0.1358
0.99	1.0023	1.0428	11.1784	0.0648	0.0644

Table 32.2: *Characteristic thermal parameters for the arrangement of cylinders.*

ϕ	k_0/L^2	α_∞	α_0	Λ/L	M
0.55	9.3775×10^{-4}	2.0509	2.5525	0.2254	0.5506
0.60	4.0068×10^{-3}	1.7251	2.1500	0.3768	0.6491
0.70	1.8911×10^{-2}	1.4306	1.7869	0.6355	0.7656
0.80	5.3356×10^{-2}	1.2579	1.5616	0.9243	0.7855
0.90	1.3451×10^{-1}	1.1220	1.3538	1.4174	0.6677
0.95	2.3056×10^{-1}	1.0600	1.2348	2.0431	0.4931
0.97	3.0616×10^{-1}	1.0358	1.1779	2.6481	0.3730
0.99	4.7542×10^{-1}	1.0119	1.1038	4.6021	0.1835

Table 32.3: *Characteristic viscous parameters for the arrangement of squares.*

ϕ	k'_0/L^2	α'_0	Λ'/L	M'
0.55	4.2983×10^{-2}	1.3703	0.8199	0.9301
0.60	5.3081×10^{-2}	1.3424	0.9487	0.7864
0.70	8.5593×10^{-2}	1.2538	1.2780	0.5989
0.80	1.5108×10^{-1}	1.1766	1.7889	0.4721
0.90	3.0451×10^{-1}	1.1188	2.8461	0.3342
0.95	4.9032×10^{-1}	1.0869	4.2485	0.2288
0.97	6.3876×10^{-1}	1.0700	5.6003	0.1680
0.99	9.7404×10^{-1}	1.0451	9.9000	0.0803

Table 32.4: *Characteristic thermal parameters for the arrangement of squares.*

The macroscopic parameters for the different configurations are presented in tables 32.1, 32.2, 32.3, and 32.4. The parameters α_0^{JKD} , and $\alpha_0'^{\text{JKD}}$ reported in these tables will be discussed in the following section. From the knowledge of the analytic solutions for the cylinders case, we can compute the values of the shape factors M_{dil} and M'_{dil} , where the subscript *dil* stands for dilute. These values are also reported in the tables.

In figures 32.2 to 32.5 we plotted the expressions in (32.5), (32.7), (32.10), (32.11), (32.13), (32.19), and (32.20), and the numerical results obtained computing the static viscous and thermal problems for both the cylinders and the squares. We notice that the dilute cylinders analytical solutions show an excellent agreement with the full numerical computations of the cylinders for values of the porosity $\phi > 0.7$. Only the static thermal tortuosity α_0' shows an agreement with computations starting from $\phi > 0.9$. From figure 32.2, we notice that the limit of the viscous and thermal permeabilities k_0 and k_0' goes to infinity for $\phi = 1$ for both the cylinders and the squares. This is nothing else than the so-called Stokes paradox (Lamb, 1932). However, this paradox is solved noticing that we are interested in the ratio of k_0/Λ^2 and, from figure 32.4, we observe that the characteristic lengths Λ tends also to infinity for ϕ that tends to one. In fact, it can be seen from (32.7) and (32.19) that the ratio k_0/Λ^2

$$\frac{k_0}{\Lambda^2} = (1 - \phi) \left(-\frac{3}{4} - \frac{1}{2} \ln(1 - \phi) \right) + \mathcal{O} \left((1 - \phi)^{3/2} \right) \quad (32.21)$$

remains always bounded, and goes to zero for $\phi = 1$.

We notice that for high porosities, also the values for the squares follow the dilute cylinder predictions. The value of k_0' for the squares and the cylinders remain very much the same for all porosities, whereas deviations between k_0 for the cylinders and the squares can be observed for $\phi < 0.9$. Analogously to the case of the thermal permeabilities, also the characteristic thermal lengths for the cylinders and the squares show a trend agreement for all values of porosity. A kind of “thermal” Stokes paradox also holds for the thermal permeability k_0' . Analogously to the viscous case, it can be

seen from (32.10) and (32.13) that the ratio k'_0/Λ'^2

$$\frac{k'_0}{\Lambda'^2} = (1 - \phi) \left(-\frac{3}{2} - \ln(1 - \phi) \right) + \mathcal{O} \left((1 - \phi)^{3/2} \right) \quad (32.22)$$

remains bounded for ϕ that tends to one.

§ 33 Direct dynamic numerical computations

In order to establish the validity of the Johnson and Pride scaling functions, we performed a large set of numerical simulations on the 2D porous media configurations depicted in figures 32.1. A detailed description of the geometries in figure 32.1 is given in § 32. The full dynamic flow problem (10.8) was solved using a Finite-Element based on the Uzawa decomposition method (Cortis *et al.*, 2001). The range of frequency chosen for the direct computations was between $\tilde{\omega} = 0.01$ and 100. We used an algorithm for the refinement of the FEM grid developed by Rebay (1993) which was already proved to be effective in Firdaouss *et al.* (1998), and Cortis *et al.* (2001). The full dynamic thermal problem (10.9) was solved using the Finite Element package SEPRAN (Cuvelier *et al.*, 1986). In order to better appreciate the differences at low frequencies between the computations and the models, we choose to represent the results as the real part of $\alpha(\omega) - 1$. Typical results are presented in figures 33.1 and 33.2.

In figure 33.1 (top) we plotted the results of the viscous problem for the cylinders configurations at two different porosities, namely $\phi = 0.4$ and 0.99. At high porosities, we observe that Johnson model deviates from the aforementioned scaling behavior. Please note that, for high porosities and at a frequency $\tilde{\omega} \approx 100$, the thickness of the viscous boundary layer δ is of the same order of magnitude of radius of the cylinder R , and the effects of the curvature of the pore wall on the potential flow in the bulk become predominant.

As expected, at low frequency, Johnson model was found to be off for all porosities deviating from $M/(4m)$, the theoretical limit predicted by Pride model and confirmed by the direct dynamic computations.

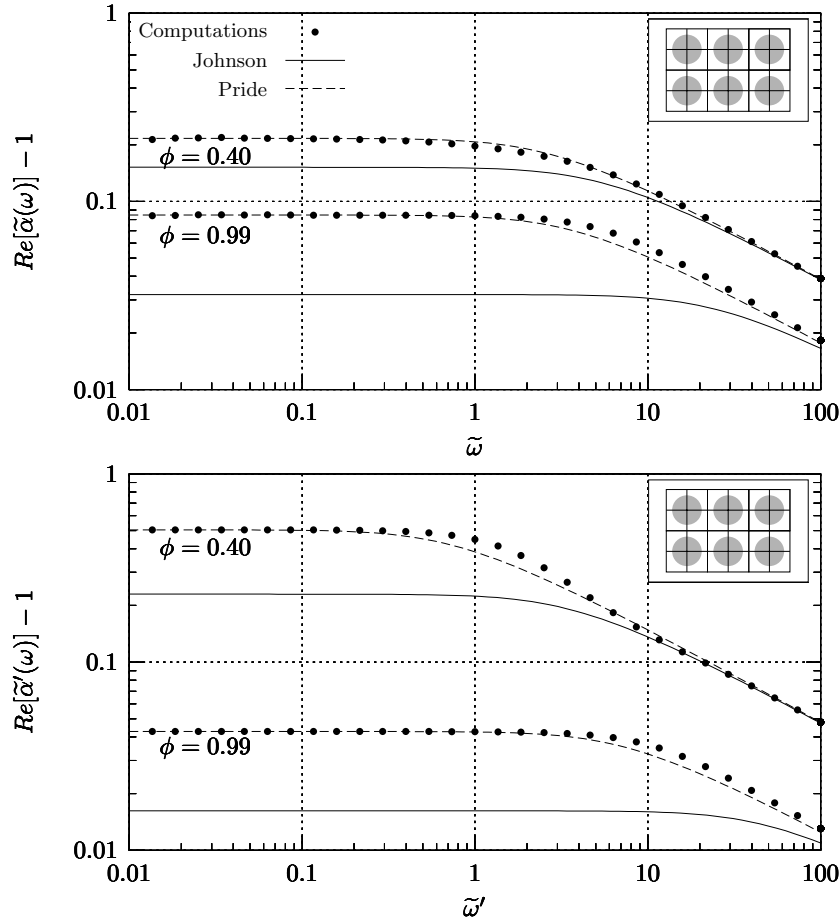


Figure 33.1: Plot of the real part of the dynamic tortuosity minus one, for an arrangement of solid cylinders at two different porosities $\phi = 0.4$ and $\phi = 0.99$. Top: viscous case. Bottom: thermal case.

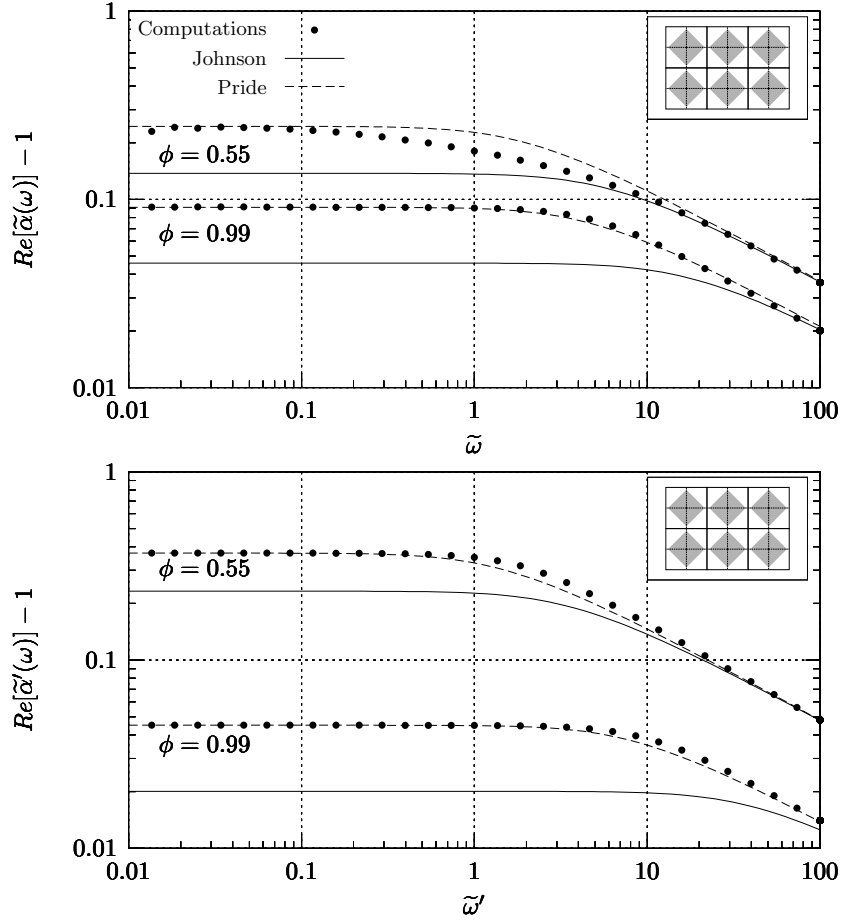


Figure 33.2: Plot of the real part of the dynamic tortuosity minus one, for an arrangement of solid squares at two different porosities $\phi = 0.55$ and $\phi = 0.99$. Top: viscous case. Bottom: thermal case.

The bottom plot in figure 33.1, shows the thermal dynamic computations of $\alpha'(\omega) - 1$ for the arrangement of cylinders. As for the viscous case, the high frequency limit is correctly predicted by both models for high and middle-range porosities, whereas at low frequencies, Johnson model start to deviate (see bottom figure 33.1 for $\phi = 0.99$) Also in this case, the low frequency limit of the Johnson model yields an incorrect prediction for α'_0 , at all porosities.

In figures 33.2, we plotted $\text{Re}[\alpha(\omega)] - 1$ (top) and $\text{Re}[\alpha'(\omega)] - 1$ (bottom) for the squares configuration at two different porosities, $\phi = 0.55$ and 0.99 . Analogously to the case of the cylinders, the Pride model (dashed line) perfectly predicts the direct numerical computations in both the high and low frequency at all porosities. Johnson model (drawn lines) converges to a lower value for α_0 , and α'_0 at all porosities, and start to deviate from the high frequency limit for high values of the porosity.

A comparison of the low frequency limits for the viscous and thermal static tortuosity of Johnson model (α_0^{JKD} , and $\alpha_0'^{\text{JKD}}$) and Pride model (α_0 , and α'_0), is presented in tables 32.1, 32.2, 32.3, 32.4. We notice that Johnson prediction (α_0^{JKD} , and $\alpha_0'^{\text{JKD}}$) underestimates the actual value (α_0 , and α'_0) for all values of ϕ , for both the cylinders and the squares.

§ 34 Causality

We want to investigate for which values of the parameters m , and M the dynamic permeability corresponding to the Pride model is causal.

It is obvious that once the causality requirement is satisfied for the viscous scaling function, then it is automatically satisfied for the thermal scaling function too, since the two functions differ only for the definition of their parameters. Therefore, we shall carry out our analysis on the viscous scaling function only. In fact, the causality requirement for a model function is equivalent to the require that all the poles of the model function itself belong to the upper plane of the complex frequency, $\text{Im}[\omega] > 0$. The analyticity and the long wavelength condition are satisfied when all the zeros, poles, and branch points lie on the positive imaginary axis of the complex frequency plane (Johnson *et al.*, 1987).

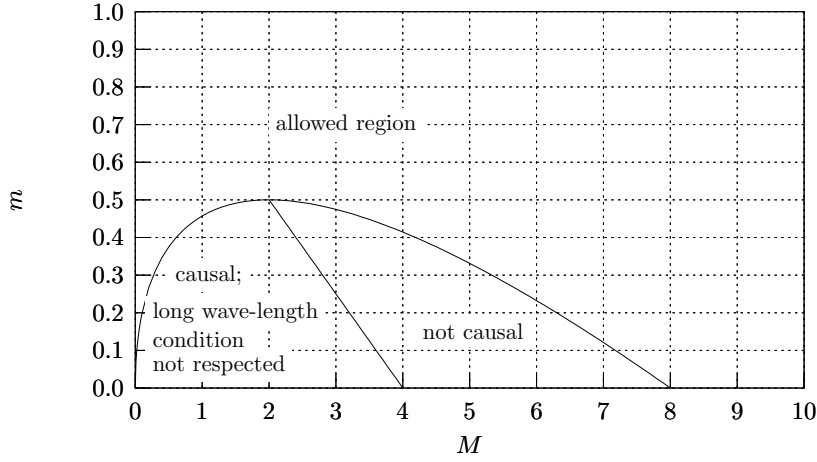


Figure 34.1: Graphical illustration of the allowed region of parameters in the (m, M) plane for the Pride model.

The only branch point, $\tilde{\omega}_b$, of $k(\omega)$ for the Pride model, is found from the square root in the complex-valued expression, and satisfies the condition

$$1 + \frac{M}{2m^2}i\tilde{\omega}_b = 0, \quad (34.1)$$

from which we see that $\tilde{\omega}_b$ lies on the imaginary positive axis, posing, therefore, no problems. We now analyze the poles of $k(\omega)$ (the zeros of $\alpha(\omega)$). We have a pole of the permeability when $\tilde{\omega}_p$ verifies

$$1 - m + m\sqrt{1 + \frac{M}{2m^2}i\tilde{\omega}_p} + i\tilde{\omega}_p = 0. \quad (34.2)$$

There are no other singularities of the permeability. Thus, to establish causality, it would suffice that all the solutions $\tilde{\omega}_p$ of (34.2) have $\text{Im}[\tilde{\omega}_p] \geq 0$. The long wavelength condition requires, in addition, $\text{Re}[\tilde{\omega}_p] = 0$. Please

notice that a solution of (34.2) is necessarily one of the two quantities

$$i\tilde{\omega}_p = 1 - m + \frac{M}{4} \pm \sqrt{\left(m + \frac{M}{4}\right)^2 - \frac{M}{2}}. \quad (34.3)$$

It is possible to locate three different regions in the (M, m) plane. When $m > \sqrt{M/2} - M/4$, we have that $\text{Im}[\tilde{\omega}_p] \geq 0$ and $\text{Re}[\tilde{\omega}_p] = 0$, i.e., Pride model is causal and respects the long wavelength condition. On the other hand, when $m < \sqrt{M/2} - M/4$, we find that $\text{Re}[\tilde{\omega}_p] \neq 0$, which means that Pride does not respect the long wavelength condition and is thus not-allowed. We can split the region $m < \sqrt{M/2} - M/4$ in two sub regions, viz, the region $m < 1 - M/4$ for which $\text{Im}[\tilde{\omega}_p] \geq 0$ and Pride model is causal, and the region $m > 1 - M/4$ for which $\text{Im}[\tilde{\omega}_p] \leq 0$ and Pride model is not causal. These three regions are illustrated in figure 34.1.

In figure 34.2, we plotted values for the viscous and thermal parameters m , m' , M , and M' in a similar figure as figure 34.1. The m -values are obtained from the relations

$$m = \frac{M}{4(\alpha_0/\alpha_\infty - 1)}; \quad m' = \frac{M'}{4(\alpha'_0 - 1)}; \quad (34.4)$$

Also the values estimated from the Chapman & Higdon (1992) dynamic computations on arrangement of spheres are plotted. We notice that causality is respected indeed. Moreover, our numerical data and the Chapman & Higdon (1992) 3D computations agree very well.

§ 35 Conclusions

We analyzed two scaling functions, namely the Johnson *et al.* (1987) model and the Pride *et al.* (1993) model, describing the frequency-dependent viscous and thermal interaction of an ideal gas saturating a porous medium. These two models depend on two parameters, M and m , whose value is determined once the microgeometry of the porous material is given. We performed a large set of direct dynamic computations of the viscous and

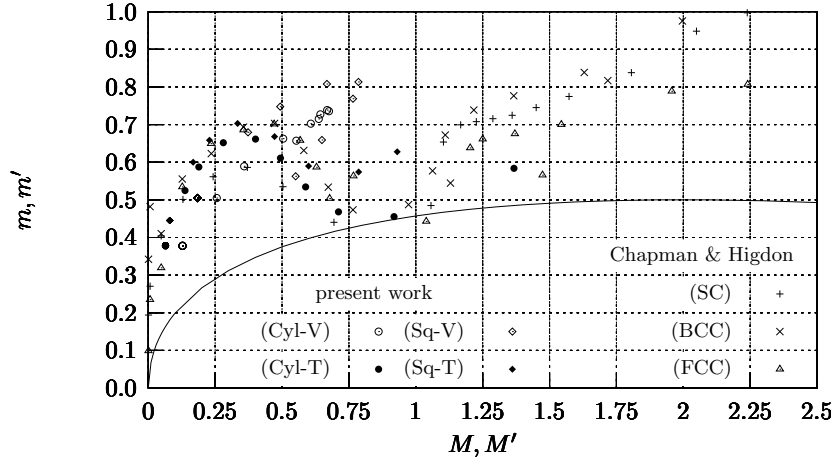


Figure 34.2: Values of the shape factors m , and M , for the cylinders (Cyl) and the squares (Sq), for the viscous (V) and thermal case (T). Comparison with the estimated values obtained from the Chapman & Higdon (1992) 3D-spheres computations: (SC): simple cubic, (BCC): body centered cubic, (FCC): face centered cubic. The drawn line defines the allowed region of parameters for the Pride model.

thermal problems on microgeometries consisting in arrangements of cylindrical and squared fibers at different porosities. We then computed the model parameters for these geometries and compared the direct dynamic computations with the corresponding Pride and Johnson scaling functions. We found that, at low frequency, Johnson model is off for all values of porosities, both for the viscous and the thermal problem. Excellent agreement was found between the Pride model and the direct computations, at low and high frequencies, for both the viscous and the thermal problem in the whole porosity range.

APPENDIX TO CHAPTER V

§ 36 Causal models for viscous and thermal dynamic dissipation

In the present section we propose an expression for the viscous and thermal scaling functions as follows. We give two different expressions for 2D and the 3D case respectively. Let's define:

$$z = \sqrt{\frac{P}{p^2}} 3i\tilde{\omega}, \quad M = \frac{8k_0\alpha_\infty}{\phi\Lambda^2}, \quad m = \frac{P}{4\left(\frac{\alpha_0}{\alpha_\infty} - 1\right)}. \quad (36.1)$$

The expression for the 2D case reads:

$$F(\tilde{\omega}) = 1 - p + \frac{1}{3}pz^2 \frac{\tanh(z)}{z - \tanh(z)}, \quad (36.2)$$

where

$$P = \frac{3}{2}M, \quad p = \frac{4}{5}m. \quad (36.3)$$

The expression for the 3D case reads:

$$F(\tilde{\omega}) = 1 - 2p + \frac{1}{4}pz^2 \frac{A(z)}{z - A(z)}, \quad (36.4)$$

where

$$A(z) = 2i \frac{J_1(-iz)}{J_0(iz)}, \quad (36.5)$$

$$P = M, \quad p = m. \quad (36.6)$$

Please notice that these models satisfy both the theoretical low- high-frequency limits, just as Pride model. Our models can be naturally extended to cover the dynamic thermal dissipation case.

In figures 36.1 we plotted the function $Re[(i\omega)^{-1}F(\omega)] = Re[\alpha(\omega) - 1]$ for the slit (top) and tube (bottom) flow, for the Johnson model, the Pride

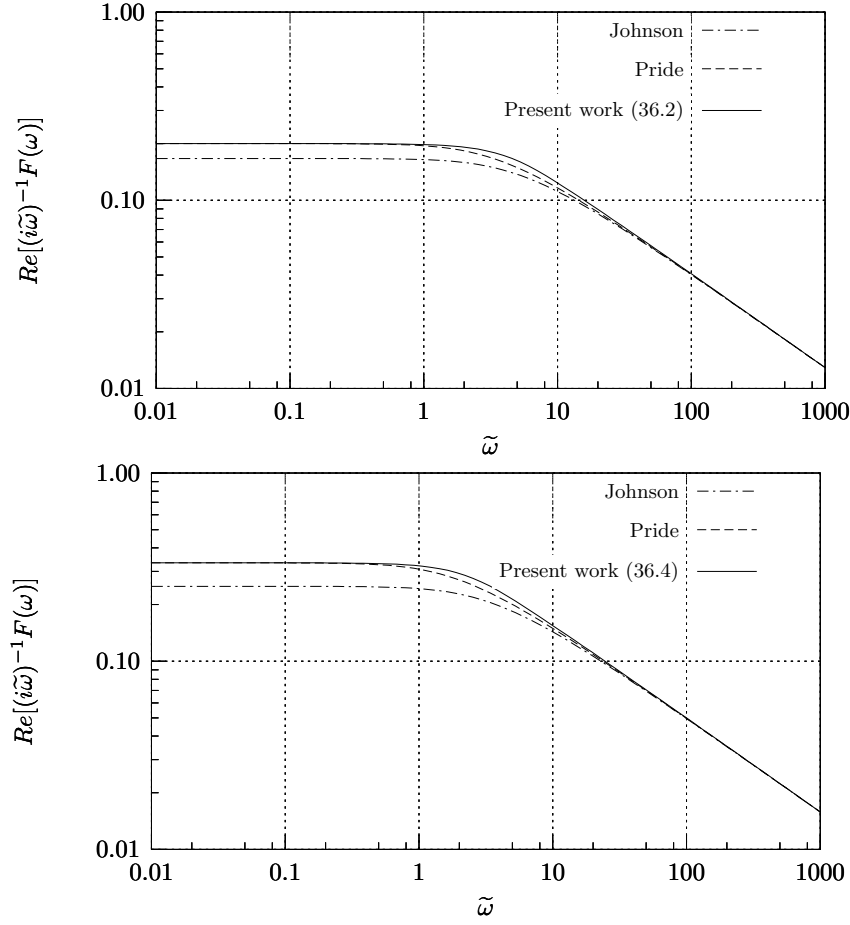


Figure 36.1: Plot of $(i\tilde{\omega})^{-1}F(\omega)$ for Johnson model (31.2), Pride model (31.5), and the models proposed in the present work (36.4). Top: slit flow. Bottom: tube flow.

model, and the models proposed in the present work. We notice that our models depart significantly from the Pride model only in the range of frequencies $\tilde{\omega} = 1 - 50$.

It is quite difficult to tackle the study of the poles of (36.2), and (36.4) from an analytic point of view. It is however possible to find the poles numerically. A Mathematica program was written to find numerically the poles of (36.2), and (36.4). Our findings indicate that the poles are always located on the imaginary positive axis for all the possible combinations of m and M , therefore ensuring, the causality of (36.2), and (36.4). In figures 36.2 we plotted the functions $(F(\omega) + i\tilde{\omega})$ for the 2D case (top), and for the 3D case (bottom) against the imaginary frequency $i\tilde{\omega}$, for the couple of parameters $m = 0.1$, and $M = 1$, which make Pride function non-causal. We notice that all the zeros of this two functions (the poles of $k(\omega)$) belong to the positive part of the imaginary axis proving, therefore, our claim.

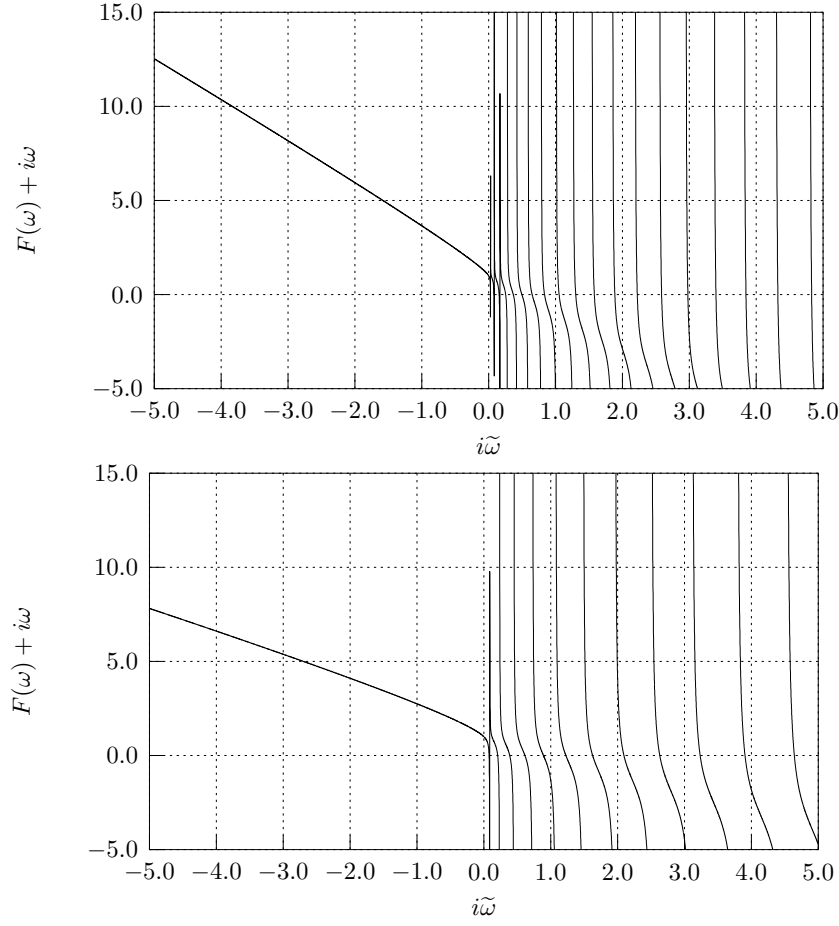


Figure 36.2: Plot of $F(\omega) + i\omega$ vs the imaginary frequency $i\tilde{\omega}$. $m = 0.1$; $M = 1.0$. Top: 2D model function described in (36.2). Bottom: 3D model function described in (36.4). The zeros of this function lie exclusively on the positive part of the imaginary axis.

CHAPTER VI

VISCOUS DYNAMIC PERMEABILITY: THEORY AND EXPERIMENTS

In this Chapter we present the results of some laboratory experiments on the dynamic viscous permeability performed in order to validate the numerical computations and the scaling functions already broadly discussed in Chapters IV and V. In §37 we give an overview of the previous experimental works on the frequency-dependent flow experiments in porous media. The porous media under investigation is a stack of orifice plates as described in §38. The choice of this particular model porous medium, was suggested by the possibility of a direct accurate comparisons between the experiments and the numerical results of the FEM computations on the same micro-geometry. Experiments on the static viscous permeability, and the dynamic viscous tortuosity, and the comparison with their predicted numerical values, makes the object of §39, and §40 respectively. The experiments on the dynamic viscous permeability and their comparison with both the FEM computations, and the scaling model are described in §41, where we also present the experimental measurements on the viscosity of the saturating fluid.

§ 37 In-series tube geometry

Experiments on the dynamic viscous permeability of porous media were already the object of previous studies. Auriault *et al.* (1985) were the first

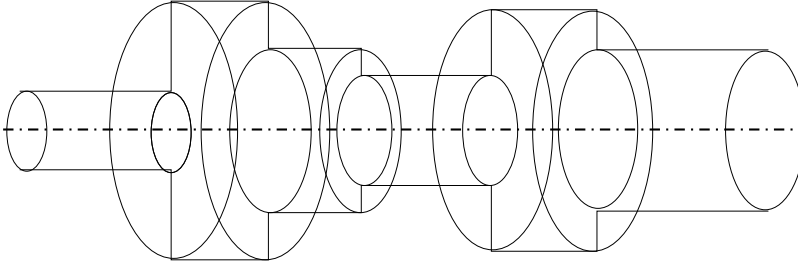


Figure 37.1: *In-series tubes model.*

to report experimental results on dynamic viscous permeability in porous media for an in-series slit geometry. Their measurements were performed in the non-dimensional frequency range $\tilde{\omega} = 10^{-2} - 10^2$. Charlaix *et al.* (1988) reported experimental measurements of $k(\omega)$ for a variety of fused crushed glass beads in the same non-dimensional frequency range of Auriault *et al.* (1985). Smeulders *et al.* (1992) presented a series of measurements on porous media samples consisting of glass and sand glued beads. Kelder (1998) performed experiments on glued glass beads, and permeable ceramic materials like the ones used in Johnson *et al.* (1994). All these experimental works confirmed the universal behavior for $k(\omega)$ predicted by Johnson's theory (see Chapter IV).

In this Chapter we compare numerical predictions and laboratory experiments for a simple in-series tube geometry. The in-series tube model, is a model porous medium idealized as a long capillary tube formed of N straight elements of length L_i , $i = 1, \dots, N$ ($L = \sum L_i$), with circular cross sections of radius R_i (see figure 37.1). This type of geometry has been often modeled in terms of simple lubrication theory, which is also known as Reynolds flow, or cubic law approximation (Achdou & Avellaneda, 1992; Pride *et al.*, 1993; Kelder, 1998). Assuming lubrication theory, it is possible to derive the following expressions for the macroscopic parameters of the dynamic viscous dissipation (Achdou & Avellaneda, 1992; Kelder, 1998). First we define the length-weighted average valid for piece-wise varying

cross sections:

$$\sum_{i=1}^N \frac{L_i}{L} R_i^n = \|R^n\|, \quad (37.1)$$

where n is an integer. With the notation in (37.1), it is possible to express the permeability k_0 as

$$\frac{k_0}{\phi} = \frac{1}{8} \frac{1}{\|R^2\| \|R^{-4}\|}, \quad (37.2)$$

the permeability α_∞ as

$$\alpha_\infty = \|R^2\| \|R^{-2}\|, \quad (37.3)$$

and the characteristic viscous length Λ as

$$\Lambda = \frac{\|R^{-2}\|}{\|R^{-3}\|}. \quad (37.4)$$

Thus, the shape factor M reads

$$M = \frac{8k_0\alpha_\infty}{\phi\Lambda^2} = \frac{\|R^{-3}\|^2}{\|R^{-4}\| \|R^{-2}\|}. \quad (37.5)$$

From (37.5) we notice that $M < 1$, because of the Cauchy-Schwartz inequality $\|R^{-3}\|^2 = (\|R^{-1}\| \|R^{-2}\|)^2 < \|R^{-2}\| \|R^{-4}\|$. The expression for the dynamic permeability $k(\omega)$ in the Reynolds flow approximation is clearly an harmonic average of the individual permeabilities $k_i(\omega)$

$$k(\omega) = \|k_i(R_i, \omega)^{-1}\|^{-1}, \quad (37.6)$$

where

$$k_i(R_i, \omega) = \frac{8\nu}{iR_i^2\omega} \left(1 - \frac{2J_1(i^{3/2}R_i\sqrt{\omega/\nu})}{i^{3/2}R_i\sqrt{\omega/\nu}J_0(i^{3/2}R_i\sqrt{\omega/\nu})} \right), \quad (37.7)$$

is the expression valid for the tubes model.

Lubrication theory can be a very good approximation for the full Stokes problem for channel-like porous media with slowly varying cross-section

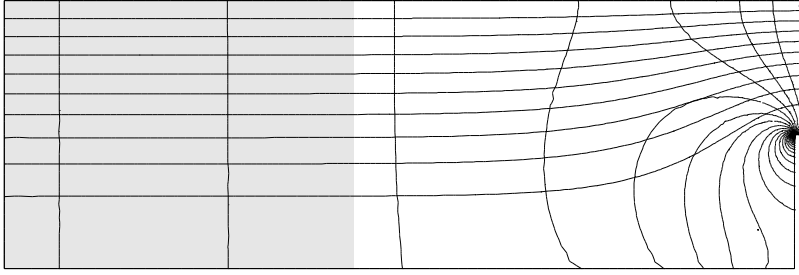


Figure 37.2: *Plot of the streamlines and iso-pressure lines for a 2D in-series slit model: a quarter of the computational cell is showed.*

(Pride *et al.*, 1993), but it happens to be a very poor approximation when the geometric constraint on the cross-sections is not satisfied (Cortis, 1997; Oron & Berkowitz, 1998). This is illustrated in figure 37.2 where we plotted the streamlines for the Stokes flow for a 2D in-series slit configuration: a quarter of the computational cell is showed. It can be seen that for a large part of the wide tube (gray zone), the flow is very much undisturbed, but in the proximity of the narrow tube we cannot assume an undisturbed approximation of the pressure profile. Thus, the vertical components of the velocity, which are neglected in the Reynolds flow approximation, play a prominent role for this type of in-series tube models.

Our micro-geometry consists of a stack of orifice plates separated by rings (see figure 37.3). The sample was saturated with a solution of glycerol and water. The choice of this specific configuration was motivated by its characteristic sharp-edge obstruction to the fluid flow, and because of its simple axial-symmetric geometry. It is possible to find in literature many experimental works on the oscillating flow through a singular circular orifice inside a circular tube. Among the many of them we can cite Thurston & Wood (1953), Thurston & Martin (1953), Thurston (1952), and Elger & Adams (1989). However, our experiment is different from the ones of the aforementioned papers because the number of orifices considered is much larger. Each of the individual cells between two consecutive plates can

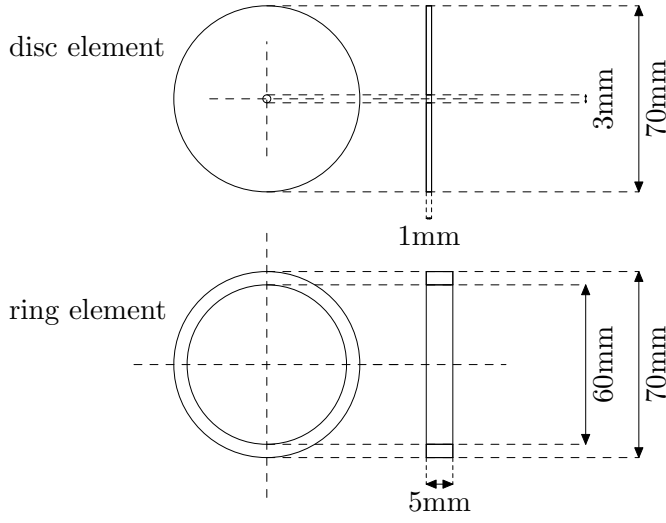


Figure 37.3: *Schematics of the rings and plates used in the experiments with relevant dimensions.*

be therefore considered a typical REV of the all porous medium. This justifies the averaging procedures defined in § 2 on both the pressure and velocity fields. Furthermore the characteristic dimension of the pore throat (the orifice) is much smaller than the macroscopic length over which the pressure drop is measured, satisfying the constraint on the separation of the length scales.

We report laboratory experiments for the static parameters k_0 , α_∞ , for the viscosity η of the saturating fluid, and finally for the viscous dynamic permeability $k(\omega)$. We are in a position to compare our measurements against the calculated values, with no adjustable parameters. We will show that the presence of the sharp-edge does not induce a large value of the shape factor M in the dynamic viscous permeability. On the contrary, we find that the value of M remains close to one.

§ 38 The porous medium under study

The porous medium under study consists of a stack of ten orifice plates separated by nine ring elements. Geometry and relevant dimensions are indicated in figure 37.3. Two sets of orifice plates have been used: one set of metallic plates for the dynamic viscous measurements, and another of plastic ones for the static permeability, and tortuosity measurements. The spacing rings were in both cases made out of plastic material. The diameter of the orifices were 2.95 ± 0.03 mm.

The numerical values of the viscous dynamic permeability were obtained by solving the Stokes problem (10.12) and averaging the velocity solution on the pore-fluid domain using (10.13), as described in Chapters II, IV, and V. The problem was solved in axi-symmetric coordinates, and the grid refinement technique described in Chapter IV was used to obtain detailed description of the flow around the tip of the orifice.

The Stokes flow finite element computations of the static parameters k_0 , α_∞ , α_0 , and Λ are summarized in table 39.1, where we also reported the values obtained by means of the Reynolds flow approximation. We notice that the macroscopic parameters obtained by means of the Reynolds flow approximation are considerably different from the ones obtained from the Stokes flow computations. We also notice that the characteristic viscous length, computed according to Johnson's formula (24.13), is equal to $\Lambda = 1.292$ mm, a value close to that of the radius of the orifice ($r = 1.475$ mm). This is consistent with the definition of Λ as a viscous characteristic length of the pore scale. The value of the tortuosity was $\alpha_\infty = 163.67$. To our knowledge no such high value of the tortuosity was previously reported in literature. However, from the computations, the ratio of α_0/α_∞ was equal to 1.45, close to $4/3$, the theoretical value for a straight tube. Despite the sharp-edge geometry and the extremely high value of the tortuosity the computed set of parameters yielded a value of the shape factor $M = (8k_0\alpha_\infty)/(\phi\Lambda^2) = 1.46$.

We performed FEM computations of the dynamic permeability, $k(\omega)$, in the frequency range $\tilde{\omega} = 10^{-2} - 10^2$, solving the full Stokes problem (10.8), as described in Chapters II, V, and IV. In figure 38.1, we plotted the

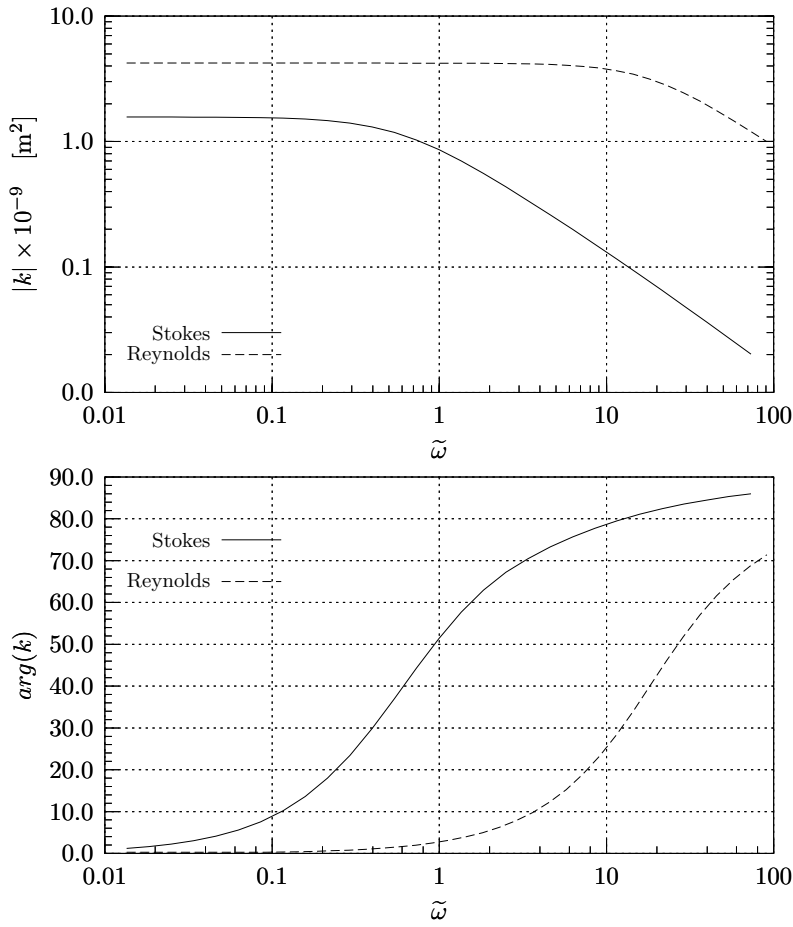


Figure 38.1: *Plots of the dynamic permeability, $k(\omega)$ for the Stokes flow equations (10.8) (drawn line), and Reynolds flow approximation (37.6) (dashed line). Top: absolute value. Bottom: phase shift. The characteristic frequency was computed by means of the Stokes flow macroscopic parameters.*

	$k_0 \times 10^{-9} [\text{m}^2]$	α_∞	α_0	$\Lambda \times 10^{-3} [\text{m}]$	M
experiments	1.577 ± 0.02	156.68			
Stokes	1.554	163.67	237.89	1.292	1.46
Reynolds	4.218	56.28		1.518	0.99

Table 39.1: *Macroscopic parameters for the geometry under study: Laboratory experiments, Stokes flow computations, and Reynolds flow computations. The porosity of the sample was $\phi = 0.8337$.*

results of these numerical computations and we compared them with the simple lubrication theory, described in (37.6) and (37.7). We notice that lubrication theory represents a poor approximation of the flow patterns which are actually taking place inside our porous medium.

§ 39 Static permeability measurements

The experiments on the static permeability, k_0 , were performed in a conventional permeability set up. A fluid head smaller than 2 cm was imposed to induce the fluid flow through the sample. The pressure drop was measured by means of a differential manometer, and the mass flow was measured with a mass balance: both devices were interfaced with a computer which recorded pressure, and mass flow against time. The saturating fluid was a solution of glycerol and water (68.8% in weight). This solution had a value of viscosity high enough to ensure that the experiments were performed in a flow regime characterized by values of the Reynolds number, $Re < 10$, with respect to a characteristic length scale of the pore (in this case the diameter of the orifice). Three experiments were performed at different fluid temperatures. Results are summarized in figure 39.1, where we plotted the recorded mass flow against the driving head. The experimental value for k_0 reported in table 39.1 is the average value of the three different experiments (see table 39.2). The relative error of the experiment to the computations is thus equal to 1.5%.

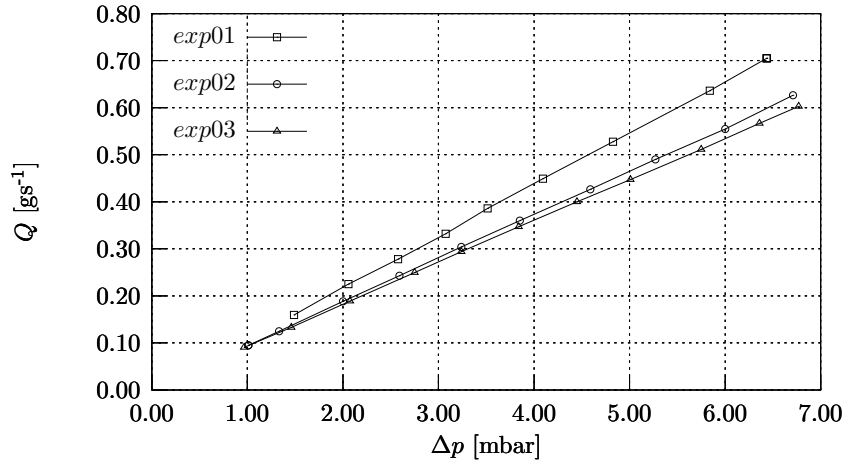


Figure 39.1: *Experimental results for the static permeability. The volume flow Q against the driving head Δp is plotted. The three curves correspond to three different fluid temperatures (see table 39.2).*

	T []	$k_0 \times 10^{-9}$ [m ²]
exp01	26.70	1.597
exp02	24.45	1.555
exp03	23.55	1.581

Table 39.2: *Temperatures and permeabilities for the three laboratory experiments.*

§ 40 Experiments on the tortuosity

The experimental value of the tortuosity was determined by means of an electrical resistivity measurement technique. Tortuosity and resistivity are related by the formula $\alpha_\infty = \phi r_s / r_f$ (Brown, 1980), where r_s is the intrinsic resistivity [Ωm] of the fluid-filled porous insulator, and r_f is the intrinsic fluid resistivity. The ratio α_∞ / ϕ is also known as formation factor. The rings and plates (10 cells) porous sample was placed inside the measurement cell. For this experiment, the ring and plates were made of plastic material to ensure electric insulation. The sample was fully saturated with a 10% wt NaCl-water solution. Resistances were measured with a Wayner-Kerr resistance bridge. The applied electric voltage had a frequency of 10 kHz. The measured values were: $R_f = 109 \Omega$, and $R_s = 20485 \Omega$, giving a value of $\alpha_\infty = 156.68$. From the computations we had a value of $\alpha_\infty = 163.67$. The relative error of the experiment to the computations is thus equal to 4.3%.

§ 41 Dynamic measurements

In order to measure the frequency-dependent permeability we used the experimental set-up developed by Kelder (1998), which is an improved version of the one used by Smeulders *et al.* (1992). The setup is shown in figure 41.2. An oscillating pressure gradient was induced by a vibration exciter driving a rubber membrane. The vibration exciter was controlled by a waveform generator driving a power amplifier, inducing an oscillating flow with a frequency from 20 to 200 Hz. Hence the wavelength is much larger than the length of the porous sample and the fluid may be regarded as incompressible. The pressure drop across the porous sample was measured using two piezo-electric transducers. The first pressure transducer was installed in the stiff steel body of the set-up in order to reduce resonance disturbances, while the second one was mounted on the lower end of a cylindrical Perspex shaft, fixed to a separate steel framework. The pressure signals were recorded as electric charge, and converted by Kistler 5011 amplifiers, to obtain a proportional analogue voltage. Effective noise

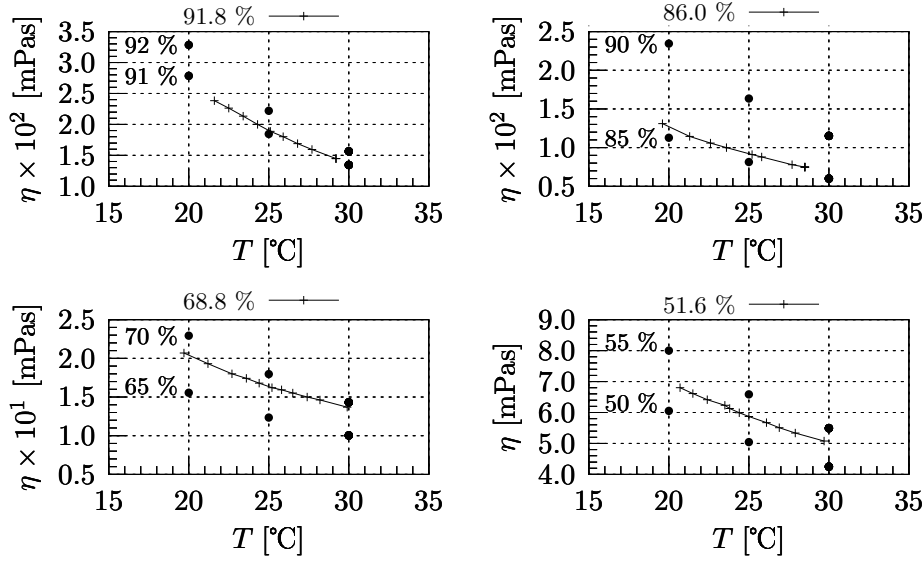


Figure 41.1: *Viscosity experiments for the solutions of glycerol and water. Solid lines and crosses represent the viscosity η as a function of the temperature. Full circles represent available data in literature (Janssen & Warmoeskerken, 1987, p. 146). Each of the four pictures corresponds to a different weight proportion of glycerol and water in the mixture as indicated on the top of each graph.*

reduction in the recorded signals was obtained by signal averaging during the measurements. The signals were then transformed to the frequency domain by means of a Fast Fourier Transform algorithm.

In order to cover a wide range of frequencies a suitable choice of the fluid viscosity and density was needed. We used for our experiments four different glycerol-water solutions, namely 51.6 wt-%, 68.8 wt-%, 86.0 wt-%, and 91.8 wt-% glycerol. We measured the viscosities of those solutions in a Low-Shear viscosimeter as a function of the fluid temperature (see figure 41.1). The points were fitted by third order polynomials whose coef-

wt-% gly	viscosity [mPa s]	density ρ [kg m ⁻³]
91.8	$\eta = 0.0322T^3 - 2.0323T^2 + 28.055T + 256.32$	1231.19
86.0	$\eta = -0.0403T^3 + 3.1852T^2 - 88.782T + 950.90$	1215.75
68.8	$\eta = -0.0015T^3 + 0.1344T^2 - 4.6262T + 70.836$	1165.46
51.6	$\eta = 0.0005T^3 - 0.0367T^2 + 0.6052T + 5.1380$	1119.16

Table 41.1: *Polynomial expressions of the measured viscosities as a function of the fluid temperature T in °C. Each row corresponds to a different composition of the glycerol-water solution, whose relative weight proportion is indicated in the first column.*

ficients are presented in table 41.1. Results show a within range agreement with the available literature data (Janssen & Warmoeskerken, 1987). In figure 41.2b we give a schematics of the porous sample used with the relevant dimensions. The porous sample has a length L_p , and a cross section area equal to A_{tot} . The sample is fully saturated, and the free surface of the fluid is located at a height, $L_s + x_2$, over the top surface of the porous sample. The perspex shaft holding the top transducer, p_2 , has an area equal to A_d , and is located at a distance x_2 from the top surface of the sample. The bottom transducer, p_1 , is at a distance x_1 from the bottom surface of the porous sample.

We notice that the velocity \hat{v}_2 can be obtained by the momentum equation over the distance L_s :

$$\frac{\hat{p}_2}{L_s} = -\rho i \omega \hat{v}_2. \quad (41.1)$$

The macroscopic fluid velocity \hat{w} within the porous sample, follows from the continuity equation

$$\phi \hat{w} = \frac{A_{tot} - A_d}{A_{tot}} \hat{v}_2. \quad (41.2)$$

Using the momentum equations over the distance x_1 , and x_2 , it is possible to express pressure amplitudes at the top and the bottom of the sample as

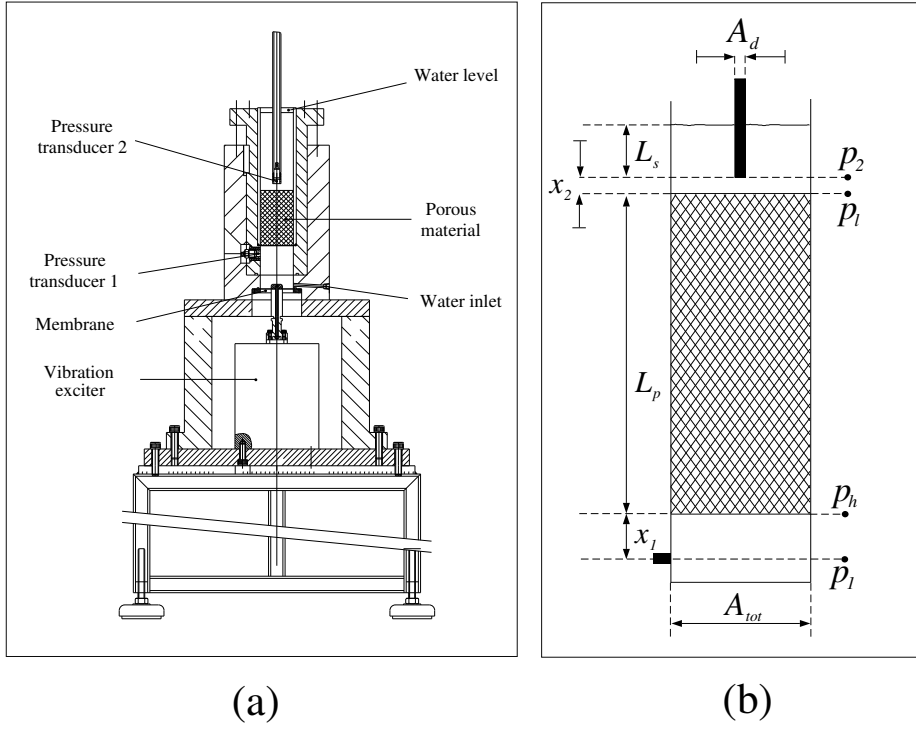


Figure 41.2: (a) *Dynamic Darcy Cell for dynamic permeability measurements.* (b) *Detailed sketch with relevant dimensions of porous material and its surroundings.* (After Kelder (1998) with permission.)

functions of the recorded pressure amplitudes \hat{p}_1 and \hat{p}_2 :

$$\hat{p}_h = \hat{p}_1 - \frac{A_{tot} - A_d}{A_{tot}} \frac{x_1}{L_s} \hat{p}_2, \quad (41.3)$$

$$\hat{p}_l = \hat{p}_2 + \frac{A_{tot} - A_d}{A_{tot}} \frac{x_2}{L_s} \hat{p}_2. \quad (41.4)$$

It is now possible to deduce the value of the dynamic permeability $k(\omega)$

from the equation:

$$\frac{\eta\phi}{k(\omega)}\hat{w} = \frac{\hat{p}_h - \hat{p}_l}{L_p}. \quad (41.5)$$

A measure of the fluid temperature was made at each frequency shot during dynamic measurements. The corresponding viscosity was deduced from the polynomial expressions in table 41.1.

Particular care was paid to avoid the presence of air bubbles in the saturating fluid.

Charlaix *et al.* (1988) reported that even bubbles of the size of a fraction of a millimeter can significantly affect the experimental results. The relatively high viscosities of the fluids used in our dynamic experiments made this issue particularly important. Another point that made extremely difficult the dynamic permeability measurements was the very low value of the applied pressure, due to the relatively high value of the static permeability k_0 . In fact, in order to ensure linearity of the flow, we had to keep the Reynolds number $Re < 10$. For $Re \approx 10$, extra-harmonic components in the Fourier spectrum were observed, and for larger Reynolds numbers, a chaotic behavior appeared. Therefore low energy inputs had to be used when dealing with our lowest values of the viscosity, leading to a lower value of the signal-to-noise ratio.

Six experiments with different saturating fluids were performed: the set of the weight compositions is reported in table 41.1.

In figures 41.3, we plotted the measured dynamic permeability, $k(\omega)$ for the different experiments, together with the Stokes flow numerical computations and the Pride model function. As it can be seen from figure 41.3, we have found a satisfactory agreement between the measurements and the computations.

§ 42 Conclusions

In this Chapter, we presented the results of laboratory experiments on the dynamic permeability of a porous medium consisting in stack of orifice-plates, saturated with a glycerol-water solution. Experiments were made

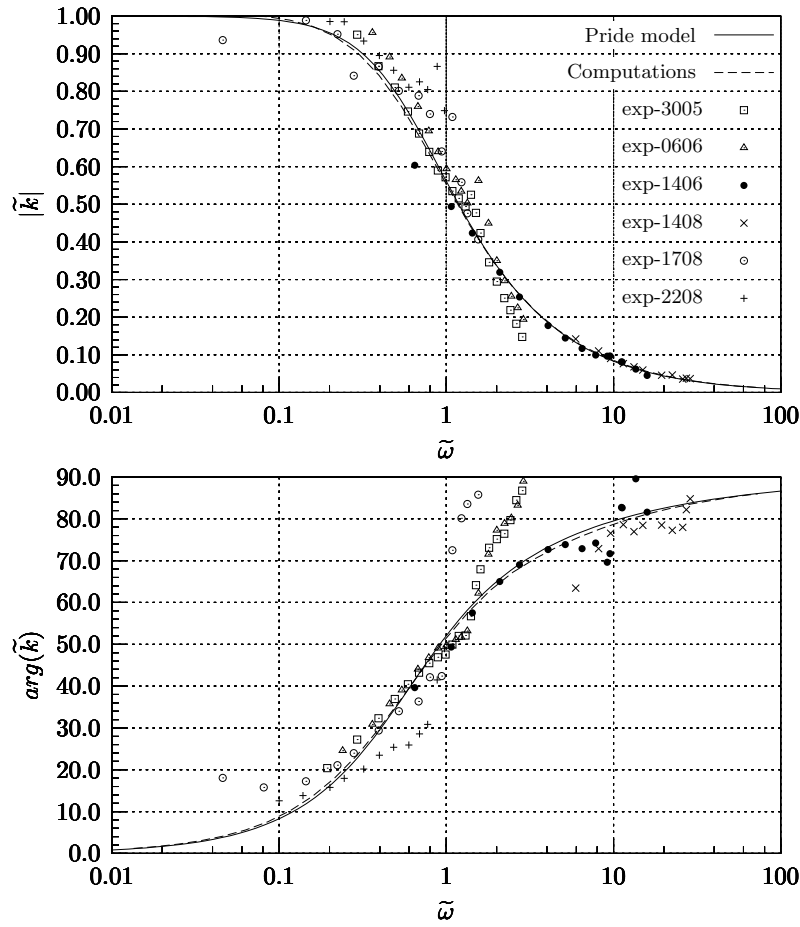


Figure 41.3: Comparison of laboratory experiments and computations on viscous dynamic permeability for the arrangement of orifice-plates. Top: absolute value. Bottom: phase shift (same legend as top). Composition of the saturating glycerol-water fluid in weight: (\square) 86.0 %; (\triangle) 86.0 %; (\bullet) 68.8 %; (\times) 51.6 %; (\circ) 91.1 %; (+) 91.1 %.

to determine dependence of the viscosity of the saturating fluids with the temperature, for different proportions of the glycerol and water. The static permeability of the porous medium was measured in a conventional Darcy cell: the experiments are in perfect agreement with the FEM computations. The tortuosity was also measured saturating the sample with a NaCl-water solution and measuring the electric resistance with a Wayner-Kerr bridge. Finally, we performed experiments on the frequency-dependent permeability and compared the results with the frequency-dependent Stokes flow computations. The experiments are in satisfactory agreement with the computations. Finally, we notice that the simple lubrication theory fails to predict the experimental results.

BIBLIOGRAPHY

- ABRAMOWITZ, M. & STEGUN, I. 1970 *Handbook of mathematical functions*. Dover publications, Inc., New York.
- ACHDOU, Y. & AVELLANEDA, M. 1992 Influence of pore roughness and pore-size dispersion in estimating the permeability of a porous medium from electrical measurements. *Phys. Fluids A* **4** (12), 2561–2673.
- ALLAIRE, G. 1996 *One-phase newtonian flow*, pp. 45–69. Springer.
- AURIAULT, J.-L., BORNE, L. & CHAMBON, R. 1985 Dynamics of porous saturated media, checking of the generalized law of Darcy. *J. Acoust. Soc. Am.* **77** (5), 1641–1650.
- AVELLANEDA, M. & TORQUATO, S. 1991 Rigorous links between fluid permeability, electrical conductivity, and relaxation times for transport in porous media. *Phys. Fluids A* **3** (11), 2529–2540.
- BARRÈRE, J., GIPOLOUX, O. & WHITAKER, S. 1992 On the closure problem for Darcy's law. *Transport Porous Med.* **7**, 209–222.
- BIOT, M. 1956*a* Theory of propagation of elastic waves in a fluid-saturated porous solid. I. Low-frequency range. *J. Acoust. Soc. Am.* **28**, No.2, 168–178.
- BIOT, M. 1956*b* Theory of propagation of elastic waves in a fluid-saturated porous solid. II. Higher-frequency range. *J. Acoust. Soc. Am.* **28**, No.2, 179–191.
- DE BOER, R. 2000 *Theory of porous media*. Springer.
- BOURGEOAT, A., QUINTARD, M. & WHITAKER, S. 1988 Éléments de comparaison entre la méthode d'homogénéisation et la méthode de prise de moyenne avec fermeture. *C. R. Acad. Sc. Paris* **306**, Série II, 463–466.
- BROWN, R. 1980 Connection between formation factor for electrical resistivity and fluid-solid coupling factor in biot's equations for acoustic waves in fluid-filled porous media. *Geophysics* **45** (8), 1269–1275.
- BURRIDGE, R. & KELLER, J. 1981 Poroelasticity equations derived from microstructure. *J. Acoust. Soc. Am.* **70**(4), 1140–1146.

- CHAMPOUX, Y. & ALLARD, J.-F. 1991 Dynamic tortuosity and bulk modulus in air saturated porous media. *J. Appl. Phys.* **70** (4), 1975–1978.
- CHAPMAN, A. & HIGDON, J. 1992 Oscillatory Stokes flow in periodic porous media. *Phys. Fluids A* **4** (10), 2099–2116.
- CHARLAIX, E., KUSHNICK, A. & STOKES, J. 1988 Experimental study of dynamic permeability in porous media. *Phys. Rev. Lett.* **61** (14), 1595–1598.
- CORTIS, A. 1997 Study on the relationship between microgeometry and permeability of porous media. Master’s thesis, Università degli Studi di Cagliari, Italy.
- CORTIS, A. & SMEULDERS, D. 2001 On the viscous length scale of wedge-shaped porous media. *Int. J. Engng Sci.* **39**, 951–962.
- CORTIS, A., SMEULDERS, D., GUERMOND, J.-L. & LAFARGE, D. 2001 Influence of pore roughness on high-frequency permeability. *Phys. Fluids* (submitted).
- CUSHMAN, J. 1984 On unifying the concepts of scale, instrumentation, and stochasticity in the development of multiphase transport theory. *Water Resour. Res.* **20**, No 11, 1668–1676.
- CUSHMAN, J. 1992 Hierarchical problems: Some conceptual difficulties in the development of transport equations. In *Heat and Mass Transfer in Porous Media, Proc. of the International Centre for Heat and Mass Transfer* (ed. M. Quintard & M. Todorovic), pp. 123–136. Amsterdam: Elsevier.
- CUVELIER, C., VAN STEENHOVEN, A. & SEGAL, G. 1986 *Finite element methods and Navier–Stokes equations*. Reidel, Dordrecht.
- DEVIN, C. J. 1959 Survey of thermal, radiation, and viscous damping of pulsating air bubbles in water. *J. Acoust. Soc. Am.* **31** (12), 1654–1667.
- DIEDERICKS, G. & DU PLESSIS, J. 1995 On tortuosity and areosity tensors for porous media. *Transport Porous Med.* **20**, 265–279.
- EHLERS, W. & KUBIK, J. 1994 On finite dynamic equations for fluid-saturated porous media. *Acta Mechanica* **105**, 101–117.
- ELGER, D. & ADAMS, R. 1989 An experimental study of oscillating flow through two orifices in series. *J. Acoust. Soc. Am.* **85** (3), 1065–1073.
- FIRDAOUSS, M., GUERMOND, J.-L. & LAFARGE, D. 1998 Some remarks on the acoustic parameters of sharp-edged porous media. *Int. J. Engng Sci.* **36**, 1035–1046.
- HASSANIZADEH, S. & GRAY, W. 1979 General conservation equations for multiphase systems: 1. Averaging procedure. *Adv. Water Resour.* **2**, 131–144.
- HELD, R. J. & CELIA, M. 2001 Pore-scale modeling extension of constitutive

- relationships in the range of residual saturations. *Water Resour. Res.* **37**, no.1, 165–170.
- HENRICI, P. 1991 *Applied and computational complex analysis*, , vol. 3. Wiley, Chichester.
- JANSSEN, L. & WARMOESKERKEN, M. 1987 *Transport phenomena data companion*. Edward Arnold, DUM.
- JOHNSON, D., HEMMICK, D. & KOJIMA, H. 1994 Probing porous media with first and second sound. I. dynamic permeability. *J. Appl. Phys.* **76** (1), 104–114.
- JOHNSON, D., KOPLIK, J. & DASHEN, R. 1987 Theory of dynamic permeability and tortuosity in fluid-saturated porous media. *J. Fluid Mech.* **176**, 379–402.
- JOHNSON, D., KOPLIK, J. & SCHWARTZ, L. 1986 New pore-size parameter characterizing transport in porous media. *Phys. Rev. Lett.* **57**, (20), 2564–2567.
- KELDER, O. 1998 Frequency-dependent wave propagation in water saturated porous media. PhD thesis, Delft University of Technology.
- KOSTEK, S., SCHWARTZ, L. & JOHNSON, D. 1992 Fluid permeability in porous media: Comparison of electrical estimates with hydrodynamical calculations. *Phys. Rev. B* **45**, 186–195.
- KUWABARA, S. 1959 The forces experienced by randomly distributed parallel circular cylinders or spheres in a viscous flow at small Reynolds numbers. *J. Phys. Soc. Japan* **14**, no.4, 527–532.
- LAFARGE, D. 1993 Propagation du son dans les matériaux poreux à structure rigide saturés par un fluide viscothermique: Définition de paramètres géométriques, analogie électromagnétique, temps de relaxation. PhD thesis, Université du Maine, Le Mans, France.
- LAFARGE, D., LEMARINIER, P. & ALLARD, J. 1997 Dynamic compressibility of air in porous structures at audible frequencies. *J. Acoust. Soc. Am.* **102** (4), 1995–2006.
- LAMB, H. 1932 *Hydrodynamics*, sixth edn. Cambridge Mathematical Library.
- LANDAU, L. & LIFSHITZ, E. 1959 *Fluid Mechanics*. Pergamon.
- LÉVY, T. 1979 Propagation of waves in a fluid-saturated porous elastic solid. *Int. J. Engng Sci.* **17**, 1005–1014.
- LYNCH, E. 1962 *Formation evaluation*. Harper & Row, Publishers.
- ORON, A. & BERKOWITZ, B. 1998 Flow in rock fractures: the local cubic law assumption reexamined. *Water Resour. Res.* **34**, no.11, 2811–2825.
- PARRA, J. 1997 The transversely isotropic poroelastic wave equation including the biot and the squirt mechanism: Theory and applications. *Geophysics* **62**(1), 309–318.

- PIERCE, A. 1989 *Acoustics*. J. Acoust. Soc. Am.
- PRIDE, S. 1994 Governing equations for the coupled electromagnetics and acoustics of porous media. *Phys. Rev. B* **50**, 15678–15696.
- PRIDE, S., MORGAN, F. & GANGI, A. 1993 Drag forces of porous-medium acoustics. *Phys. Rev. B* **47**, No 9, 4964–4978.
- QUINTARD, M. & WHITAKER, S. 1994 Transport in ordered and disordered porous media I: The cellular average and the use of weighting functions. *Transport Porous Med.* **14**, 163–177.
- RAYLEIGH, J. 1894 *The theory of sound*.
- REBAY, S. 1993 Efficient unstructured mesh generation by means of Delaunay triangulation and Bowyer-Watson algorithm. *J. Comp. Phys.* **106** (1), 125–38.
- RUBINSTEIN, J. & TORQUATO, S. 1989 Flow in random porous media: Mathematical formulation, variational principles and rigorous bounds. *J. Fluid Mech.* **206**, 25–46.
- RUZYLA, K. 1986 Characterization of pore space by quantitative image analysis. *SPE Formation Evaluation* **August**, 389–398.
- SAHIMI, M. 1995 *Flow and transport in porous media and fractured rock: from classical methods to modern approaches*. VCH Verlagsgesellschaft.
- SANCHEZ-PALENCIA, E. 1980 *Non-homogenous media and vibration theory*. Springer-Verlag.
- SCHWARTZ, L. 1966 *Théorie des distributions*. Paris Hermann.
- SHENG, P. & ZHOU, M. 1988 Dynamic permeability in porous media. *Phys. Rev. Lett.* **61**, No 14, 1591–1594.
- SLATTERY, J. 1967 Flow of viscoelastic fluids through porous media. *AIChE J.* **13** (6), 1066–1071.
- SMEULDERS, D., EGGELS, R. & VAN DONGEN, M. 1992 Dynamic permeability: reformulation of theory and new experimental data. *J. Fluid Mech.* **245**, 211–227.
- SMEULDERS, D., VAN HASSEL, R., VAN DONGEN, M. & JANSEN, J. 1994 Similarity of sharp-edged porous media. *Int. J. Engng Sci.* **32**, No.6, 979–990.
- TARTAR, L. 1980 *Incompressible fluid flow in a porous medium - convergence of the homogenization process*, pp. 368–377. In Sanchez-Palencia (1980).
- THURSTON, G. 1952 Periodic fluid flow through circular tubes. *J. Acoust. Soc. Am.* **24** (6), 653–656.

- THURSTON, G. & MARTIN, C. 1953 Periodic fluid flow through circular orifices. *J. Acoust. Soc. Am.* **25** (1), 26–31.
- THURSTON, G. & WOOD, J. 1953 End corrections for a concentric circular orifice in a circular tube. *J. Acoust. Soc. Am.* **25** (5), 861–863.
- TIJDEMAN, H. 1975 On the propagation of sound waves in cylindrical tubes. *J. Sound Vib.* **39** (1), 1–33.
- TREFETHEN, L. 1979 *Numerical computation of the Schwartz–Christoffel transformation*. Computer science department, Stanford University, Stanford, CA 94305.
- WHITAKER, S. 1986 Flow in porous media I: A theoretical derivation of Darcy’s law. *Transport Porous Med.* **1**, 3–25.
- WHITAKER, S. 1999 *The method of volume averaging*. Kluwer.
- WISSE, K. 1999 On frequency dependence of acoustic waves in porous cylinders. PhD thesis, Delft University of Technology.
- ZHOU, M. & SHENG, P. 1989 First-principles calculations of dynamic permeability in porous media. *Phys. Rev. B* **39**, No 16, 12027–12039.
- ZWIKKER, C. & KOSTEN, C. 1949 *Sound absorbing materials*. Elsevier Publishing Company.

SAMENVATTING

Dutch abstract

ACKNOWLEDGEMENTS

I would like to express my gratitude to all the persons who helped me during these years.

This PhD thesis would not have been succesfully completed without the constant presence, guidance, and encouragement of both my promoters, Prof. Jacob T. Fokkema, and Dr. David M.J. Smeulders. They contributed substantially to my scientific progress and, in different ways, to my maturation as an individual. *David, Jacob: Dank U wel voor alles!*

I cannot thank enough my M.Sc. supervisor, Prof. Giovanni Barrocu, who encouraged me to pursue doctoral studies. *Grazie Professore per avermi aiutato a togliere la testa dal sacco!*

I am very much indebted to Prof. Shaul Sorek, for bringing the PhD vacancy at Delft University of Technology to my attention, and many interesting scientific discussions. *Toda raba, Shaul!*

During these years, I enjoyed a wonderful collaboration with Dr. Jean Luc Guermond and Dr. Denis Lafarge, who warmly hosted me in their laboratories in Paris and Le Mans. Their expertise in solving numerical problems, and theoretical puzzles represents an invaluable contribution to my PhD thesis work. *Jean Luc, Denis: merci bien à vous pour tout!*

My gratitude extends to all the Dietz Laboratory staff for their support

and assistance at many times during the experiments. In particular, I would like to mention ir. Karel Heller: without his assistance and expertise I would not have been able to even start with the experimental work. *Karel, "I did it my way"!*

Over the years, I had both the honor and the pleasure to enjoy many interesting scientific discussions with eminent scientists in the field. Among the many I like to remember Prof. Hans Bruining, Prof. Majid Hasanizadeh, Prof. Mouaouia Firdaouss, Prof. Hans van Duijn, Prof. Amir Gubaidullin Prof. Jean Prieur du Plessis, Prof. Jacob Bear, Prof. Davide Ambrosi, and Dr. Claudio Gallo.

I express my deepest gratitude to the president and the members of the jury, for their comments and for agreeing to judge my work.

I have made many friends along the way – inside and outside the walls of the University – who helped me, one way or another, in my struggle to complete a Ph.D: Robert, Lèon, Jeroen, Boudewijn, Claudio, all the Italian friends I met at Church on Sunday, and at the “Circolo Sardo S’Argiola” in Den Haag, and many other whose names form a long list.

Last but not least, I dedicate this work to my parents, Giuseppe and Bonaria: they suffered and rejoiced along with me during these difficult years, unconditionally supporting and encouraging me with their love. For this, and for all they have done for me, there are no better words than: *Mamma, Papà, vi voglio bene!*

CURRICULUM VITÆ

July 25, 1969	Born in Iglesias, Italy
1988	Secondary school (Maturità tecnica per Geometri) at the ITCG Enrico Fermi, Iglesias, Italy.
1994	D.E.A. (Diplome des Etudes Approfondies) in Fluid Mechanics and Transport Phenomena, from ENSAM Bordeaux (France)
1997	M.Sc. Diploma (Laurea) in Hydraulic Engineering, from Università degli Studi di Cagliari (Italy)
1997 - 2002	Ph.D. student at Delft University of Technology, (The Netherlands)
2002	Visiting scientist at Weizmann Institute for Science, Rehovot (Israel)